# EXPLORING THE MILKY WAY OUTER HALO GLOBULAR CLUSTERS AM 1 AND PYXIS*

Brian L. Pohl

A dissertation submitted to the faculty of the University of North Carolina at Chapel Hill in partial fulfillment of the requirements for the degree of Doctor of Philosophy in the Department of Physics and Astronomy.

Chapel Hill
2015

Approved by:

Bruce W. Carney

J. Christopher Clemens

Daniel Reichart

Fabian Heitsch

Art Champagne

## ABSTRACT

BRIAN L. POHL: Exploring the Milky Way Outer Halo Globular Clusters AM 1 and Pyxis*.
(Under the direction of Bruce W. Carney.)

In order to probe the origins and history of the Milky Way halo, I executed a photometric survey of the outer halo globular clusters AM 1 and Pyxis using the southern astrophysical research (SOAR) telescope. The principal goal of this investigation was to determine the ages of these clusters, but the techniques employed in this process revealed other intrinsic properties such as chemical composition. A total of 32.2 hours of data were obtained on the program clusters, and observations of 22 stars from the Landolt (1992) catalogue were used to transform the clusters to the Johnson-Cousins $BV$ standard system. The resultant color-magnitude diagrams are used in conjunction with the reference globular cluster M5 to determine the intrinsic properties of the program clusters. Three independent age-determination techniques show agreement, consistent to within the error of the techniques, that AM 1 is $-1.0$ Gyr younger than, and that Pyxis is coeval to, the reference cluster M5. The chemical properties of both clusters are found to be the same for both clusters, [Fe/H] $= -1.40$ and [$\alpha$/Fe] $= +0.4$, similar to M5. The results are presented in terms of two outstanding issues regarding the outer halo; the second parameter problem and the issue of accretion vs. *in-situ* formation.


*Based on observations obtained at the Southern Astrophysical Research (SOAR) telescope, which is a joint project of the Ministério da Ciência, Tecnologia, e Inovação (MCTI) da República Federativa do Brasil, the U.S. National Optical Astronomy Observatory (NOAO), the University of North Carolina at Chapel Hill (UNC), and Michigan State University (MSU).

To my loving wife Jalene who gave me the courage and support to pursue my dream, and to a girl named Maggie who started out as my daughter but ended up my best friend.

## ACKNOWLEDGMENTS

I am extremely grateful for the guidance, mentorship, and, above all, patience of my advisor, Bruce Carney, and to the members of my committee, particularly Professors Reichart and Clemens for technical advice regarding observing practices and data reduction.

I would also like to thank the individuals listed in this paragraph for assistance with data acquisition. The lead observers Drs. Brad Barlow, Bruce Carney, Leslie Prochaska Chamberlain, Haw Cheng, Bart Dunlap, Jesse Miner, and Jim Rose, and the SOAR onsite observers Daniel Maturana, Alberto Pastén, Sergio Pizarro, Roberto Tighe, and Patricio Ugarte. I am further grateful to Dr. Sean Points for technical assistance with SOAR data.

I am extremely grateful to Paula Borden and the science enrichment preparation program (SEP), who provided financial support in the form of summer employment for the duration of my doctoral program and for welcoming me into the SEP family.

I am thankful for advice, council, and friendship, through graduate school and beyond, of Miles Blanton, Shane Brogan, Leslie Prochaska Chamberlain, Haw Cheng, Roseanne Cheng, Matt Fleenor, Richard Longland, Jay Ihry, Sean Gidcumb, Michael Good, C. Bayard Stringer, and Matt Wolboldt.

This project would not have succeeded without the love, support and encouragement of my family. And finally, thank you for reading this.

## TABLE OF CONTENTS

## LIST OF FIGURES

## LIST OF TABLES

# Chapter 1

# Introduction

On a clear, dark night, earthbound observers can see a narrow, dusty band spanning the sky. This milky band we see from Earth represents the disk portion of our galaxy; indeed the common perception of the Milky Way (MW) is only the spiral disk portion of the Galaxy, but this notion betrays several other structures unknown to astronomers even a century ago. The central region contains a bulge and a bar, and the disk itself is comprised of a thick and thin component, the latter of which forms the classic "pinwheel" appearance associated with spiral galaxies. Our sun lies within the thin disk about 8 kpc from the center of the Galaxy, which is about three-quarters of the way to the edge of the canonical boundary of the central portion of the MW ($R_{\rm GC} \leq 0.05 \times R_{\rm viral} \sim 12$ kpc, Rix & Bovy 2013). Indeed the popular conception of the MW structure would end there, but in fact the galaxy extends another order of magnitude in galactocentric radius beyond our solar neighborhood into a region called the halo.

The halo was first described by Harlow Shapely in a series of five classic papers published in 1918 and 1919. He assumed the globular clusters contained therein were in arranged in a spherical pattern around the center of the galaxy, and based on their apparent position measured the Sun at 15 kpc from the center of the MW. Globular clusters (GC) are not the only systems contained within the halo; dwarf spheroidal (dSph) galaxies, the Magellanic Clouds, open clusters, individual stars and stellar "tidal streams", or the disrupted debris of evaporating GC and dSph systems, are found therein.

But what is the origin of the halo and what does its existence and structure tell us about the origin of the MW itself? Is the halo, as classically believed (Eggen et al. 1962), comprised

of the remnants of the protogalactic structure whose angular momentum and inclination were sufficient to remain in circular orbit about the galactic center, or is it a repository for remnants of accreted systems as more recent models of galactic evolution predict? Perhaps a combination of both?

These questions remain unresolved in part due to the vast distances to, and hence faintness of, the objects in the Halo. Many of the problems discussed below will be resolved as more powerful telescopes and instruments come online. However, for the time being, the halo represents a frontier of discovery about our galaxy.

Halos are observed around other galaxies as well, but the extraordinary distances to extragalactic systems inhibits the study of individual stars. Walter Baade was able to image halo stars using photo plates during World War II, and HST has been able to resolve individual stars as far away as M87. However, to thoroughly study a stellar system, to determine its age, for example, using the techniques discussed in this work, the resolution of individual stars at the main sequence turnoff (MSTO) and fainter are required. This is only practicable for the nearest extragalactic systems such as the Magellanic clouds and local dwarf spheroidal (dSph) galaxies. And while some of these dSph galaxies exist therein, the proximity of MW halo is the best forest for which we may study the trees.

### 1.1 History of the Outer Halo

The story of the outer halo (OH) begins with Eggen, Lynden-Bell, & Sandage (1962, ELS) who argued for the formation of the MW by dissipation collapse of a protogalactic structure. They describe a scenario in which an enormous cloud of material collapses under its common gravity. During the free fall portion of this collapse, the outermost stars and clusters form and thus have highly eccentric orbits. As the cloud contracts, its angular velocity increases and the shape flattens until a disk structure forms supported by its own rotation. The evidence they produced in support of this model hinges on the association

with increased ultraviolet excess with metallicity, which was assumed to be related to age, leading to correlations with age and both orbital eccentricity and maximum height above the galactic plane. Their conclusion that the youngest stars are confined to the plane of the galaxy whereas the oldest stars are found almost everywhere support the dissipational collapse model.

As the protogalaxy collapsed, the innermost stars, residing in a denser environment, underwent rapid star formation and hence earlier enrichment of the interstellar medium. Therefore a vertical as well as radial metallicity gradient serves as a testable observable for the ELS model. Searle & Zinn (1978, SZ) undertook a survey of the abundances of 19 GCs, most of which lie in the OH, and found no radial gradient beyond $R_{\rm GC} > 8$ kpc (see Figure 1.2, which is an updated version of SZ Figure 6). Furthermore their classification of clusters by morphological type, or how generally blue or red the horizontal branch (HB) stars are, show a correlation with metallicity at inner galactic radii that breaks down for $R_{\rm GC} > 15$ kpc (see their Figure 7). This shows that metallicity, the so called "first parameter", dominates HB morphology for IH clusters, but in the OH, some other mechanism is acting. The latter effect is known as the "second parameter problem" and remains a topic of debate discussed in § 1.1.1. The combination of these effects conflict with the ELS model, and SZ proposed a scenario for the formation of the OH by accretion of sub galactic "fragments."

This debate persists over the past forty years fueled, as are many such great debates, by the probability that both combatants contain portions of the truth. Follow-up studies by Zinn (1980, 1993) and Lee, Demarque, & Zinn (1994, LDZ) provide evidence for the outer halo forming by both processes.

The inner, older population of GCs formed from the dissipation collapse of the proto-galaxy, and the outer, younger formed from some independent mechanism such as accretion of extragalactic structures, the likeliest candidates being dSph galaxies and their associated GC systems due to their continued proximity to the MW (see Marín-Franch et al. 2009, for

a recent review.)

Accretion as a component of galactic evolution comprises an important part of the ΛCDM model of the universe (see Freeman & Bland-Hawthorn 2002, for a recent review.) Observational evidence of accreted satellite systems and their tidal debris streams continues to accumulate. The most famous of these being the Sagittarius Dwarf Spheroidal (Sgr dSph) and its associated tidal streams (see Belokurov et al. 2006 and references therein). Thus little doubt remains that accretion occurred during the formation of the MW and remains ongoing. How much of the halo is of extragalactic origin (Forbes & Bridges 2010), as well as what exactly is being accreted (Geisler et al. 2007), remain open problems.

### 1.1.1 The Second Parameter Problem

As the name implies, horizontal branch stars share the same luminosity due to their common core mass of $\approx 0.5 M_{\odot}$ required to ignite helium burning. Generally speaking, the color of a HB star depends on its envelope mass; the thicker the envelope, the larger its radius. The energy of the core, related to its mass, must ultimately escape. Stellar luminosity ($L$) obeys the Stefan-Boltzmann relation for black bodies given by

$$L \propto R^2 \, T^4. \tag{1.1}$$

For fixed luminosity, as the radius ($R$) increases, temperature ($T$) must decrease. Thus more massive HB stellar envelopes have cooler surfaces and produce redder HB stars.

Due to the rapid evolutionary timescales of post main sequence stars, stars on the HB began their ascent up the red giant branch (RGB) with roughly the same mass as stars currently at the MSTO. Pre-HB stellar core masses increase as helium piles up in the hydrogen burning core, but stellar envelopes undergo mass loss of about 0.1 $M_{\odot}$, for example due to solar winds, most prominently at the tip red giant evolutionary phase. RGB mass loss is complex and ongoing topic of study (see §5 of Catelan 2009). For simplicity, the discussions

below regarding the parameters that influence HB morphology focus on the mass of MSTO stars. The relevant physics behind these effects is discussed in §4.3.

Metallicity, the "first parameter", dominates horizontal branch morphology due to its influence on stars at the MSTO. Increased metallicity raises the mass of stars at the turnoff. Thus more metal rich clusters classically show redder horizontal branches and vice-versa. However, Sandage & Wildey (1967) and van den Bergh (1967) first noticed metal-poor GCs with extremely red HBs. Some other mechanism, a "second parameter", must be at work to explain the anomalous HB morphologies.

The authors of the first studies of this phenomena put forth helium as the mechanism for the second parameter. Increased helium also increases the luminosity of a main sequence star by raising the mean molecular weight of the core. Greater luminosity means faster fuel consumption and shorter stellar lifetimes, which lowers the mass of MSTO stars resulting in a bluer HB. Age is another candidate due to its overwhelming influence on the mass of MSTO stars. The main sequence is also a mass sequence as luminosity is directly proportional to mass (a commonly cited but controversial relationship between the two is $L \propto M^{3.5}$). As the cluster ages, the turnoff luminosity, and mass, decreases. Other proposed mechanisms include CNO abundance, stellar rotation rates and cluster central density (Ashman & Zeph 1998, §2.1.3). The ultimate color of a HB star depends on the extent of mass loss near the tip of the RGB, a process that is poorly understood and difficult to measure. Thus all of the above factors are speculative and based on observational correlation.

As studies of this mystery grew, various morphological indices developed as a statistical measure of the relative number of stars blueward and redward of the instability strip (also known as the RR Lyrae gap). An example of this quantitative measure of the HB morphology is given as

$$\text{HB Type} = \frac{(B - R)}{(B + V + R)} \tag{1.2}$$

where $B$, $R$ and $V$ represent the number of stars blueward, redward and within of the RR Lyrae gap respectively (Ashman & Zeph 1998, §2.1.3). Some authors, including SZ, use the quantity $B/(B+V)$.

Plots of metallicity vs. the morphological index, first constructed by SZ though commonly called "Lee diagrams" due to their prominence in LDZ, show a correlation matching the first parameter as the principle architect of HB type for GCs within the solar circle ($R_{\rm GC} < 8$ kpc) that break down at greater galactic radii.

An insight provided by Zinn (1993, see Figure 1) is that all the clusters in the inner halo, which he defined as $R_{\rm GC} < 6$ kpc, matched a nearly linear pattern in the Lee Diagram, but the clusters beyond this galactocentric radius broke into two groups; one of which matched the inner halo trend and another forming a parallel trend shifted by about 0.4 redward in HB type. Assuming age as the second parameter, Zinn (1993) argued this latter group represented a younger, and possibly accreted population.

An example of a Lee Diagram is shown in Figure 1.1 below. This is a reproduction of Figure 5 of Mackey & Gilmore (2004), which is itself an updated version of Figure 7 of LDZ. My figure uses HB type and metallicity data from the 2003 and 2010 revisions of the Harris (1996) catalog[1] respectively. The figure does not include every entry in the catalog, merely the set of clusters for which both HB type and metallicity data are available.

The original trend used by Zinn (1993) to fit the inner halo was drawn by hand, but isochrones based on HB model evolution codes evolved over the years culminating with those developed by Rey, Yoon, Lee, Chaboyer, & Sarajedini (2001). These isochrones[2] are shown as solid lines in Figure 1.1, the darkest of which matches the mean age of the inner halo (now canonically defined as $R_{\rm GC} \leq 8$ kpc) and the lower grey lines represent relative

[1]HB type data are unlisted in the 2010 revision, presumably because the reliability of measurements from 2003 obviate revision.

[2]Private communication with Soo-Chang Rey revealed that the authors misplaced the original data used to construct the solid curves in Figure 9 of Rey et al. (2001). Under his advice, I traced the curves by eye to construct Figure 1.1

age increments of $-1.1$ and $-2.2$ Gyr respectively.

A modification of the criteria originally specified by Zinn (1993) distinguishes the populations in Figure 1.1. The exact algorithm, adapted from Keller et al. (2012), is given as

```
for each cluster
  if ([Fe/H] > -0.8)
    Classify as Disk/Bulge popluation
  else if (HB type - HB Fiducial  <  -0.3)
    Classify as Young Halo population
  else
    Classify as Old Halo
```

where `HB Fiducial` is the isochrone matching the mean inner halo age (the black line in Figure 1.1).

SZ's observation of the second parameter association with position in the galaxy led them to conclude that age primarily drives HB morphology in the OH, as HB of older clusters evolved from stars with less overall mass. The age-as-second-parameter argument couples nicely with the accretion model of galaxy evolution because the observed age difference between the OH and IH of $\approx 2$ Gyr is an order of magnitude greater than the timescale for a free-fall collapse predicted by ELS. However, the observed age difference is too short a time interval compared with dynamical simulations (see the introduction of Dotter et al. 2010a, for a recent and comprehensive review).

Furthermore, MSTO measured ages appear to differ among clusters of similar metallicity. Clusters that share similar metallicities but widely different HB types are referred to as "second parameter pairs", the classic example of which being NGC 288 and NGC 362. Both clusters share a similar metallicity of $-1.32$ and $-1.30$ respectively (Carretta et al. 2009), but NGC 288 has an exclusively blue HB and NGC 362 is mostly red. Catelan, Bellazzini, Landsman, Ferraro, Pecci, & Galleti (2001) showed an age difference of $2 \pm 1$ Gyr that could explain the variation in HB morphology. However, most recently, VandenBerg, Brogaard,

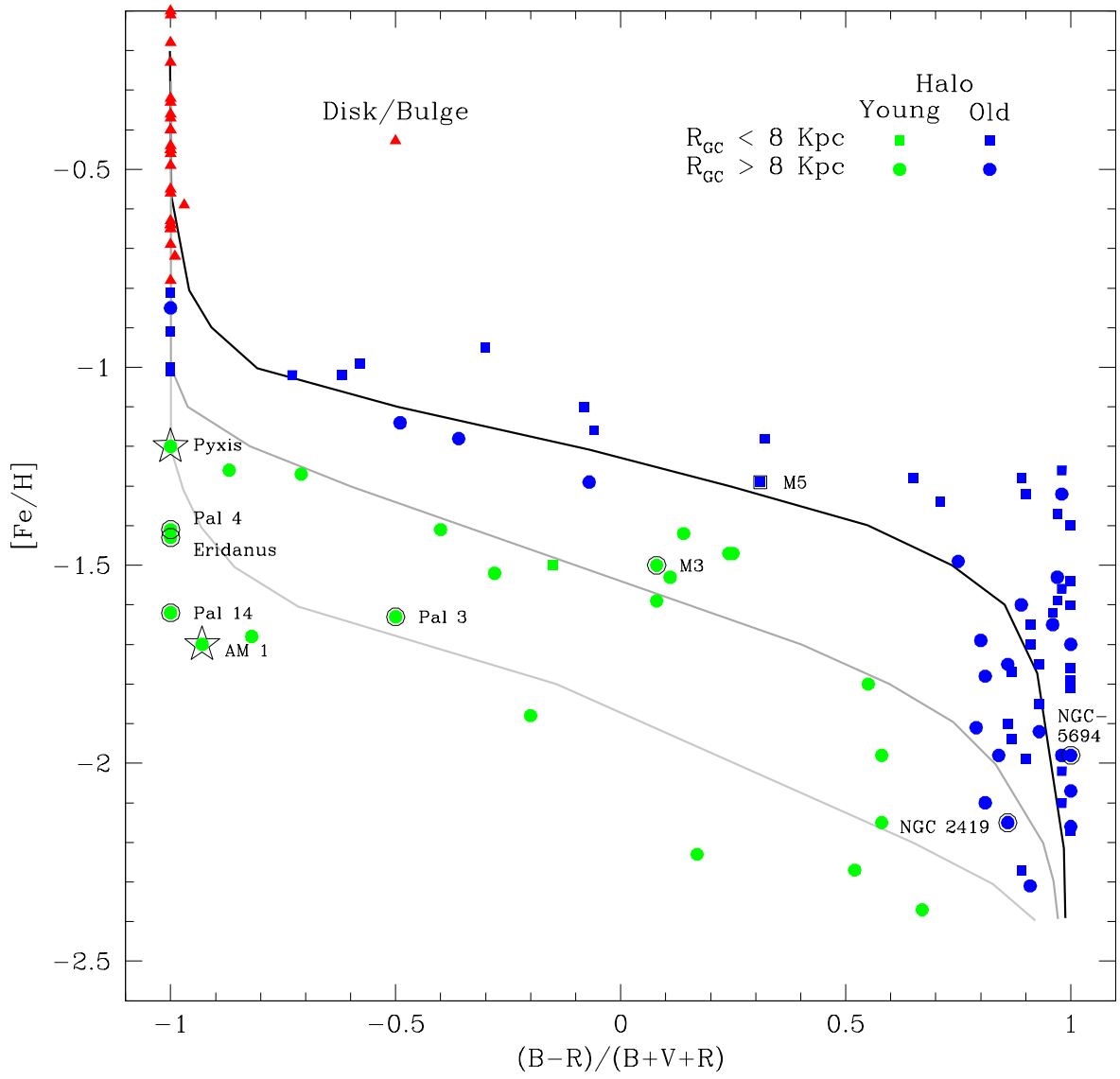


Figure 1.1 Example of a Lee Diagram constructed using the 2003 and 2010 revisions of Harris (1996). The solid black line represents the isochrone for the mean age of the inner halo population based on the models of Rey et al. (2001). The grey lines below represent relative age increments of −1.1 and −2.2 Gyr respectively. Metallicity alone distinguishes the disk/bulge population, whereas HB type offset between the mean inner halo age isochrone at a cluster's metallicity distinguishes the young and old halo populations (see text for details).

Leaman, & Casagrande (2013), employing the most recent and accurate technique for relative age determination discussed in further in §4.2.2, find an age difference between the clusters of only $0.75 \pm 0.45$ Gyr. They argue that, in addition to age, enrichment variations in helium or Mg and Si may be at work. Additionally, analyses of the MSTO derived ages for several such second parameter pairs show enough variation that HB morphology cannot be explained by age alone (see §7 of Catelan 2009).

Thus some other factor or set of factors in addition to or perhaps exclusive of age may be required. Most recently, Dotter (2013) points out one of the reasons the problem remains so intractable is that the approach one takes biases the conclusion. Indeed the study of the second parameter problem remains an open debate. That the second parameter effect appears characteristic of the OH is of greater concern to this work than the exact mechanisms behind it.

## 1.2 The Globular Clusters

Globular clusters are classically believed to be simple systems of stars that formed from the same material at the same time. As such, they are coeval and homogenous in composition, which makes them among the few systems for which reliable ages may be determined. Furthermore, globular clusters are compact enough to survive the accretion process despite complete evaporation by their parent system. This makes them analogous to fossil relics of our galaxy's past.

Why study AM 1 and Pyxis? As discussed in §1.2.2 and §1.2.3, at the onset of data acquisition for this project in the fall of 2008, little was known about either cluster. AM 1, being the most distant and hence faintest GC, serves as an excellent capability indicator for the, as then newly commissioned, Southern Astrophysical Research Telescope (SOAR). As shown in Table 2.1, both clusters are of sufficient southern declination for SOAR to practically survey.

In the course of investigating the background of these clusters, some interesting scientific motivations arise. Both clusters show the second parameter effect and have apparently young ages, but their position in the Galaxy is curious in itself. Figure 1.2, an updated version of the same plot by SZ showing galactocentric distance vs. metallicity, shows a curious region between $40 \lessapprox R_{\rm GC} \lessapprox 60$ kpc, labeled as "the gap," that contains no currently known clusters. The logarithmic scale of the horizontal axis betrays the relative size of "the gap;" it is 2.5 times wider than the radius of the solar circle. Figure 1.2 uses the same data and symbol convention as Figure 1.1. As the most distant cluster identified with the MW, AM 1 contains the outer region beyond the gap along with only five other clusters (see Table 1.1.) This outer region also occupies the nearest dSph galaxies making the clusters therein likely accretion remnants. At 42 kpc, Pyxis lies at the innermost edge of the gap and cannot be so easily identified as an accretion candidate by position alone. Thus similarities between the current properties of Pyxis and AM 1 point to a common mechanism of origin.

Before embarking on our own exploration of these clusters, let us begin with the state of knowledge to date regarding all outermost halo clusters. The remainder of this section summarizes work performed by other authors with an emphasis on measurements relevant to age and chemical composition.

### 1.2.1 The Extreme Outer Halo

The outermost part of the halo, beyond the "the gap," is frequently referred to as the "extreme outer halo" (EOH). To provide some context for the study of AM 1 and Pyxis, this section probes the most recent studies of the clusters in this region. We keep an eye trained on the issues of what constitutes the typical characteristics of an EOH cluster and which clusters are unique. The key issues to note include whether or not the cluster shows the second parameter phenomenon, unusual elemental abundances ($[X/\mathrm{Fe}]$, where $X$ is any element greater than He), and whether or not the cluster seems "typical" with regards to the

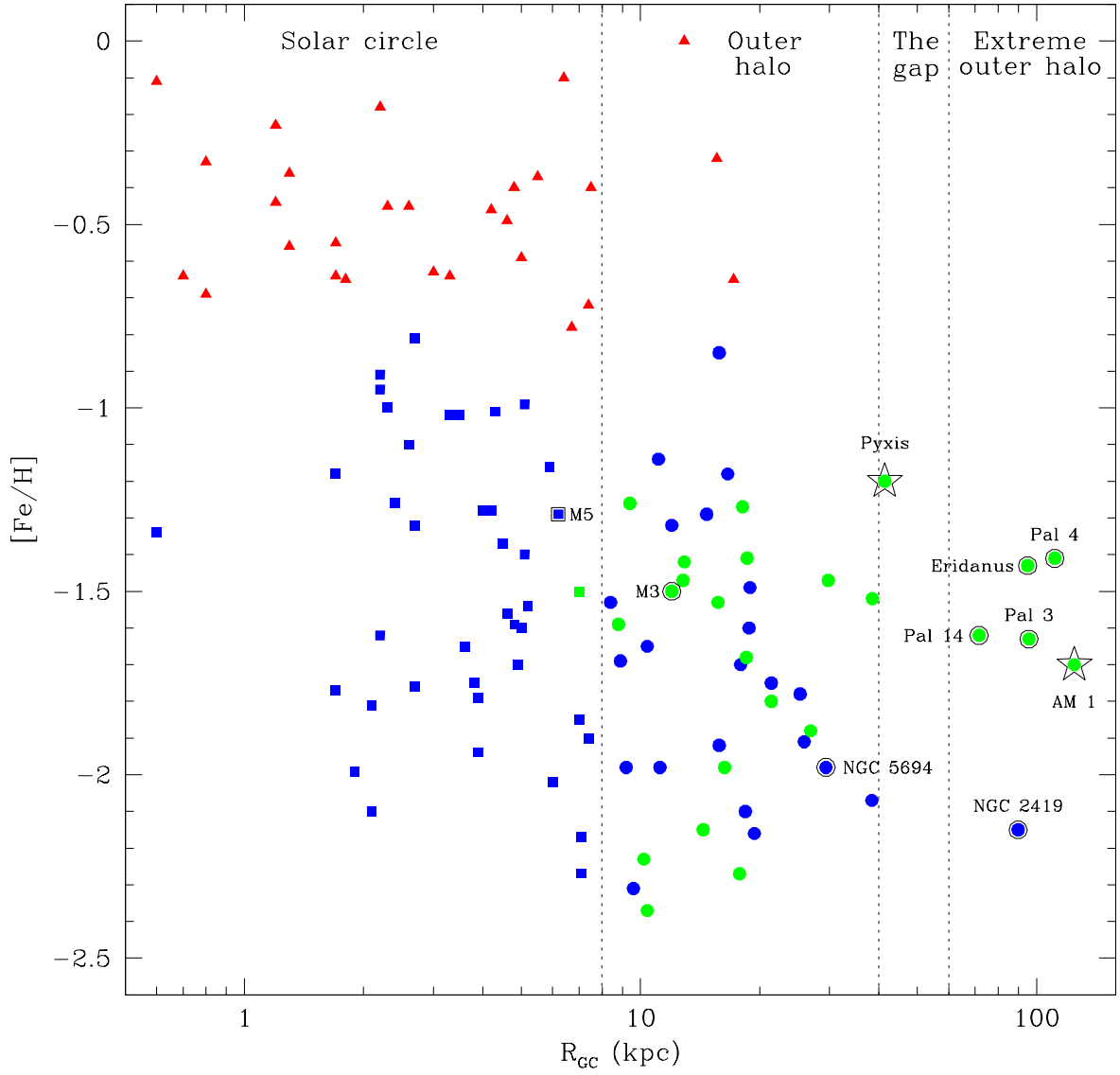


Figure 1.2 Metallicity versus galactocentric radius using data from Harris (1996, 2010 revision). The symbols match those defined in Figure 1.1. Note the presence of a metallicity gradient with 10 kpc that breaks at greater radii as well as the gap between $\sim 40$ and $\sim 60$ kpc devoid of clusters.

other clusters in the outer halo.

From a chemical perspective, a look at Figure 1.2 shows that the most metal rich clusters

lie within the solar circle and, though there is quite a bit of spread, the OH appears to be restricted to the range $-2.0 \lessapprox$ [Fe/H] $\lessapprox -1.0$. Carney (1996) notes that the OH clusters share a common $[\alpha/\mathrm{Fe}] = +0.3$. §4.3.1 discusses the specific effects of age, metallicity, helium, and $\alpha$ enhancements of the cluster in the observational plane as well as the relevant physics. In the discussion that follows, we begin with the EOH clusters that appear "typical" in a chemical sense and conclude with the outliers.

It is also worth noting the chemical inventory of nearby dSph galaxies as a number of clusters in the EOH are considered accretion relics. Venn et al. (2004) notes that dSph galaxies share very low $\alpha$ (very nearly solar) enhancements and are simultaneously more metal rich than the MW. She uses these results to argue against the idea of an accreted EOH population.

**Palomar 3**

We begin our survey of the EOH with what appears to be the most generic sample. Palomar 3 resides at a distance of $R_{\mathrm{GC}} \simeq 92$ kpc and is about 1.5 to 2.0 Gyr younger than M3 according to Stetson et al. (1999). Koch et al. (2009) reports $[\mathrm{Fe/H}] = -1.58 \pm 0.13$ and $[\alpha/\mathrm{Fe}] = 0.35 \pm 0.23$. They report all chemical abundances fully consistent with the clusters and field stars of the outer halo. Indeed, the title of their paper, "All Quiet in the Outer Halo", implies that this cluster as a benchmark standard of ordinariness for this neighborhood.

**Palomar 4**

A galactocentric distance of 109 kpc (Stetson et al. 1999) and a half light radius a full order of magnitude greater than that of a typical GC distinguishes Palomar 4 as among the most distant and diffuse globular clusters known. Stetson et al. (1999) determined its age about 1.5 to 2.0 gyr younger than M5, consistent with the ages of the other EOH clusters.

Coupled with its relatively low total luminosity, these properties make it similar in many ways to UFD. Koch & Côté (2010) obtained high resolution spectra of 19 RGB stars using the Keck/HIRES spectrograph. They report [Fe/H] = $-1.41\pm0.17$ and [$\alpha$/FE] = $0.38\pm0.11$, the latter being consistent with the rest of the EOH clusters with the exception of NGC 2419. Its extremely red HB places it comfortably in the territory of the Lee Diagram occupied by its neighbors. Though they report an unusual [Mg/Ca] abundance, Koch & Côté (2010) find its overall chemical pattern in agreement with the other EOH clusters; they even go as far as to describe Palomar 3 and Palomar 4 as "twins" due to their nearly identical chemistry, distance and half light radii.

**Palomar 14**

At a heliocentric distance of $\sim 71\pm2$ kpc (Sollima et al. 2011), Palomar 14 is the innermost EOH cluster. Like the other clusters its neighborhood, it is faint, diffuse, displays a red HB and is about 2 Gyr younger than M3 (Dotter et al. 2008b). High resolution spectroscopy by Caliskan et al. (2012) reports [Fe/H] = $-1.44\pm0.03$ and [$\alpha$/Fe] = $0.34\pm0.17$. These results as well as the other elemental ratios show Palomar 14 as nearly identical in chemical abundances as the EOH clusters Palomar 3 and Palomar 4. One of the most striking discoveries regarding this cluster is the presence of two tidal tails (Sollima et al. 2011). The chemical similarity of this cluster to the other Palomar clusters in the EOH, as well as the presence of its tidal tails, lead the authors of both studies to conclude Palomar 14 is a likely an accretion relic from an evaporated dSph parent galaxy.

**Eridanus**

The most comprehensive, though aging, review of Eridanus is given by Stetson et al. (1999). Its metallicity ($-1.42 \pm 0.08$ dex, Carretta et al. 2009, and references therein), distance and age (Catelan 1999) are quite similar to Palomar 4, enough so that investigations in

to the second parameter problem they are cited as classical second parameter pairs (Catelan 2009). Much like its second parameter cousin, everything about this cluster seems typical of the EOH. However, no high resolution spectroscopic studies yet exist for this cluster. The metallicity cited above ultimately comes from Calcium II triplet line strength analysis by Armandroff & Da Costa (1991).

Here ends the discussion of the "typical" EOH clusters. What follows represent the clusters that are dissimilar to the others.

**NGC 5694**

Though its current galactocentric distance of 30 kpc, similar to that of Pyxis, excludes it from the canonical EOH group, its velocity with respect to the galactic center of $-273 \pm 13$ km/s lead Harris & Hesser (1976) to believe it an interloper from the EOH whose orbit extends to $\sim$ 100 kpc. Lee, Lopez-Morales, & Carney (2006), making use of the chemical tagging technique with high resolution spectra of a single red giant in the cluster, noticed anomalously low values of [$\alpha$/Fe] and [Cu/Fe] compared to globular clusters of similar metallicity and concluded the cluster is likely of extragalactic origin. Mucciarelli et al. (2013) extended the study to include a total of six red giants in the cluster and measured [Fe/H] $= -1.98 \pm 0.03$ and [$\alpha$/Fe] $= 0.02 \pm 0.02$. Its low metallicity and blue dominated HB place it in the lower right of the Lee Diagram, quite apart from the EOH clusters that occupy the lower left. Additionally its solar $\alpha$ enhancement distinguishes it chemically from the rest of the outer halo. Mucciarelli et al. (2013) ultimately agrees with the conclusions of Lee et al. (2006) that NGC 5694 is an interloper from the EOH and of extragalactic origin, but it formed in an environment unique to the rest of the EOH which are believed to be relics of dSphs. Ultra Faint Dwarf (UFD) galaxies share a similar combination of poor metallicity and solar $\alpha$ enhancement, leading the authors to believe this as the likeliest parent environment. They also note that Ruprect 106 shares similar enough chemical pattern as to be a

potential chemical sibling.

**NGC 2419**

We conclude this tour of the EOH with the most interesting cluster of them all. Second in luminosity among globular clusters beyond $R_{\rm GC} > 15$ kpc to M54, which is known to be the core of the Sgr dSph, NGC 2419 is more massive, by an order of magnitude, than all the EOH globular clusters *combined* (Borissova et al. 1996, see Table 7). With a blue dominated HB, it occupies the opposite side of the Lee Diagram than the rest of the EOH clusters with the exception of the interloper NGC 5694 which is suspected of being a UFD. Chemical analysis by Cohen et al. (2011) show a mean [Fe/H]$= -2.06 \pm 0.10$ and [$\alpha$/Fe] $=$ $0.19 \pm 0.4$; both low compared to the rest of the EOH. A closer look at the chemical inventory by Cohen & Kirby (2012) showed an anomalous depletion of magnesium in a third of stars in the cluster. The authors describe this anomaly as "unprecedented" among globular clusters, leading them to conclude that NGC 2419, like its luminous cousin M54, is the nucleated core of a dSph.

Very recently, Mucciarelli et al. (2015) also discovered a K–Mg anti-correlation in NGC 2808, a cluster known to have three distinct populations (Piotto et al. 2007). The three populations in NGC 2808 are believed to be subsequent generations of stars formed from the gravitationally bound debris of primordial stars. As such, Mucciarelli et al. (2015) attribute the K–Mg anti-correlation to a self-enrichment scenario. While this does not exclude the possibility of NGC 2419 being a nucleated dSph, indeed a dSph would have no trouble providing enough gravitational potential to retain the gas from early generations of stars, the K–Mg anti-correlation, in and of itself, no longer provides evidence for this classification.

Table 1.1. Extreme outer halo (EOH) globular clusters.

| Cluster ID | $R_{GC}$ (kpc)[a] | HB Type[b] | [Fe/H][c] | [$\alpha$/Fe] |
|---|---|---|---|---|
| NGC 5694 | 29.4 | +1.00 | $-1.98 \pm 0.03$ | $0.02 \pm 0.02$ |
| Pyxis | 41.4 | −1.00 | $-1.4 \pm 0.1$ | ... |
| Palomar 14 | 71.6 | −1.00 | $-1.44 \pm 0.04$ | $0.34 \pm 0.17$ |
| NGC 2419 | 89.9 | +0.86 | $-2.06 \pm 0.10$ | $0.19 \pm 0.36$ |
| Eridanus | 95.0 | −1.00 | $-1.42 \pm 0.08$ | ... |
| Palomar 3 | 95.7 | −0.50 | $-1.58 \pm 0.13$ | $0.35 \pm 0.23$ |
| Palomar 4 | 111.2 | −1.00 | $-1.41 \pm 0.17$ | $0.38 \pm 0.11$ |
| AM 1 | 124.6 | −0.93 | $-1.7 \pm 0.2$ | ... |

[a]Distances from Harris (1996, 2010 revision)

[b]Horizontal branch types of the form $(B-R)/(B+V+R)$ from Harris (1996, 2003 revision)

[c]Whenever possible, metallicities and $\alpha$ enhancements are from the latest high resolution spectroscopic studies. References contained in the text.

**Summary**

With the exceptions of NGC 2419 and NGC 5694, the extreme outer halo clusters show nearly uniform metallicity ($-1.6 \lesssim$ [Fe/H] $\lesssim -1.4$) and mean alpha element ($0.3 \lesssim$ [$\alpha$/Fe] $\lesssim$ 0.4) enhancements as shown in Table 1.1. The authors of the most recent studies of nearly all these clusters argue for their extragalactic origin.

### 1.2.2 AM 1

Though previously identified as ESO-201-SC by Holmberg & Lauberts (1975) during their survey of the ESO "Quick Blue" plates, the designation Arp-Madore-1, or simply AM-1, assigned by Madore & Arp (1979) persists because they produced a color-magnitude diagram (CMD). They discovered three faint stellar clusters among the IIIa-J plates acquired by the Australian UK Schmidt Telescope Unit. Based on the limiting magnitude of $m_J = 20.5$ on the ESO discovery plates and an assumed color of $(B-V) = 1.4$ for red giants, they estimated that the brightest stars have a magnitude of $B = 21.2$. Coupled with an absolute magnitude $M_B = -1.5$ for the red giants as well as an interstellar absorption value of $A_B \sim 0.3$ based

Table 1.2. AM 1 candidate RR Lyrae stars reprinted from Ortolani (1984).

| Star ID* | $V$ | (B-V) |
|---|---|---|
| 12 | 21.02 | 0.33 |
| 19 | 21.27 | 0.28 |
| 50 | 21.10 | 0.40 |
| 67 | 21.16 | 0.46 |
| 83 | 21.07 | 0.45 |

Note. — * The Star ID column is Ortolani's designation. His paper provides a finder chart

on the cosecant law[3] of Harris & Racine (1979), they reported a tentative distance of 300 kpc.

Ortolani (1984) obtained $BV$ photometry using the 1.5 meter ESO telescope at La Silla to a limiting magnitude of $V = 23$, sufficient to identify the horizontal branch (HB). They also identified 5 possible RR Lyrae (RRL) stars based on their de-reddened color lying within the RRL gap $[1.8 \leq (B-V) \leq 4.2]$. However, they assume an interstellar extinction term of $E(B-V) = 0.03$ based on the cosecant law. All subsequent authors assumed interstellar extinction to be negligible for this object $[E(B-V) = 0.00]$. Without the extinction correction, two of their RRL candidates fall outside the RRL gap. Table 1.2 lists non-extinction corrected colors for the candidate RRLs.

Based on an assumed $< M_V >= 0.6$ for the RR Lyraes, Orlotani reported a distance of $R_{GC} = 123 \pm 10$ kpc. Using the color index of the RGB at the HB of $(B-V)_{0,g} = 0.76 \pm 0.08$ he estimates a metallicity of [Me/H] $= -1.6 \pm 0.4$ based on the average value of three techniques.

Working independently using the CTIO 4m telescope, Aaronson, Schommer, & Olszewski (1984) obtained a total exposure of 3000 seconds each in $B$ and $V$ (though only 2000 of each

[3] $E(B-V) = K_{bv}\,[1 - \exp(-Z/Z_0)] \times \csc|b|$ where $Z_0$ is the scale height of the Galactic extinction layer and $K_{bv}$ is a derived constant equal to 0.056 and 0.040 for the north and south poles (Racine & Harris 1989, Equation 2).

were on nights designated as "clear"). They show a well-defined HB but do not identify any candidate RRL stars as the blue edge of their HB lies outside the RRL gap [$(B-V) = 0.47$]. They assume no interstellar reddening [$E(B-V) = 0.00$] based on the maps of Burstein & Heiles (1982).

Assuming $M_V(\mathrm{HB}) = 0.6$, they computed a distance of $R_{\mathrm{GC}} = 118 \pm 2$ kpc. Their upper RGB is heavily contaminated by field stars, leaving them confident of only one upper RGB star in their sample of cluster members. Based on a fit of the upper RBG heavily weighted by this one star, they estimated a metallicity of $[\mathrm{Fe/H}] = -1.8 \pm 0.3$.

Both Aaronson et al. (1984) and Ortolani (1984) measurements of distance and metallicity agree within the errors, something Orlotani points out as support for their results. Though the discrepancy in the reddening between the two authors raises an eyebrow. Due to the extremely red nature of the HB, both authors identify AM 1 as a good second parameter cluster in need of future studies, particularly with regard to spectroscopy.

The only spectroscopic study of AM 1 was undertaken by Suntzeff, Olszewski, & Stetson (1985). Using the 2.5 m du Pont telescope at Las Campanatas Observatory in November of 1983, they obtained spectra on the two brightest stars in the cluster (shown as red plus symbols in Figure 4.9). Based on the line strengths of the Calcium II H and K line strengths, they determined a metallicity of $[\mathrm{Fe/H}] = -1.7 \pm 0.2$. They further determined a Galactocentric radial velocity of $-41$ km/s.

Hilker (2006) obtained VLT data in $BV$ to $V \leq 22.9$. His CMD shows a well defined HB and RGB suitable for fitting with the Yonsei-Yale ($\mathrm{Y}^2$, Kim et al. 2002) isochrones. However, Aaronson's metallicity estimate of $-1.8$ did not adequately fit the data. Instead a metallicity of $-1.4$ was used for the best fitting isochrones. Other fitting parameters fix the age at 11 Gyr, and $[\alpha/\mathrm{Fe}] = 0.3$ dex. He further used an an artificial color shift of $-0.01$ to correct an offset between his best fitted isochrone and the data that he ascribes to reddening.

Hilker's CMD does not reach faint enough in V to see the MSTO, but his motivation was

to establish reliable cluster members and good positions for further spectroscopic work on individual stars, necessary to lay to rest many questions regarding the chemical history of the cluster and its origin. His final catalog has positions reported to 0.01" RA and 0.1" Dec.

Finally and most recently, Dotter et al. (2008b) obtained HST data in $V$ and $I$ (or in the HST parlance, F555W and F814W respectively) down to 28th magnitude in $V$. In addition to the RGB and HB, the MSTO is clearly visible as well as some blue stragglers that appear interesting as well.

Because Hilker's CMD's does not include the MSTO, they are skeptical of his metallicity estimate and use a baseline of [Fe/H] $= -1.5$ as their baseline for a differential technique of isochrone fitting using M3 as a comparison. They caution that this technique is only valid in the extent that M3 and AM 1 are of the same composition, a point they repeatedly stress as need for follow up high resolution spectroscopy. Their final values are [Fe/H] $= -1.5$, [$\alpha$/Fe] $= +0.2$, age = 11.1 Gyr or 1.5 Gyr younger than the comparison cluster M3.

Their paper shows that all six GCs with $R_{GC} > 50$ kpc are younger than the inner halo clusters, evidence, they argue, that all such clusters were accreted and the best candidate for the second-parameter is age. But they stress the need for direct metallicity measurements are necessary. Indeed four different authors using different techniques arrived at four different values.

### 1.2.3 Pyxis

While searching the Palomar Observatory Sky Survey for planetary nebulae, Weinberger (1995) discovered several new objects worthy of followup study including a possible satellite globular cluster or dwarf spheroidal galaxy. Follow-up work by Da Costa (1995) and Irwin, Demers, & Kunkel (1995) confirmed the object as an outer halo GC; the former investigator designated it as "C J0907-372 (Pyxis)" and the latter suggested the simply Pyxis.

Da Costa (1995) obtained 900 second $B$ and 300 second $R$ CCD images using the $\approx$ 3.9 meter Anglo Australian Telescope (AAT). Poor seeing ($2\farcs1$) restricted their limiting magnitude of their CMD, their Figure 3, to $R \approx 22$ mag. However, their large overall FOV compared to the SOAR optical imager (SOI) allowed them to construct a field star CMD, shown as the lower panel of Figure 3. The fact that their FOV encompassed the entire cluster allowed them to fit a King (1966) model to the surface density profile and determine the core radius of $83''$. Their inability to fully capture the MSTO restricted their conclusions about age to a lower limit on magnitude difference between the HB and MSTO of $\Delta R_{\rm HB-TO} \geq 3.25$, leaving them no reason to suspect the cluster's age is radically different compared to the rest of the halo GCs which have values of $\sim 3.5$ (Green & Norris 1990). Fitting RGB fiducial sequences of NGC 362 and NGC 6397 established a galactocentric distance of $R_{\rm GC} \approx 37$ kpc, but the disparity of metallicities between the fiducial clusters, [Fe/H] $= -1.28$ and $-1.91$ respectively, while both providing good matches to the Pyxis RGB, restrict their conclusions metallicity to the range bound by those of the reference clusters and extinction to the interval of $0.25 \leq E(B-V) \leq 0.40$.

Working independently, Irwin et al. (1995) acquired $B, R$ and $I$ CCD data using the 2.5 meter du Pont telescope at Las Campas Observatory. Their Figure 3 shows a CMD with a limiting magnitude of $R \approx 23$ mag, or about a half magnitude below the MSTO. Application of the Yale isochrones (Green, Demarque, & King 1987) resulted in a metallicity of [Fe/H] $= -1.1 \pm 0.3$ and an age of $13 \pm 3$ Gyr assuming a reddening of $E(B-V) = 0.19 \pm 0.04$ consistent (though barely) with the value of $\approx 0.23$ derived from the maps of Burstein & Heiles (1982). The metallicity agrees with the value of $-1.0 \pm 0.3$ determined by the dereddened color of the RGB at the magnitude of the HB ($(B-V)_{0,g} = 0.9 \pm 0.1$). Their absolute age measurement is subject to the uncertainties of the Yale (or indeed any) isochrone's ability to measure true ages and increases the error to $\pm 4$ Gyr. Finally, they reported a Galactocentric distance of 42 kpc based on the mean $R$ magnitude of 24 HB stars

and the $M_V(\mathrm{RR}) = 0.15[\mathrm{Fe/H}] + 0.72$ relationship of Walker (1992).

Acknowledging the previous investigators' efforts as good initial reconnaissances of Pyxis, Sarajedini & Geisler (1996) set out to construct a CMD faint enough to fully establish the MSTO and determine the age of the cluster. They obtained single 30 and 600 second exposures in R and 60 and 1200 second exposures in $B$ using the CTIO Blanco 4 meter telescope on a night with good seeing ($0\farcs9$ and $1\farcs1$ respectively). Their CMD (Figure 2) extends to $R \approx 24$ or about a magnitude below the MSTO. The $14\farcm7$ FOV allowed them to fully sample the field star CMD (Figure 3) and restrict their sample to stars within twice the core radius established by Da Costa (1995). Making use of the simultaneous reddening and metallicity method (SRM, Sarajedini 1994) adapted for the $B, R$ system, they derived $[\mathrm{Fe/H}] = -1.20 \pm 0.15$ and $E(B-V) = 0.21 \pm 0.03$, both of which are in good agreement with Irwin et al. (1995) and Da Costa (1995). Employing a technique involving the color difference between the HB and the RGB (Sarajedini et al. 1995), they reported an age of $13.3 \pm 1.3$ Gyr subject to the usual systematic errors associated with GC absolute ages. More convincing are the relative ages derived by overlaying fiducial sequences, shown in their Figure 5, that show Pyxis to be of similar age to NGC 362 and significantly younger than NGC 288. Recall that NGC 288/362 are the classic second parameter pair as they share similar metallicity but drastically different HB types (Catelan et al. 2001). Finally, using the mean $R$ magnitude of 27 HB stars and the absolute magnitude relation of Lee (1990), $M_V(\mathrm{RR}) = 0.17[\mathrm{Fe/H}] + 0.79$, they reported a Galactocentric distance of 41 kpc.

All the investigations above mentioned the need for spectroscopic measurements, to which Palma, Kunkel, & Majewski (2000) answered the call, obtaining spectra with a 1200 line/mm grating spectrograph configured for a 7700–8750 Å wavelength range and roughly 1.3 Å/pixel detector resolution at the 2.5 meter du Pont Telescope at Las Campanas. Motivated to determine the orbital kinematics in order to test the hypothesis of Pyxis as a captured LMC object put forward by Irwin et al. (1995) and later supported by Palma, Majewski,

& Johnston (2002, submitted at the time), radial velocities comprised their primary goal. Their exposure times provided sufficient SNR for radial velocities of the brightest six stars, labeled A through F in order of brightness, from which they obtain a mean radial velocity of 39.5 km/s after excluding one outlier, Pyxis D, from their sample. Only the brightest star, Pyxis A, provided sufficient SNR for metallicity estimation. Following the technique outlined by Rutledge et al. (1997), Calcium II equivalent width measurements, $W'$, yielded a metallicity of [Fe/H] $= -1.4 \pm 0.1$ dex.

Finally, Dotter et al. (2011) obtained *HST* data in the $F606W$ and $F814W$ (or $V$ and $I$) filters for Pyxis along with five other GCs in the interval $15 \leq R_{\rm GC} \leq 50$ kpc. Their CMD (Figure 3) extends to 26th magnitude in $V$ ($F606W$), or $\sim 4.5$ mag below the MSTO. Applying the age determination technique described by Dotter et al. (2010b, section 4.2) using the Dartmouth Stellar Evolution Database (Dotter et al. 2008a, DSED) isochrones, they reported an age of $11.5 \pm 0.1$ Gyr, $V$ magnitude distance modulus ($\mathrm{DM}_V$) of 18.64, $E(B-V) = 0.25$, [Fe/H] $= -1.5$, and [$\alpha$/Fe] $= 0.2$ (see their Table 3).

### 1.3 Purpose

To best understand the origins of AM 1 and Pyxis and their insights into the formation of the outer halo, we must first ascertain their physical properties as best as possible. Detailed chemical abundance and kinematics measurements could lay to rest many of these questions through "chemical tagging" (see, for example, Geisler, Wallerstein, Smith, & Casetti-Dinescu 2007; Brewer & Carney 2006), if only the instrumentation existed to obtain the requisite high resolution and SNR spectra.

Thus we employ the best tools at our disposal for the study of this frontier. The SOAR telescope provides sufficient aperture to study such faint objects, and our access to roughly one or two nights per month each target is available allows for an unprecedented amount of total exposure time on each target. One of the goals of this project is to completely

exhaust the possibilities of ground-based instrumentation for AM 1 and Pyxis, making future applications for time on space based instrumentation more compelling, if deemed necessary.

Wide bandpass photometry makes the most efficient use of telescope aperture and time by exploiting the greatest amount of light. The consequence is that chemical abundance measurements must be made in an indirect fashion. Photometrically derived parameters such as metallicity are worthwhile goals in that they serve as starting points, and verification tests, for more direct techniques. Therefore we set out on this campaign with the goal of deriving such properties with the caveat that their conclusive determination will not be available until instruments capable of high resolution spectroscopy (or perhaps some as yet unforeseen technique) are available.

The age of a globular cluster is the most worthwhile and reliable measurement photometry reveals. Being classically considered coeval systems[4], the stars therein show all stages of stellar evolution. A globular cluster color-magnitude diagram (CMD) shows a main sequence, subgiant and red-giant branches, horizontal branches and asymptotic giant branches. As discussed later, comparisons of stars at different evolutionary phases in the CMD reveals the age of the cluster as a whole. Revisiting the analogy of globular clusters as fossils, revelations about the age of a cluster provide clues about its origins and history inasmuch as carbon dating reveals the same of a biological fossil.

The purpose of this endeavor, therefore, is reliable age determination for AM 1 and Pyxis using a variety of techniques. In the process, we hope to discover or confirm other intrinsic properties of the clusters such as metallicity and $\alpha$ element enhancement as well as extrinsic properties of distance and interstellar extinction.

Chapter Two discusses the observing program and the data reduction process. Chapter Three describes the calibration of the stars to the standard system and the construction of the CMDs. In Chapter Four, I bring to bear three independent techniques for determining

[4]There are a growing number of clusters that show multiple populations betraying the notion that all GCs are coeval systems. See Piotto (2009) for a review.

the age of the clusters as well as the other properties listed above.

# Chapter 2

# Data and Analysis

## 2.1 Observations

Several individuals, including myself, obtained the data between the fall of 2007 and spring of 2009 using the Southern Astrophysical Research (SOAR) telescope, a 4.1 meter aperture telescope located on Cerro Panchón, Chile, at an altitude of 2,700 $m$ and south latitude of $-30.2°$. In order minimize the effects of the atmosphere on the star light, we maintained an observing constraint of an airmass, $X$, less than 2, or a maximum of 30° from the zenith. SOAR's south latitude restricts the preferred ($X < 2$) observing declination range to $0° \geq \delta \geq -60°$, ideal for southern hemisphere targets due to the availability of equatorial standards as well as program fields. Table 2.1 lists the celestial coordinates for the clusters and standard fields.

Table 2.1. Target Coordinates

| | Target | Number of Standards* | RA (J2000) | Dec |
|---|---|---|---|---|
| *Clusters* | AM 1 | ... | 03:54:54.0 | -49:36:38 |
| | Pyxis | ... | 09:07:57.8 | -37:13:17 |
| *Standard star fields* | PG 0231+051 | 6 | 02:33:39 | 05:18:44 |
| | SA 98 | 6 | 06:52:10 | 00:18:56 |
| | Rubin 149 | 6 | 07:24:10 | 00:31:41 |
| | PG 0918+029 | 4 | 09:21:31 | 02:47:05 |

* Each field from Landolt (1992) typically contains many more stars than listed here. The number listed in this table represents the total available given the coordinates and SOI's field of view. See Table 3.2 for colors and magnitudes of each standard star in the field.

We imaged the clusters and standard fields using the SOAR Optical Imager (SOI[1]), a mosaic of two 2048x4096 pixel Charged Coupled Devices (CCDs), with the Johnson-Cousins $B$ and $V$ filters. When operating SOI in the default 2x2 binning mode, and accounting for the physical gap between the long edges of the detectors (see §2.2.1), the resulting images are 2099x2048 pixels with a resolution of $0.154''$/pixel.

CCD binning is the process of combining the signal, electrons corresponding to the number of photon hits, collected in the physical pixels of a specified area into a "super pixel" using the readout register. The procedure trades spatial resolution for increased readout time, smaller output file size, and greater signal-to-noise (SNR) due to the single passage of the accumulated charge of the "super pixel" through the readout register as opposed to each individual pixel incurring the readout register noise. The unbinned pixel resolution of $0.077''$/pixel is extremely small compared to the best seeing of $\sim 0.5''$. Thus the 2x2 binning reduces the noise while retaining enough resolution to measure the stellar profile.

We planned our observations around constructing light curves for variable stars should we discover any. Therefore, we always began and ended an observing session with a $V$ frame and alternated $B$ and $V$ frames in between. A complete list of the observations are listed in Tables A.1 and A.2 in Appendix A. Table 2.2 summarizes the observations.

We operated SOI remotely in Chapel Hill using the Constance and Leonard Goodman Remote Observing Room (Cecil & Crain 2004, though the facility is now located in Chapman Hall). On-site telescope operators controlled SOAR under the direction of the observers via videoconferencing.

In addition to the target clusters, we observed standard stars (or simply "standards") from the Landolt (1992) catalog on nights deemed photometric. I determined photometric quality nights using available weather and satellite data and consultation with the on-site operators. However, an on-site assessment of photometric conditions is notoriously unreliable. Upper

[1] http://www.soartelescope.org/observing/documentation/soar-optical-imager-soi/soi-manual/soi_toc

Table 2.2. Summary of observations

| Object | First Night/ Last Night (UT) | Total Nights | Filter | Exposure Times (seconds) | Total Times (seconds) | Mean Seeing (arcseconds) |
|---|---|---|---|---|---|---|
| AM 1 | 2007-10-08 | 10 | V | 28×300 | 8400 | 0.87 |
| | 2009-01-31 | | | 33×600 | 19800 | 0.76 |
| | | | | | 28200 | |
| | | | B | 27×500 | 13500 | 0.90 |
| | | | | 25×900 | 22500 | 0.78 |
| | | | | | 36000 | |
| Pyxis | 2007-11-14 | 11 | V | 3×15 | 45 | 0.76 |
| | 2009-01-31 | | | 72×300 | 21600 | 0.79 |
| | | | | | 21645 | |
| | | | B | 3×30 | 90 | 0.89 |
| | | | | 60×500 | 30000 | 0.84 |
| | | | | | 30090 | |
| PG 0231 | 2008-01-03 | 1 | V | 3×20 | 60 | 0.86 |
| | | | B | 3×30 | 90 | 0.86 |
| | | | | | 150 | |
| SA 98 | " | " | V | 3×4 | 12 | 0.75 |
| | | | B | 3×5 | 15 | 0.86 |
| | | | | | 27 | |
| Rubin 149 | " | " | V | 1×3 | 3 | 0.70 |
| | | | | 1×4 | 4 | 1.01 |
| | | | B | 1×4 | 4 | 1.27 |
| | | | | 1×30 | 30 | 1.08 |
| | | | | | 41 | |
| PG 0918 | " | " | V | 2×5 | 10 | 1.03 |
| | | | B | 1×6 | 6 | 0.98 |
| | | | | 1×15 | 15 | 1.01 |
| | | | | | 31 | |

atmosphere cirrus clouds are invisible to the unaided eye and can creep in at any point during the night. The following quote from John Irwin (1952) summarizes the observer's frustration.

> One might ask: "How clear a sky?" The answer is: "Just as clear as possible-*the best is none too good.*" The photocell can "see" and respond to thin cirrus clouds long before they become apparent to the naked eye. Such clouds are worse than a nuisance; once they have intruded themselves into the observations their effects are subtly injurious to the scientific interpretation and are difficult to eradicate. At the Goethe Link Observatory we call such clouds "photoelectric poison."

True photometric conditions are most reliably verified post analysis (more details about this in Chapter 4). Therefore we observed standards on multiple nights until we were confident we had a truly photometric night. This turned out to be the night of 2008-01-04. Table 2.1 lists the standards observed that night.

## 2.2 Data Reduction

Image processing refers to the methods of removing the systematic effects of the instruments from the images. Such systematic effects include a bias offset introduced to the analog to digital converter (ADC) that prevents it from reading a negative number as well as imperfections in the optical train, most commonly dust or scratches on the mirrors, that distort the final image.

I processed the data using the Image Reduction and Analysis Facility (IRAF[2], Tody 1993, and references therein). IRAF is an operating environment tailored for Flexible Image Transport Standard (FITS, Pence et al. 2010) data files commonly used in astronomical

[2]IRAF is distributed by the National Optical Astronomy Observatories, which are operated by the Association of Universities for Research in Astronomy, Inc., under cooperative agreement with the National Science Foundation.

applications. It consists of a collection of tasks (or programs) grouped into packages. Each task receives input from the user through parameters. In this section, all words in the `typeset` font refer to IRAF tasks. Typeset words connected by a period refer a parameter of a task For example, `ccdproc.statsub` refers to the `statsub` parameter of the `ccdproc` task.

### 2.2.1 Calibration

The following is a summary of the calibration process based on IRAF CCD documentation by Massey (1997) to which I refer the reader for details about the tasks below.

#### Bias Subtraction

In order to correct for the CCD pixel to pixel bias variations, we acquired a sequence of 10–20 bias (also called zero due to their exposure time) frames at the beginning of each observing run, which `zerocombine` combined into a single, averaged image. In order to account for cosmic rays infiltrating the images, all combination algorithms for the bias and flat frames discussed below had the `reject` parameter set to `minmax`. This master bias frame was subsequently subtracted from all the images using `ccdprocess`.

#### Flat Field Correction

Broadly speaking, flat fielding refers to the process of removing imperfections in the optics train that cause distortions in the final image and pixel-to-pixel variations in detective quantum efficiency (DQE). The idea is to have the telescope image a uniformly illuminated area with an exposure sufficient to provide enough signal to be clearly distinguished from the background while also not saturating the CCD.

There are two methods for obtaining flat field images ("flats"). The first involves mounting a screen on the dome and illuminating it with one or more lamps. The telescope then images

the screen to obtain what are commonly called "dome flats". The advantage of this technique is that the uniformly illuminated, featureless field free of extraneous signal. However, dome flats in short wavelength filters, such as $B$, suffer a lower SNR due to the comparative lack of flux of blue light from the lamp. In principle, this could be addressed with longer exposure times at the risk of greater hits by cosmic rays.

Incandescent lamps are relatively faint in blue, broadband filters due to the steep drop off in the blackbody spectrum as wavelength decreases past the effective temperature of the lamp. Solutions include using incandescent lamps with a hotter effective temperature and fluorescent bulbs made with gasses with strong blue emission lines. The temperatures required of the filament to produce such a blue spectrum make incandescent bulbs expensive and short lived, and fluorescent bulbs only approximate a continuous spectrum with a dense blanket of emission lines making them less than ideal for broadband filters.

The alternative is to image the sky itself during twilight. The daytime sky is actually violet, but we perceive it as blue because are eyes are less sensitive to violet wavelengths (Smith 2005). However, the sky is far too bright to image during the day with a four meter class telescope. Therefore, we began imaging the flats as soon as the sun set, starting with the shortest wavelength filter and working our way redward as the sky turns from blue to red.

Because SOI has a 16 bit ADC, its gain is set such that ADC saturation occurs before physical the detector's response becomes non-linear (somewhat near to, but less than, the point of physical saturation). Saturated pixels have a value of 65,535 counts; the maximum value of an unsigned 16 bit integer. To reduce the risk of high transparency regions of the image saturating, we obtained flat field images with median levels less than half that value, or between 20,000 and 30,000 counts per pixel. We insisted on acquiring enough flats such that the sum of the median levels of all the individual flats exceed 100,000 counts (typically at least five flats per filter).

A complication that arises when the shutter transfer time, the time it takes for the shutter to open and close, becomes significant compared to the total exposure time. For example, in an iris style shutter, pixels first illuminated as the shutter open acquire more signal creating a gradient on the flat field image that artificially diminishes signal upon application to the science frames. SOI has a "focal-plane" style shutter, a two curtain system each of which sweeps across the chip in the same direction, with a 60 millisecond transfer time. This design purposely minimizes the effects of extra illumination as the first pixels exposed by the opening curtain are also the first to be blocked by the closing curtain. To limit the maximum illumination variation to 0.5%, I insisted on a minimum exposure time of four seconds.

Light from stars dominating over the sky brightness is a risk with sky flats. When imaging the sky, photons from stars and galaxies reach the detector, but their signal tends to be weak compared to the much brighter sky. As the sky darkens during the flat acquisition process, stellar light images become significant compared to the sky leading to artifacts in the flats that could corrupt the final science frames unless accounted for. To correct for this the telescope operators slightly changed the telescope's position between sky exposures, a process called "dithering". Dithering causes whatever star light that appears in the flat images to appear in different locations from frame to frame. The flat field processing algorithms, `flatcombine`, assumes patterns that change position from frame to frame are stars and removes them during construction of the final flat image. We used sky flats exclusively during this campaign, however, dome flats were often acquired each night to serve as backups.

The flat field images were bias subtracted using `ccdprocess` with the `ccdproc.zero` parameter set to the master bias frame constructed previously. These images were then combined into a single, averaged image for each filter using `flatcombine` which works similarly to `zerocombine` but is designed to identify and filter out star light provided the telescope position changed from exposure to exposure.

Finally, I bias subtracted and flat field corrected the science frames using `ccdprocess`

configured to be aware of the master zero and flat field images. Additionally, `ccdprocess` trims away the overscan regions (more details about this in Section 2.5.)

### Cosmic Rays

Debate continues regarding the origin of cosmic rays (Ackermann et al. 2013), but suffice it to say that they are an unavoidable consequence of astronomical data acquisition manifesting as strong spikes or streaks in the image. `IRAF` image processing software is capable of detecting and removing them whenever images are combined using the `combine` parameter set to `ccdclip` or `minmax`. As both `zerocombine` and `flatcombine` average images, cosmic rays are removed from the master zero and flat images. However, because the detection of variable stars requires photometry of all cluster images, the science frames are not combined and cosmic rays persist. The PSF photometry software sufficiently distinguishes stars from other sources such as cosmic rays as to not corrupt the final measurement (see §2.3.2.)

### Image Mosaic

Because SOI has four separate readout amplifiers, the raw data consist of a single FITS file which is actually a stack of four, 512x2048 images that `soimosaic` combines into a single 2099x2048 image using. To account for the physical gap between the chips, 51 pixel columns are added between amplifiers two and three by setting the parameter `soimosaic.xgap = 102` (this parameter accepts values as unbinned pixels which are scaled according to the binning read from the image header). The upper left panel of Figure 2.1 is an example of a portion of the finished product.

## 2.3 Photometry

Photometry refers to the process of measuring the apparent brightness of a star after correcting for the sky brightness and light from nearby stars (“blending"). The photometry was

performed using the DAOPHOT/ALLSTAR/ALLFRAME software suite by Peter Stetson (1987). The choice of photometry software was largely influenced by the side-by-side comparisons of several algorithms performed by the Large Synoptic Survey Telescope (LSST, Becker et al. 2007) group who concluded DAOPHOT/ALLFRAME superior for crowded fields.

`DAOPHOT` is similar to `IRAF` in that it is an operating environment for launching commands (or tasks). In this section, with the exception of `ALLSTAR` and `ALLFRAME` which are standalone applications, all words in the upper case `TYPESET` font refer to `DAOPHOT` commands. Lower case `typeset` words refer to parameters.

### 2.3.1 Aperture Photometry

Aperture photometry is the simplest and most accurate method for measuring the brightness of a star, but it only works in sparse fields where blending of stellar images is negligible. In the simplest form, the software sums up all the light signal in a circular aperture centered on the peak of the star. Provided the aperture is of sufficient radius to collect all the light of the star but small enough to not be infected by light from nearby stars or background galaxies.

Absent light from nearby stars, one must then remove light from the sky itself. The sky is not completely dark even after the sun is more than eighteen degrees below the horizon and direct scattering of sunlight ceases (i.e. the onset of "astronomical twilight"). Sources of sky brightness include solar wind induced airglow that varies with time, zodiacal light (scattering of sunlight off of interplanetary dust) that is time and position dependent, and light from faint background sources (e.g. stars, galaxies, etc.) It manifests itself as an additive constant to the stellar profile. Time averaged values of sky brightness at CTIO[3] are $22.81 \pm 0.01$ in $B$ and $21.79 \pm 0.01$ in $V$. Any star fainter than these values are dominated by the noise

[3] `http://www.ctio.noao.edu/site/pachon_sky/`

introduced by the sky.

To subtract off the sky brightness, the software measures the light in a circular annulus, concentric with the aperture, whose inner radius exceeds the aperture. The outer radius of the annulus should be large enough to contain enough area to keep the SNR low but small enough to avoid the effects of blending. The area of the annulus should be smaller than the aperture to reduce the contribution of photon noise from the sky. The averaged value of light in the annulus becomes the measurement of the sky and is subtracted away from the total light contained in the aperture. The result should be a direct measurement of the total amount of light from the star.

All of the standard stars were measured in this fashion using `DAOPHOT`. The `FIND` command locates the center of the stars in the field. To keep things simple, the `threshold` parameter was set sufficiently high such that only the brightest objects in the field were identified. The resultant catalog was pruned by hand to only include the standard stars. The `PHOT` command performed the photometry configured to use an aperture radius of 4.62″ (30 pixels), an inner annulus radius of 4.62″ (30 pixels) and an outer annulus radius of 5.08″ (33 pixels). These correspond to a total aperture area of 67 sq″ and annulus area of 14 sq″.

### 2.3.2 PSF Photometry

Aperture photometry is too difficult in crowded fields due to the effects of multiple stars within the aperture and starlight infiltrating the annulus. The remedy is to develop a model point spread function (PSF) and use it to simultaneously measure and subtract away stars. Development of the model PSF is a delicate procedure performed using `DAOPHOT`. I refer the reader to Stetson (1987) for details of the model itself and simply outline the procedure below.

The purpose of `DAOPHOT` is to develop a model PSF and a catalog of decent guesses for the central positions of the stars and their brightness. The program allows for a number of

choices for the PSF model which are detailed in Stetson (2000). I found success with the Moffat function which is, in Stetson's words, "something like"

$$\frac{1}{\left(1 + x^2/\beta_x^2 + y^2/\beta_y^2 + \beta_{xy}xy\right)^{\beta}} \tag{2.1}$$

where $x$ and $y$ are the coordinates of the center of the star and $\beta_x, \beta_y$, and $\beta_{xy}$ are free parameters based on the full width half maximum (FWHM) of the stellar profile. The $\beta$ term is a user specified fixed parameter that I set to 1.5 because it produced decent results (the other option is 2.5).

The first step is to identify everything in the image (or frame) that is a star (as opposed to background galaxies, cosmic rays, CCD chip defects, etc...) using the `FIND` command. For each night's worth of data, I toggled the `threshold` value, the multiple of the standard deviation of the average pixel value, or $\sigma$, above which a signal is considered a star, by a few tenths to get a consistent number of stars in the input guess catalog. For example, for AM 1, a typical value would be $2.8\sigma$ for 3,000 stars. For nights with poor transparency, I used reasonable values from previous nights and try to get consistent counts from frame to frame.

The initial positions file serves as the input for `PHOT` which produces the initial guesses for the brightness. As discussed in section 2.3.1, this procedure performs simple aperture photometry with an aperture of between $0.462''$ and $0.770''$ (3-5 pixels) depending on the seeing, and an inner and outer annulus radii of $2.31''$ and $3.08''$ (15 and 20 pixels) respectively.

The choice of aperture and annulus radii serves to achieve a reasonable first guess at the brightness of the star while mitigating the effects of the crowded field. The choice of such a narrow aperture limits the inclusion of light from neighboring stars and non-stellar artifacts at the expense of underestimating the star's brightness by including a relatively small portion of the stellar profile. The annulus almost certainly contains light from nearby stars, but the relatively large area typically contains more sky and hence dominates the average. By the inclusion of quite a bit of light from blended stars, the result overestimates

the sky brightness. The ultimate guess, while being far from perfect, suffices most of the time. When the initial guess is too far off, the model does not converge, but by allowing the brightness guess to vary with successive iterations, the algorithm eventually achieves a solution.

The next step is to select a group 20-30 candidate stars, referred to herein as "PSF stars," used to create the PSF model for the frame. Because the parameters of the model are designed to optimize the fit for the PSF stars and are allowed to vary via a quadratic function of position for remaining stars, it is important that they are uniformly distributed spatially, relatively isolated from other stars and are bright enough to give provide good SNR on nights with poor transparency while not being so bright as to saturate on nights of good seeing. Whenever possible, I used the same stars for each target from night to night, but pointing variations sometimes excluded certain stars from the image.

Table 2.3 shows the PSF stars used for the master frame of AM 1, which served as the PSF stars for the majority of the frames. Replacements became necessary whenever stars on this list wander off the chips or into unuseful regions, such as the guide star probe shadow or the gap between CCDs, due to night-to-night pointing variations. The stars in this table are calibrated to the standard system via the procedure outlined in §3.1. Calibrated magnitudes for these stars, of course, were unknown *a-priori*. I estimated relative brightnesses using stellar radial profile plots in `IRAF`.

With the initial list of candidate PSF stars, `PSF` computes an initial PSF model and identifies neighboring stars whose profiles could corrupt the PSF stars. With this in hand, I used `GROUP` and `NSTAR` to perform photometry on the PSF stars and neighbors. As a quality assurance (QA) check, `SUBSTAR` subtracts away all the PSF stars and their neighbors. Should anything go wrong with the PSF model, the subtracted image showed distortions and other defects.

The PSF stars were inspected by hand and problematic stars deleted from the list of

Table 2.3. An Example of PSF Stars for AM 1

| ID | $\bar{X}$ (pixels) | $\bar{Y}$ (pixels) | $V$ | $(B-V)$ | $\sigma_V$ | $\sigma_{(B-V)}$ |
|---|---|---|---|---|---|---|
| 169 | 1858.82 | 87.70 | 19.891 | 1.370 | 0.0008 | 0.0014 |
| 10161 | 652.45 | 168.60 | 20.735 | 0.650 | 0.0009 | 0.0013 |
| 10212 | 1944.58 | 248.93 | 19.491 | 0.705 | 0.0007 | 0.0011 |
| 432 | 1210.97 | 251.04 | 21.001 | 0.600 | 0.0012 | 0.0018 |
| 30182 | 615.84 | 262.45 | 19.985 | 0.163 | 0.0007 | 0.0010 |
| 10294 | 1945.64 | 301.12 | 20.189 | 1.565 | 0.0009 | 0.0017 |
| 681 | 314.11 | 382.76 | 21.372 | 1.460 | 0.0014 | 0.0032 |
| 683 | 636.17 | 385.11 | 20.860 | 0.839 | 0.0010 | 0.0016 |
| 1260 | 269.94 | 619.77 | 20.645 | 0.658 | 0.0009 | 0.0013 |
| 10649 | 591.58 | 670.80 | 19.473 | 1.056 | 0.0006 | 0.0010 |
| 1916 | 201.74 | 775.61 | 20.481 | 0.827 | 0.0009 | 0.0013 |
| 11323 | 1544.91 | 884.09 | 17.570 | 0.980 | 0.0006 | 0.0009 |
| 11550 | 791.54 | 927.78 | 19.368 | 1.443 | 0.0007 | 0.0011 |
| 11807 | 231.95 | 1048.58 | 19.940 | 0.948 | 0.0007 | 0.0011 |
| 3456 | 806.96 | 1124.92 | 20.971 | 0.593 | 0.0012 | 0.0018 |
| 21293 | 669.60 | 1159.29 | 18.416 | 0.916 | 0.0005 | 0.0008 |
| 3745 | 1291.03 | 1249.45 | 21.829 | 1.697 | 0.0021 | 0.0056 |
| 12045 | 485.92 | 1299.15 | 20.371 | 1.484 | 0.0009 | 0.0017 |
| 31194 | 1399.85 | 1436.67 | 17.150 | 0.607 | 0.0006 | 0.0009 |
| 4112 | 1246.74 | 1455.72 | 21.055 | 1.378 | 0.0014 | 0.0028 |
| 4133 | 482.44 | 1467.26 | 20.601 | 1.600 | 0.0010 | 0.0021 |
| 31230 | 1782.21 | 1498.57 | 19.678 | 1.349 | 0.0007 | 0.0013 |
| 4534 | 1652.78 | 1732.76 | 20.917 | 0.822 | 0.0011 | 0.0018 |
| 12374 | 209.27 | 1758.80 | 17.625 | 0.979 | 0.0006 | 0.0009 |

candidate PSF star list for a second iteration of the above procedure. In almost all cases, cosmic rays persistent in the science frames hitting within the 2.31″ (15 pixel) `psf radius` of a star caused these distortions. Recall the procedure for cosmic ray removal involves combining images which violated a project goal of variable star detection. If the second subtracted image looked clean of anomalies, a final image was created that included PSF stars with their neighbors subtracted away. This image was used to create the final model PSF file which, along with the initial aperture photometry file created by `PHOT` serve as input for `ALLSTAR`.

Unlike `NSTAR` which optimizes the PSF parameters for specific stars, `ALLSTAR` uses the initial guesses of position and brightness as well as the PSF model for the frame to perform photometry for all the stars in the frame. For each iteration of `ALLSTAR`, the program applies the PSF model to as many stars that will converge and subtracts them away. Subsequent iterations have fewer stars to cause blending, hence more stars will converge. The process

continues until all stars in the frame converge up to a maximum of 200 iterations. The program then produces a catalog of final positions and magnitudes plus an image with all the converged stars subtracted away as a QA check. An example of an `ALLSTAR` subtracted image can be found in the upper right panel of Figure 2.1.

### 2.3.3 Automation

The above procedure is rather slow and tedious to perform by hand. Therefore, I wrote three perl scripts to automate the procedure. In this section, words in `typeset` refer to scripts that I wrote. Source code for these scripts may be found in Appendix B.

Prior to invoking the scripts, the user must run `FIND` to set an appropriate threshold, the run `PICK` to generate the list of 500 candidate PSF stars which serves as the input for the upstream scripts.

The first two scripts aid in selecting the PSF stars and marking their positions in an image display such as SAOImage DS9 (Joye & Mandel 2003), developed at the Smithsonian Astrophysical Observatory. The first script, `daopsffind`, selects the PSF stars based on the initial guess coordinates of the PSF stars in the previous frame. The algorithm is pretty simple; find the brightest star within the user specified search radius centered on the coordinates of that star in the input list. Provided the pointing is stable over the course of the night, the algorithm works well enough to identify the same PSF stars in each image. Frequently, the PSF stars for the first frame of the night were chosen by hand, which served as the input guess list for the next frame. That frame's final list served as the input for the next frame and so on. Next, `daopsfmark` simply reads the list of PSF stars output by `daopsffind` and generates a DS9 formatted region file that draws a circle around each PSF star in the image display and labeled it according to it's catalog ID. Despite being relatively simple scripts, automating this process saved the greatest amount of human effort compared to the other automation scripts discussed in this subsection.

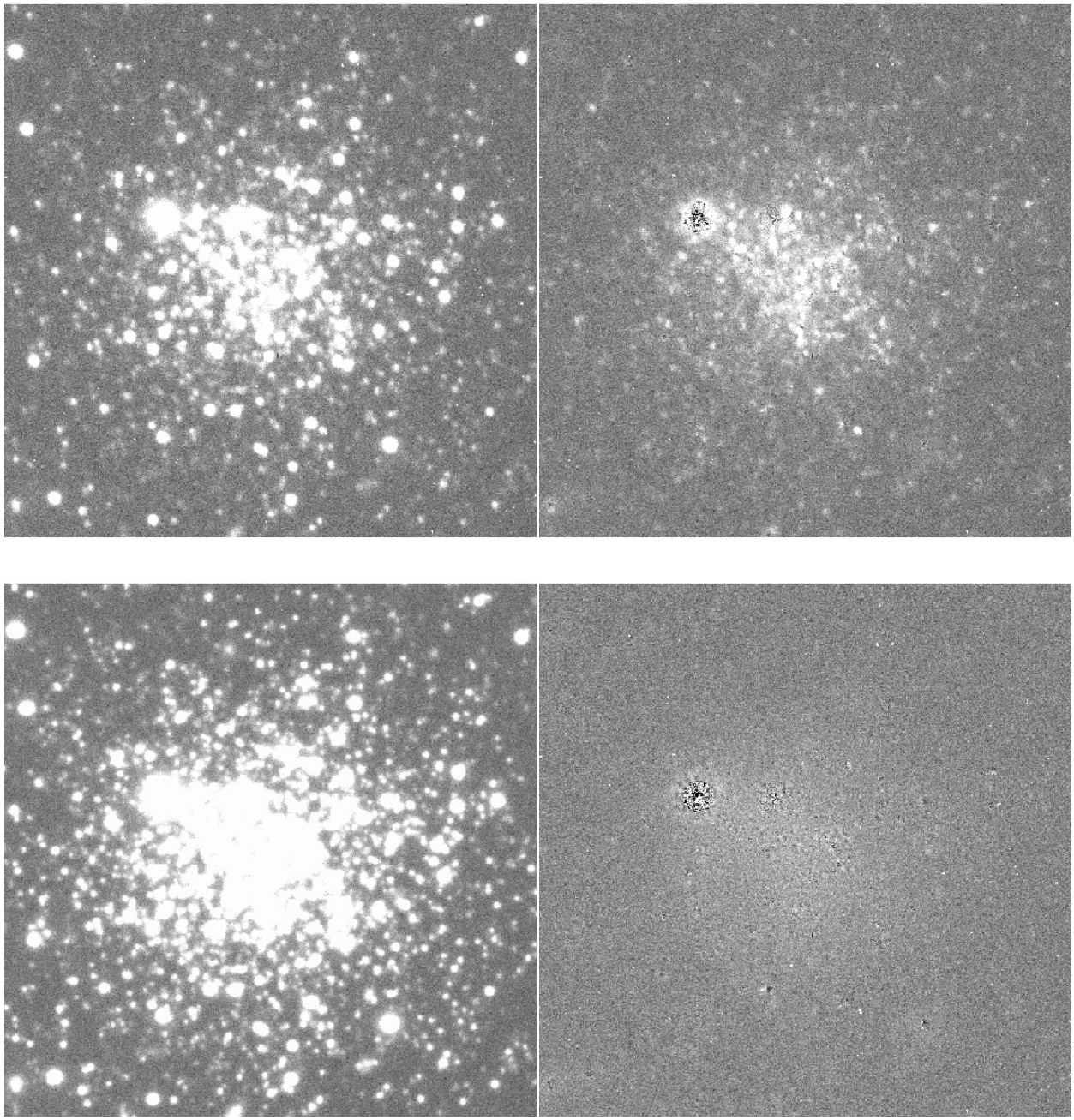

Figure 2.1 The central $2' 27''$ region of AM 1. *Upper left:* An example of a bias subtracted, flat field corrected frame. This particular frame served as the master for the $V$ portion of `ALLFRAME` reductions. *Upper right:* The same frame after `ALLSTAR` subtraction. *Lower left:* The median of 17 V frames. *Lower right:* Same as above but after `ALLFRAME` subtraction.

Finally, the input catalog of guesses at positions and magnitudes returned by `FIND` as well as the list of PSF stars serve as input to `daofun` (for lack of a better name) which automates the `DAOPHOT` command sequence. After the first iteration, the script prompts the user to inspect the image where the PSF stars and their neighbors are subtracted and delete stars that failed to cleanly subtract away from the next iteration's PSF list. Typically, less than five stars per frame needed to be culled from the list prior to the second iteration. After the second iteration, the user is again prompted to inspect the image with the remaining PSF stars subtracted away. Provided this subtracted image satisfies the user, the script invokes `DAOPHOT` to construct the final PSF model and subsequently calls `ALLSTAR` to perform the final photometry of the field.

## 2.4 Catalog Assembly

The final step is to compute the global solution for all the stars in all the frames simultaneously using `ALLFRAME`. The specifics of how the algorithm works are detailed in section 3.2 of Stetson (1994), to which I refer the reader for further information. The steps listed below follow the instruction outlined by Anne Turner (1997). In this section, words in the upper case `TYPESET` font refer to stand alone programs related to `ALLFRAME` and `typeset` font words refer to parameters to those programs.

### 2.4.1 Crude Position Registration

The first step is to register the stars in all of the images to the coordinate system of a master frame. Because the PSF can vary as a function of color, I chose to run the full `ALLFRAME` procedure on $B$ and $V$ frames separately. Hence there was a master $B$ as well as a master $V$ frame, which were the best seeing frames the night that photometric transformations were derived (2008-01-04 UTC). The specific frames used as the master frames in each filter for both closers are indicated in the "Comments" column of the observing tables

in Appendix A.

DAOMATCH makes a crude estimation of the positional transformations of of each frame to the system of the master frame using simple linear functions[4] of the form

$$x_2 = A + Cx_1 + Ey_1 \tag{2.2a}$$

$$y_2 = B + Dx_1 + Fy_1 \tag{2.2b}$$

where $A$ and $B$ are offset terms and the rest are rotational terms. The only significant rotational offsets between frames was the occasional 180 degree rotation angle caused by the telescope pointing significantly west of the meridian. I accounted for this by inverting the image's axes using IRAF prior to performing photometry on the frames. Hence, as far as DAOMASTER is concerned, there is virtually no rotational offset between frames, and the terms $C - F$ in equations 2.2 are close to zero.

The linear offset terms, $A$ and $B$, were significant. Pyxis is large enough that we consistently pointed the telescope at the center of the cluster, but AM 1 is small enough to fit on a single CCD. Most nights we centered AM 1 on the left chip, but there were some nights where it was centered on the right chip requiring a $\sim 1000$ pixel offset term. This becomes significant when executing DAOMASTER discussed below.

### 2.4.2 Fine Position Registration

The crude offsets computed by DAOMATCH serve as inputs to DAOMASTER in order to compute the final transformations. Per Turner's recommendations, the parameters `minimum number, minimum fraction` and `enough frames` were set to 5, 0.5 and 10 respectively. I

[4]These functions and associated documentation are found in the `ccdpck.man` file included with the source code.

used a `maximum sigma`[5] of 0.5 in order to reject problematic stars. Finally, because there are offsets between frames greater than tens of pixels, I configured the program to use a cubic transformation function (option 20 in `desired degrees of freedom`).

The next step in `DAOMASTER` is to chose an initial critical match-up radius, which allows the software to handle for high proper motion stars that deviate from their average position significantly from frame to frame. Both Stetson and Turner recommend starting with an initial critical radius no greater than seven and step down by one each iteration, repeating the final iteration of one until the number of stars within the radius remains the same. However, my initial interpretation of the documentation led me to believe it was to account for large shifts between frames. At first I tried a pathological number on the order of 100, which gave the program enough freedom to assign errant matches (or as my notes put it, enough rope to hang itself). This led to half moon shaped artifacts in the final `ALLFRAME` subtracted images, which are the ultimate QA check discussed in section 2.4.4. This problem was difficult to diagnose, but, in the end, following the documentation's advice of a maximum radius of seven worked great.

### 2.4.3 Median Images

The last step before invoking `ALLFRAME` is to create a median image whose photometry serves as the initial guess for the final solutions. I selected at least ten frames with the best seeing to compute a median image for each filter using `MONTAGE2`. The specific frames used to construct the mediated image are indicated in the "Comments" column of the observing logs in Appendix A. The program subtracts away the sky and sometimes introduces catastrophically large (greater than $10^{17}$) pixel values, presumably due to a divide-by-zero style error. Both of these are corrected using `IRAF`. Then the $B$ and $V$ median images are co-added to

[5]Quoting Peter Stetson's description of this parameter from the file `ccdpck.man` included with the source code, "A star will be rejected if its mean instrumental magnitude, based on a weighted average of all available observerations corrected to the magnitude scale of the "best" frame, is larger than the number you type in."

form the final median image, an example of which is shown in the lower left panel of Figure 2.1.

The final step is to process the combined median image through `DAOPHOT` and `ALLSTAR` to produce the final catalog of initial guesses of positions and magnitudes. To decide the `threshold` value for the detection limit, Turner recommends plotting number of stars vs. `threshold`, which looks like a half gaussian, and choosing the value where the elbow in the curve occurs. For AM 1, this occurred at a threshold of 2.6. `ALLSTAR` produces an image with all the stars it detected subtracted away, Turner recommends running this through the whole process again to pick up any stars not detected the first time around. I ended up doing four iterations of this process for each cluster. To avoid identification collisions between stars in each iteration, I introduced a catalog identification index offset in increments of 10,000 in each iteration (eg. stars whose catalog ID in the range 30,000 – 39,999 were detected in the third iteration). It is best to have as many stars as possible as errant detections do not converge in `ALLFRAME`.

### 2.4.4 `ALLFRAME`

After executing all the steps above, executing `ALLFRAME` is fairly straightforward. I used the parameters recommended by Turner but with the `sky radius` values changed to match what I used for `ALLSTAR`. It is important to note that `ALLFRAME` is initially configured to only allocate memory sufficient to store images of a maximum size of $2048 \times 2048$ pixels. When accounting for the physical gap, my images are $2048 \times 2099$ pixels. It is relatively straight forward to recompile `ALLFRAME` to increase the limit, and the procedure is included in the documentation accompanying the source code.

`ALLFRAME` produces two output files for each input frame; a final catalog for all the stars that converged in the frame and a image with the stars subtracted away for QA. In order to produce the final, averaged color magnitude diagram (CMD), all the $B$ and $V$ frames

are averaged separately using DAOMASTER. This accomplished by editing the original transfer file produced by the first run of DAOMASTER and changing the filenames to point to the new ALLFRAME produced catalogs. Furthermore, the file needs to be split into two files based on filter. These are input to DAOMASTER to produce a file with mean magnitudes and scatter for each filter. The magnitudes of the stars in each frame are shifted by means of a constant offset to the magnitude system of the master frame of each filter. One final iteration of DAOMATCH and DAOMASTER combines the averaged magnitudes into a single catalog as well as a transfer file that references each star's identification in the two averaged catalogs.

### 2.4.5 Aperture Correction

Different techniques determine the magnitude of the standard stars and cluster stars; aperture and PSF respectively. With PSF photometry, DAOPHOT constructs a model heavily dominated by the brightest portion of the stellar profile where the SNR is strongest. Once the model is constructed, magnitudes are evaluated by adjusting a scale factor on a star-by-star basis to this profile which simultaneously produce matches to all the stars in the image. In the end, the software outputs relative magnitudes between the stars in that image alone. Thus, each frame lacks an absolute zero point for the magnitude system.

Standard stars are measured via aperture photometry where, after the sky is reasonably measured and subtracted away, photons are counted within the aperture region measuring a total intensity. The wings of the stellar profile typically extend several arcseconds in radius from the center of the star (Stetson 1990), but the apertures for standards are chosen such that the total percentage of light excluded in the wings beyond the aperture is small compared to the expected 1% error budget[6]. This technique contains an absolute zero point for the magnitude system; a region in which no net flux is measured, for example.

In order to establish a consistent magnitude system for the standard and cluster stars, one

[6]Assuming a simple gaussian function for the stellar profile and a FWHM seeing of 1″, the 4.62″ aperture radius used for the standards contains 99.9996% of the total starlight.

must measure and apply a constant offset in brightness known as an "aperture correction." I used the curve of growth technique described by Stetson (1990) to determine the aperture correction for each of the master frames. Application of the aperture correction to the master frames suffices as these frames determine the magnitude system for all subsequent frames.

To summarize the technique, a selection of local standard stars are measured using twelve concentric aperture *radii* ranging from the aperture used by the `PSF` function (0.462″) out to at least half the radius of the aperture used for the standards (4.62″). The PSF stars used in `DAOPHOT` described in section 2.3.2 serve this purpose well. Stetson (1990) lists two techniques for determining the aperture radius sequence; a geometric relationship and recursive sequence I call "fourth night" because Stetson first used it on data obtained from the fourth night of an observing run at Cerro Tololo. Though he claims both techniques work well, he expresses a preference for the latter, the general form of which is

$$r_k = r_{k-1} + \frac{(k-1)\,(r_{12} - r_1)}{66} \tag{2.3}$$

where $r$ is measured in units of pixels. Side by side comparisons of each technique on my data verify Stetson's assertion about the fourth night technique. For my data, I used $r_1 = 3$ and $r_{12} = 20$. The program extrapolates the magnitude out to an effective aperture of twice the greatest input aperture. In my case, the extrapolated magnitude has an effective aperture radius of 6.16″, easily greater than the aperture used for the standards.

Before performing the photometry, I used `DAOPHOT` and `SUBSTAR` to subtract away everything in the frame except the local standards. Furthermore, I removed any local standard with a cosmic ray hit within the greatest aperture. A hazard I discovered when running `PHOT` is that if a model PSF file is in the same directory and with the same base name as the input file used, it will use it and make a PSF measurement of the local standards without informing the user. This is fundamentally incorrect as we wish to compare aperture magnitudes to the PSF magnitudes, not PSF to PSF. To avoid this, one should ensure that the input file has

Table 2.4. Final Aperture Corrections

| Target | V | B |
|---|---|---|
| AM 1 | -0.0611 ± 0.0004 | -0.0582 ± 0.0005 |
| Pyxis | -0.0706 ± 0.0003 | -0.0839 ± 0.0003 |

a different base name.

The concentric aperture measurements serve as input to the software `DAOGROW` to compute the curve of growth. The program outputs some data files used to make QA graphs shown in Figure 2.2. Its ultimate output file has the same base name as the input aperture file with a `.tot` extension. To get the aperture correction, one needs the "best" magnitude and the correction factor at that aperture. DAOGROW examines the curve from outside to in and locates the point at which the errors are minimized. This is the "best" aperture, and the cumulative correction factor, denoted in Turner (1997) as $\Delta$, is the summation of all the outer points plus an extrapolation factor. The result is a magnitude estimate for an aperture twice the radius of the largest aperture used to compute the curve of growth. In my case, my largest aperture is 20 pixels (3.08″), so the "best" magnitude corresponds to a magnitude measured with a 40 pixel (6.16″) aperture. The output file contains this magnitude in column 4 as well as an error estimate.

Next, to get the aperture correction for that frame, one invokes the following formula found in Appendix E of Turner (1997)

```
Ap cor = Mag (40 pixel aperture) - PSF mag
Mag (40 pixel aperture) = Mag (best aperture) + Growth curve correction.
```

The output file contains the `Mag (40 pixel aperture)` parameter, so all that is necessary is to subtract the PSF magnitudes for the local standards used in the input aperture magnitude file from the 40 pixel aperture magnitudes in the output file. The average value of the difference of all the local standards is the aperture correction. The final results are listed in

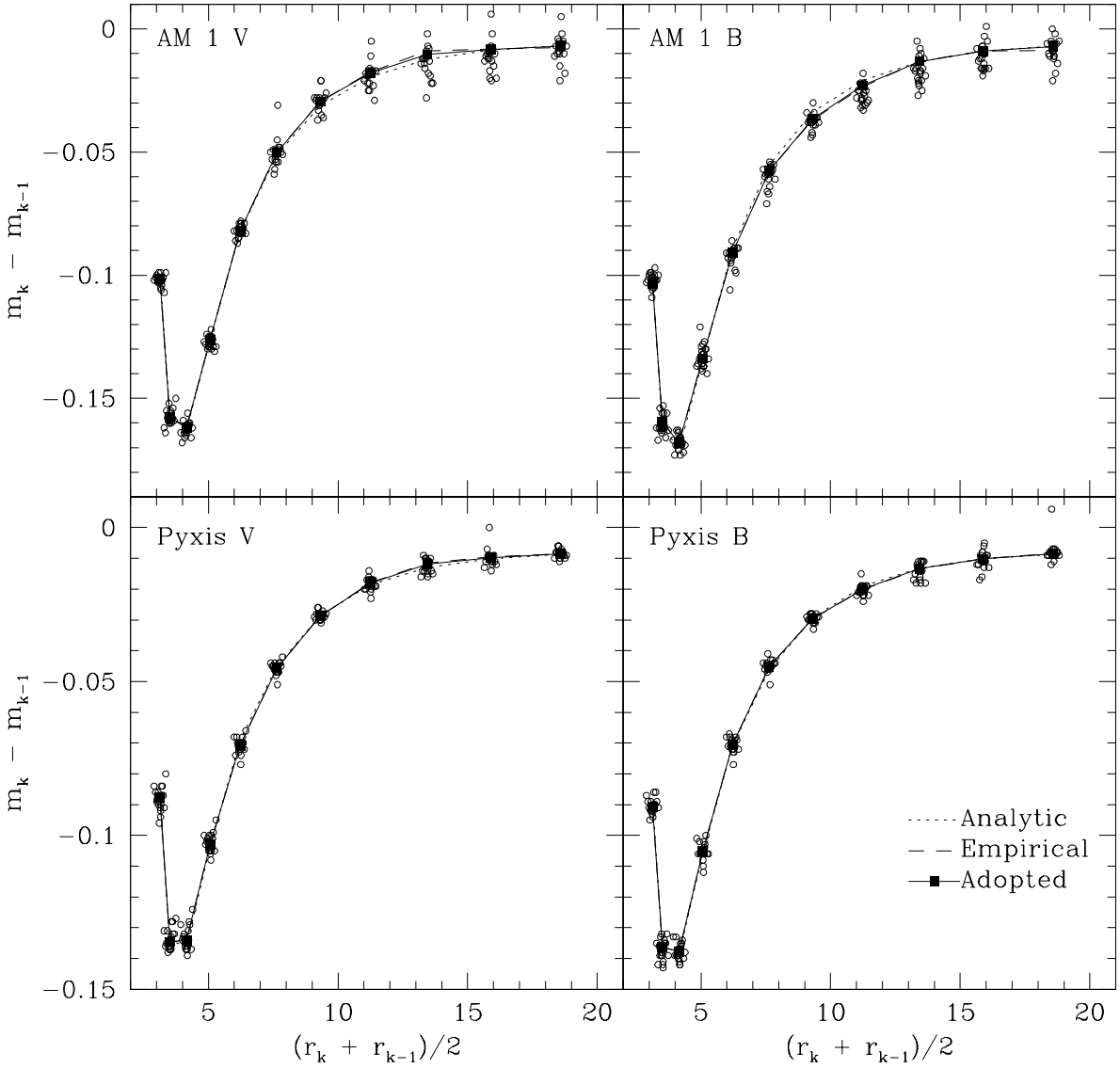


Figure 2.2 Curves of growth for both clusters in both filters. The open circles represent magnitude differences between adjacent apertures plotted versus the mean magnitude difference between the apertures in pixels. Artificial scatter is added to the horizontal scale to help distinguish the points. Fitting to the mean of the raw magnitude differences results in the empirical model and is more reliable for smaller apertures. Adjusting the parameters of an analytic function that best fits the stellar profile results in greater reliability at larger radii. The adopted model is the compromise between the two.

Table 2.4.

## 2.5 Reprocessing

Several suspicious anomalies persisted in the finished products after completing the process outlined above, the most flagrant of which being best described as "half moon" shaped residuals in the final, `ALLFRAME` subtracted images. See Figure 2.1 lower right panel for an example of a clean subtraction. These only occurred along the boundaries between the two amplifiers on each CCD chip.

After much investigation, I identified incorrect header keyword values used by `CCDPROC` to trim away the overscan region as the source of the problem. In particular, the values `BIASSEC, TRIMSEC,` and `DATASEC` were off by just a few pixels. Furthermore, these values changed with the installation of the new CCD on November 8th, 2008. This caused portions of the chip containing data to be trimmed away with the overscan region. The two amplifiers on each SOI CCD read out the chip in a theater-curtain style fashion, pulling the pixel columns left and right forming images containing 512 columns of data plus overscan regions on both sides. When `SOIMOSAIC` combined the data from each amplifier, the missing pixel columns along the boundary between the amplifiers formed discontinuities in the stellar profiles of the stars along that column. Hence the "half moon" shaped artifacts.

Sean Points, then a postdoc at SOAR, provided the proper header values. The correction required the complete reprocessing of all the data through `IRAF`, and a complete reanalysis of the AM 1 frames through the `DAOPHOT/ALLFRAME`. This served as a significant setback and a valuable lesson in data verification.

# Chapter 3

# The Color Magnitude Diagrams

This chapter describes the process that transforms instrumental magnitudes into a calibrated, filtered, color-magnitude diagram (CMD). Comparison of results with other observers as well as theoretical models necessitates calibration to a standard system. Furthermore, magnitudes on standard system facilitates an application of a bolometric correction to estimate the total luminosity of the stars from individual waveband data.

## 3.1 Photometric Calibration

Photometric calibration accounts for two broad categories of variation in measurement: atmospheric and instrumental. The apparent brightness and color of the star varies due to the atmosphere as the star transits across the sky, and instrumental differences arise due to dissimilarities between telescope optics and detectors at observatories and those used to calibrate the standard stars. In order to reconcile observations of the same stars from various observatories at different times, a correction for both effects must be applied.

The Earth's atmosphere extinguishes and reddens starlight through the processes of scattering and molecular absorption. The more atmosphere between the observer and space, the greater the effects. The sun and moon, for example, appear comparatively red when rising and setting. Fortunately, the atmosphere itself is fairly constant in time and easy to model, albeit with some exceptions; Landolt (1992) cites volcanic eruptions as an example of an event that significantly pollutes the atmosphere with extra reddening agents, but the effects from such episodes are short-lived with none occurring in the southern hemisphere during this observing campaign.

Beyond the effects of the atmosphere, the calibration technique must account for variations in instrument optics. The mirror surfaces and coatings have wavelength dependent reflectivity. For example, aluminum has a flat reflectivity response profile across optical wavelengths whereas silver has greater throughput in the red that drops off sharply at blue wavelengths[1].

The filters comprise the penultimate hurdle in the photons journey from star to detection. The filters are chosen and constructed to best match those used to establish the standard system. Figure 3.1 shows the total transmission response profiles for the SOI filters compared to those used by Landolt (1992) to establish the $UBVRI$ system. As is evident in the figure, the filters possess drastically different in throughput but have very similar central wavelengths and profile shapes.

Finally, the surviving photons face the detector; the instrumentation that converts photons into electrical signal. Detector technology varies widely with time beginning with photomultiplier tubes used to establish the standard system through improving generations of CCDs. The detectors possess wavelength dependent sensitivity and quantum efficiency. I am unable to produce a side-by-side comparison of the instrument response profiles due to the unavailability of the SOI data, but I refer the curious to compare Figure 52 of Landolt (1992) which shows the quantum efficiency of the photomultiplier used to establish the standard system as a function of wavelength with the same plot for the SOI CCDs found on the SOAR website[2].

Further complicating the issue are night-to-night variations in dust and other accumulations on the optics train that are not cleanly removed by the flat fielding process (§2.2.1). SOAR experiences a great deal of exposure to the elements when the dome shutter is open,

---

[1]The Gemini website contains figures comparing the wavelength response profiles for silver and aluminum. `http://www.gemini.edu/sciops/telescopes-and-sites/optics/silver-vs-aluminum`

[2]`http://www.soartelescope.org/observing/documentation/soar-optical-imager-soi/soi-manual/soi-hardwarde#H1` Figure 3.

allowing dust to accumulate on the mirrors. However, the most significant effects are due to nightly variations in atmospheric transparency. Because of this, the calibration procedure only applies to a single night's observations.

In order to reconcile the observational differences between different observing systems, one compares measurements of light from stars of known, or standardized, brightnesses. Landolt (1992) published a catalog of standard stars, roughly equally spaced in right ascension along the declination of the celestial equator for equal viewing opportunity in the northern and southern hemispheres.

The photometric calibration method outlined by Robert Hardie (1959), summarized in "Astronomical Techniques" edited by Hiltner (1962), has long been considered the standard for photoelectric photometry. Hardie derives the equations for computing the extinction and color coefficients for the $UBV$ filter system. The subsection below mirrors the steps and notation outlined by Hardie and derive the transformation coefficients for the $BV$ system.

### 3.1.1 Working Equations

The CCD detector, and subsequent measurement software described in §2.3.1, produces raw counts of photons collected during the exposure time. Dividing the two yields a quantity proportional to the intensity, $I$, of observed light. The intensities are scaled to the natural magnitude system via

$$m - m_0 = -2.5 \log \frac{I}{I_0} \tag{3.1}$$

where $m_0$ and $I_0$ are the magnitude and intensity of the arbitrary zero point of the system. For example, the star Vega was historically chosen to be the zero point of the magnitude system. Substituting an appropriate filter identifier in for the arbitrary magnitude, $m$, in Equation 3.1 defines the **instrumental magnitudes** as $b$ and $v$. One should not confuse these with the Stromgren photometric filters with the same names.

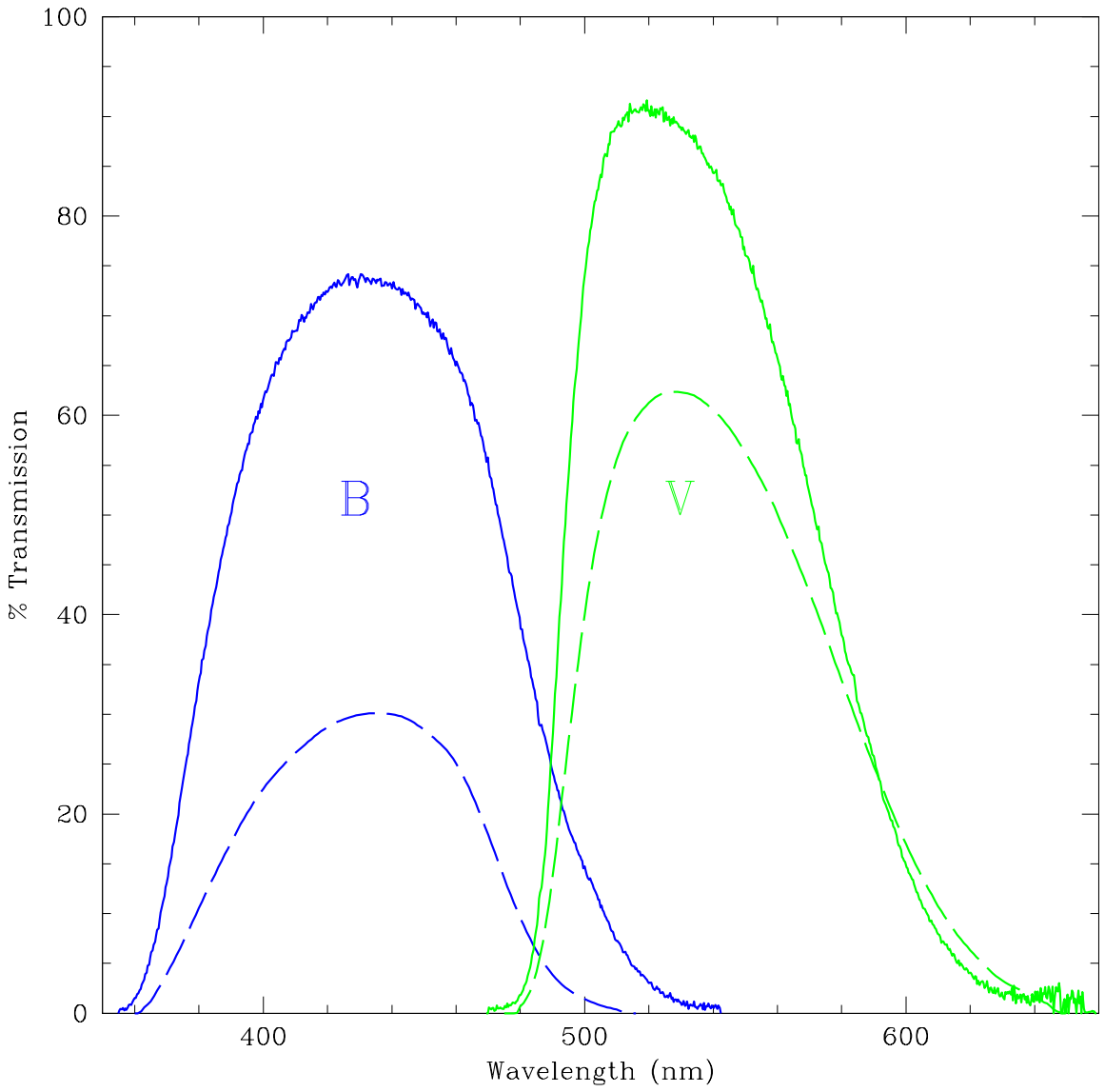


Figure 3.1 Filter throughput profiles for SOI circa October 2004 (solid lines) compared with those used by the Blanco 4m at CTIO to establish the standard system (dashed lines). Data for the SOI transmission curves are available from the SOAR website, and the CTIO data is from Tables 6 and 7 of Landolt (1992). The SOI filters have since been replaced, and updated transmission data are not yet available.

The first step in the process is to remove the effects of the atmosphere. Adopting a plane-parallel approximation for the atmosphere with a unit scale height above the observatory at the zenith, the **airmass**,

$$X = \sec z - 0.0018167\,(\sec z - 1) - 0.002875\,(\sec z - 1)^2 - 0.0008083\,(\sec z - 1)^3\,, \quad (3.2)$$

represents the relative thickness of atmosphere between the observatory and a star viewed at an angle $z$ away from the zenith. We restricted our observations to targets within 30 degrees of the meridian and altitudes sufficient to keep $z$ small enough to obviate the higher order terms in Equation 3.2. Hereafter, any mention of airmass refers to the approximation

$$X = \sec z. \quad (3.3)$$

In the equations that follow, any quantity with a 0 subscript represents an extinction-corrected, above atmosphere, instrumental magnitude. These **natural magnitudes**, defined as $b_0$ and $v_0$, are found via

$$v_0 = v - k_v^{'} X \quad (3.4a)$$

$$(b - v)_0 = (b - v)\, J_x - k_{bv}^{'} X. \quad (3.4b)$$

The color coefficient, $J_x$, is necessary due to the $\lambda^{-4}$ wavelength dependence imposed by molecular scattering (Hiltner 1962, §2.4). The mean wavelength shifts redward as the starlight encounters increased airmass, but shorter wavelengths are more strongly affected. This differential effect between the $B$ and $V$ filters is accounted for by measuring their relative brightness for a pair of stars of widely different color at low and high airmass. The functional form of this term is given by

$$J_x = 1 - k''_{bv}\, X, \tag{3.5}$$

and is stable enough over time to obviate recalibration on a nightly basis. The $k^{'}$ and $k^{"}$ terms are commonly called the first and second order extinction coefficients respectively.

Equations 3.4 and 3.5 provide an above-atmosphere, instrumental magnitude. The next step is to correct for the instrumental differences inherent to the telescope and detector, ultimately transforming to the standard system. We denote the standard magnitudes with capital letters, $B$ and $V$ given by

$$V = v_0 + \epsilon\,(B - V) + \zeta_v \tag{3.6a}$$

$$B - V = \mu\,(b - v)_0 + \zeta_{bv}. \tag{3.6b}$$

where the $\epsilon$ and $\mu$ terms are scale factors necessary to compensate for differences overall color sensitivity between the instrument used to establish the standard system and SOAR. These include differences in the central wavelengths of the filters, color sensitivity between the detectors, and color absorption on the mirrors. The $\zeta$ terms are offsets that correct for total throughput differences between the systems (Hiltner 1962, §3.1 – 3.3).

Combining equations 3.4 and 3.6 gives us our final transformation equations

$$V = v - k'_v\, X + \epsilon\,(B - V) + \zeta_v \tag{3.7a}$$

$$B - V = \mu_{bv}\,(b - v)\,J_x - \mu_{bv}\,k'_{bv}\,X + \zeta_{bv}. \tag{3.7b}$$

A close look at equation set 3.6 reveals the standard system as a linear transformation, in the $V$ band, from the natural system with $\epsilon$ and $\zeta$ being the slope and zero points respectively.

A small value of $\epsilon$ represents a decent match between the central wavelengths of the filters of the telescope and the standard system and is expected based on the comparison between the standard filters and those used by SOI shown in figure 3.1.

### 3.1.2 Determining coefficients

Section 4.3 of the Hardie chapter in "Astronomical Techniques" (Hiltner 1962) outlines the rigorous method for determining the atmospheric extinction coefficients. The process is summarized below.

The atmospheric reddening terms, the double-prime coefficients so called for the $k''$ notation, are determined by tracking two stars of different color over a wide range of airmass through the course of the night. The $k''_{bv}$ coefficient is equal to the slope of a linear fit of $\Delta(b-v)$ vs. $[X\,\Delta(b-v)]$, and similarly for the coefficients $k''_{vr}$ and $k''_{ri}$. These coefficients do not generally vary much with time, thus once they are determined, they need not be recomputed on subsequent photometric observing runs except for the occasional sanity check.

Furthermore, one can get a good estimate of the principle extinction coefficients, the $k'$ terms. The $k'_v$ is the slope of the line that fits $v$ vs. $X$. The $k''_{bv}$ is the slope of the line that best fits $(b-v)J_x$ vs. $X$. These initial estimates will be necessary in order to compute the color transformation terms, but they will be recalculated later once those terms are known.

The drawback of this technique is the enormous about of time one must spend observing standard stars. Hardie describes the "short" method that requires observations of two standards of widely different color at appreciably different airmass. If the color transformation terms and second order extinction terms are known, one can compute the principle extinction coefficients analytically using a two point difference method outlined below.

Table 3.1. CTIO Averaged Extinction Coefficients

| Magnitude or color index | Symbol | Average value | Range in values |
|---|---|---|---|
| V | $k_v^{'}$ | 0.152 | 0.099 – 0.250 |
| B-V | $k_{bv}^{'}$ | 0.124 | 0.074 – 0.184 |
| | $k_{bv}^{''}$ | 0.022 | - 0.046 – 0.013 |

Note. — Reproduced from Table 1 of Landolt (1992).

$$k_v^{'} = \frac{\Delta v - \Delta V + \epsilon \Delta (B-V)}{\Delta X} \tag{3.8a}$$

$$k_{bv}^{'} = \frac{\Delta [\mu J_x (b-v)] - \Delta (B-V)}{\mu \Delta X} \tag{3.8b}$$

This is effectively fitting a line to two points. Furthermore, Harris et al. (1981) describes a method that determines both the extinction and color transformation coefficients simultaneously via a matrix inversion.

Regardless of the technique used, direct determination of the atmospheric extinction coefficients requires extra observing time on standards. To maximize our observing efficiency, I used the time-averaged values for CTIO computed by Landolt (1992). Table 3.1, which is basically a reprint of Landolt's Table 1 with the notation changed, lists the values used for this project.

The color transformation terms, $\epsilon$ and $\mu$, are found by observing several standard stars, whose absolute magnitudes are known, at minimum airmass. The slope of the best fit line of $V - v_0$ vs. $B - V$ yields $\epsilon$. The $\mu$ term is found from the plot of catalog color index minus natural color index vs. catalog color index.

**The recipe**

The following is the step by step recipe for determining the coefficients given the averaged values of the extinction coefficients.

1. Compute the color transformation terms from the slopes of the following plots.

$$\begin{array}{rcll} \epsilon & \Rightarrow & V - v_0 & \text{vs.} \quad B - V \\ 1 - \frac{1}{\mu} & \Rightarrow & (B - V) - (b - v)_0 & \text{vs.} \quad B - V \end{array}$$

   If we denote the slopes of the above plots $m_v$ and $m_{bv}$, we can write the equations for the color transformation coefficients as

$$\epsilon = m_v \tag{3.9a}$$

$$\mu = \frac{1}{1 - m_{bv}} \tag{3.9b}$$

   And the uncertainties in the coefficients can be found from the usual propagation of error formula

$$\sigma_\epsilon = \sigma_{m_v} \tag{3.10a}$$

$$\sigma_\mu = \frac{\partial \mu}{\partial m_{bv}} \sigma_{m_b v} = \frac{1}{(1 - m)^2} \sigma_{m_{bv}} \tag{3.10b}$$

2. Finally, compute the color offset terms from the vertical-axis intercepts of the following plots.

$$\begin{array}{rcll} \zeta_v & \Rightarrow & V - [v_0 + \epsilon(B - V)] & \text{vs.} \quad B - V \\ \zeta_{bv} & \Rightarrow & (B - V) - \mu(b - v)_0 & \text{vs.} \quad B - V \end{array}$$

**Results**

The linear fits described above are shown in Figure 3.2, and Table 3.3 summarizes the resulting coefficients. As expected based on the close match between filter zero points of SOI and the standard system, the derived value of $\epsilon$ is small. One may be concerned with our choice of time-averaged extinction coefficients. A careful look at equation 3.7 reveals that any error incurred by using the time averaged coefficients rather than the correct values for that night manifests itself as an uncertainty in the slope of the graph used to determine $\mu$ term and the vertical intercept of the graph used to derive the $\zeta_v$ coefficient. As the errors of these values, listed in the fourth column of Table 3.3, are less than one percent, we see that our choice is none too perilous.

Finally, to test the quality of the results, I transform the instrumental magnitudes of the standard stars to the standard system and compare with the catalog values. As shown in table 3.2, the average difference between the catalog values, $V$ and $(B-V)$, and the derived values, $V'$ and $(B-V)'$, for the standards is zero with standard deviations of about one percent.

### 3.1.3 Uncertainties

One may have noticed a number of uncertainties, or errors, creeping up in the process of converting raw data to a final, calibrated measurement. These fall into two categories; internal and external errors.

Internal errors are inherent to the acquisition of star light and the instrument. Specifically they are the read noise of the detector, noise introduced by subtracting away the bias and the sky, and the photon noise of the star light itself. The photon noise, also known as "shot noise," comes about due to the particle nature of light. It is asymmetric and follows a Poisson distribution. For large numbers of photons, the noise is proportional to the square root of the number of photons detected. `ALLFRAME` takes all of this into account and reports an

Table 3.2. Standard star transformations from the night 2008-01-03

| Star | $V$ | $V'$ | $\Delta V$ | $(B-V)$ | $(B-V)'$ | $\Delta(B-V)$ |
|---|---|---|---|---|---|---|
| PG 0231+051 | 16.105 | 16.097 | 0.008 | -0.329 | -0.334 | 0.005 |
| PG 0231+051 A | 12.772 | 12.746 | 0.026 | 0.710 | 0.708 | 0.002 |
| PG 0231+051 B | 14.735 | 14.729 | 0.006 | 1.448 | 1.430 | 0.018 |
| PG 0231+051 C | 13.702 | 13.685 | 0.017 | 0.671 | 0.663 | 0.008 |
| PG 0231+051 D | 14.027 | 14.040 | -0.013 | 1.088 | 1.069 | 0.019 |
| PG 0231+051 E | 13.804 | 13.789 | 0.015 | 0.677 | 0.669 | 0.008 |
| SA 98 650 | 12.271 | 12.284 | -0.013 | 0.157 | 0.138 | 0.019 |
| SA 98 670 | 11.930 | 11.921 | 0.009 | 1.356 | 1.364 | -0.008 |
| SA 98 671 | 13.385 | 13.409 | -0.024 | 0.968 | 0.970 | -0.002 |
| SA 98 675 | 13.398 | 13.407 | -0.009 | 1.909 | 1.907 | 0.002 |
| SA 98 676 | 13.068 | 13.078 | -0.010 | 1.146 | 1.171 | -0.025 |
| SA 98 682 | 13.749 | 13.732 | 0.017 | 0.632 | 0.648 | -0.016 |
| Rubin 149 | 13.866 | 13.874 | -0.008 | -0.129 | -0.117 | -0.012 |
| Rubin 149 B | 12.642 | 12.636 | 0.006 | 0.662 | 0.662 | 0.000 |
| Rubin 149 C | 14.425 | 14.428 | -0.003 | 0.195 | 0.215 | -0.020 |
| Rubin 149 D | 11.480 | 11.480 | 0.000 | -0.037 | -0.015 | -0.022 |
| Rubin 149 E | 13.718 | 13.713 | 0.005 | 0.522 | 0.535 | -0.013 |
| Rubin 149 F | 13.471 | 13.486 | -0.015 | 1.115 | 1.141 | -0.026 |
| PG 0918+029 | 13.327 | 13.346 | -0.019 | -0.271 | -0.296 | 0.025 |
| PG 0918+029 A | 14.490 | 14.494 | -0.004 | 0.536 | 0.527 | 0.009 |
| PG 0918+029 B | 13.963 | 13.963 | 0.000 | 0.765 | 0.747 | 0.018 |
| PG 0918+029 D | 12.272 | 12.267 | 0.005 | 1.044 | 1.035 | 0.009 |
| | | Average | 0.000 | | Average | 0.000 |
| | | STDDEV | 0.013 | | STDDEV | 0.016 |

Note. — The primed magnitudes ($V'$ and $(B-V)'$) refer to our derived magnitudes. The unprimed magnitudes are Landolt's catalog values.

Table 3.3. Color Transformation Coefficients

| Magnitude or color index | Symbol | Value | Error |
|---|---|---|---|
| V | $\epsilon$ | -0.080 | $\pm$0.005 |
| | $\zeta_v$ | 0.474 | $\pm$0.004 |
| B-V | $\mu$ | 1.116 | $\pm$0.006 |
| | $\zeta_{bv}$ | 0.0995 | $\pm$0.005 |

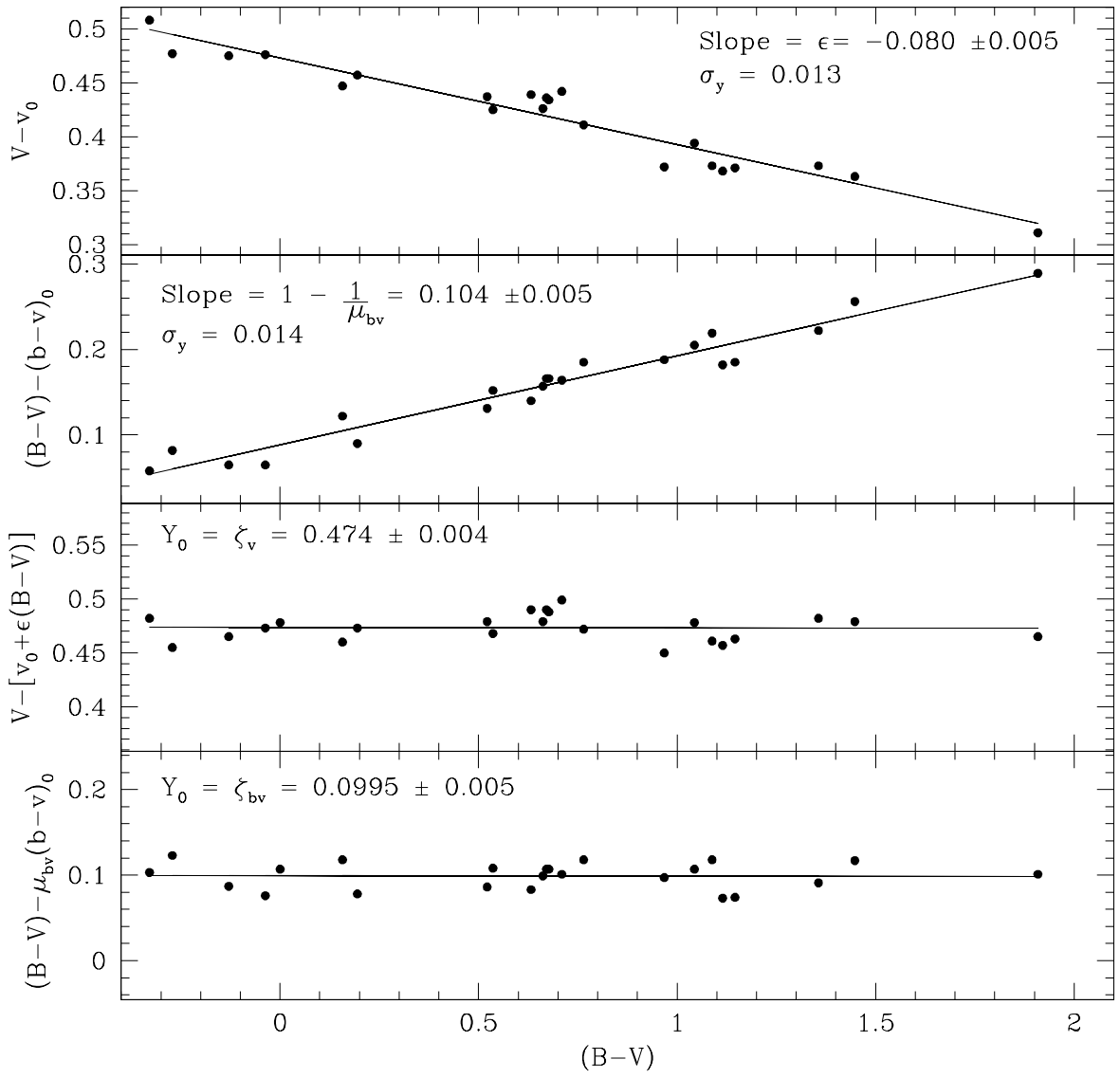


Figure 3.2 Linear fits used to determine the color transformation and offset terms.

internal error for each measurement which is preserved in the final catalog. See Figure 3.3 for a graphic representation of the internal errors of the final CMDs.

The conversion from instrumental magnitude to calibrated magnitude introduces the external errors. Use of time averaged extinction coefficients as well as uncertainty associated

with the aperture correction and the transformation coefficients contribute to the external error. One could perform a formal error analysis, but the comparison of how well the standard stars transform to the standard system shown in Table 3.2 represent a direct measure of the external error. Specifically the standard deviation of the mean difference between the transformed magnitude from the catalog value.

The external errors, shown as the STDDEV row at the bottom of Table 3.2, are both on the order of $10^{-2}$ mag or $\sim 0.1\%$. Rather than risk the perils of combining external and internal errors, in this document, whenever error is cited, it refers to internal error only.

## 3.2 Removal of Non-stellar Sources

We now turn our attention to filtering out non-stellar objects and stars not associated with the GCs from the CMD. Non-stellar objects include, but are not limited to, background galaxies, cosmic rays, and defects on the chip. Furthermore, stars not associated with the cluster, also known as "field stars," pollute the CMD with stellar "noise". However, MW field stars taper off beyond $V > 20$ (Reid & Majewski 1993); galaxies and quasars dominate the CMD background noise at fainter magnitudes.

### 3.2.1 Sharp and $\bar{\chi}$

To address the problem of non-stellar objects, `ALLFRAME` reports two values for each object whose stellar profile converges, SHARP and $\bar{\chi}$. Stetson (1987) describes SHARP (specifically equations 1-4 and Figure 2a), and Stetson & Harris (1988) (see Figure 28) detailed $\bar{\chi}$. Simply put, however, SHARP is a mean shape statistic and $\bar{\chi}$ represents the quality of the fit. Based on an analysis of plots of $\bar{\chi}$ vs. SHARP, Bergbusch & Stetson (2009, see Figure 3 for details) derived the following filtering criteria

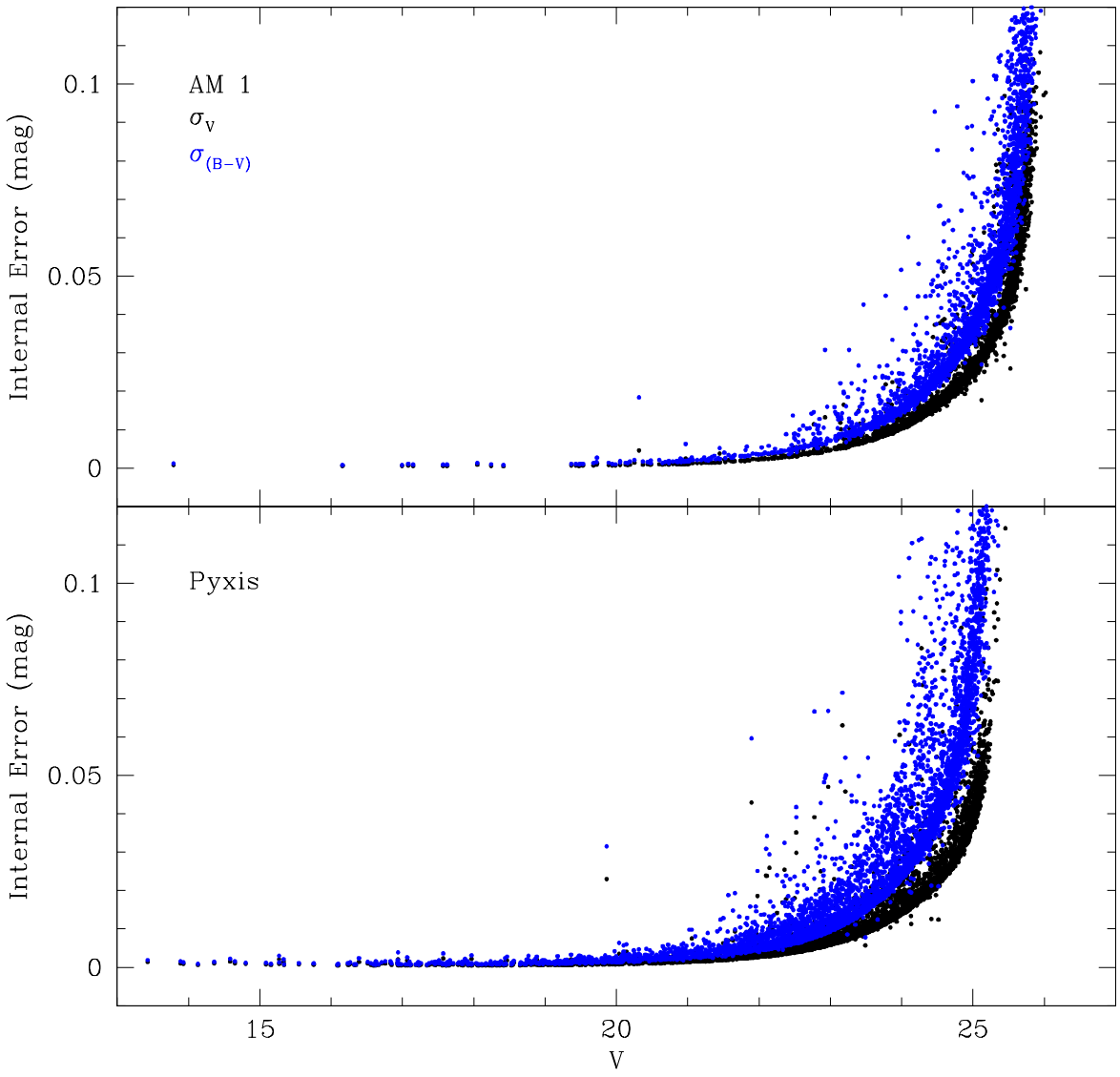


Figure 3.3 Internal errors of the averaged CMDs as a function of $V$ magnitude. Black dots represent the uncertainty in $V$ and blue dots in $(B-V)$.

$$1.0 \geq \mathrm{SHARP} \geq -1.0 \tag{3.11a}$$

$$\bar{\chi} \leq 1.3 + 5.0 \times 10^{-0.2(V-14)}. \tag{3.11b}$$

It is worth noting that the $V$ term in Equation 3.11 refers to the standard magnitude, thus filtering must be performed post calibration. Figure 3.4 shows a direct comparison of the clusters' CMDs filtered in this manner.

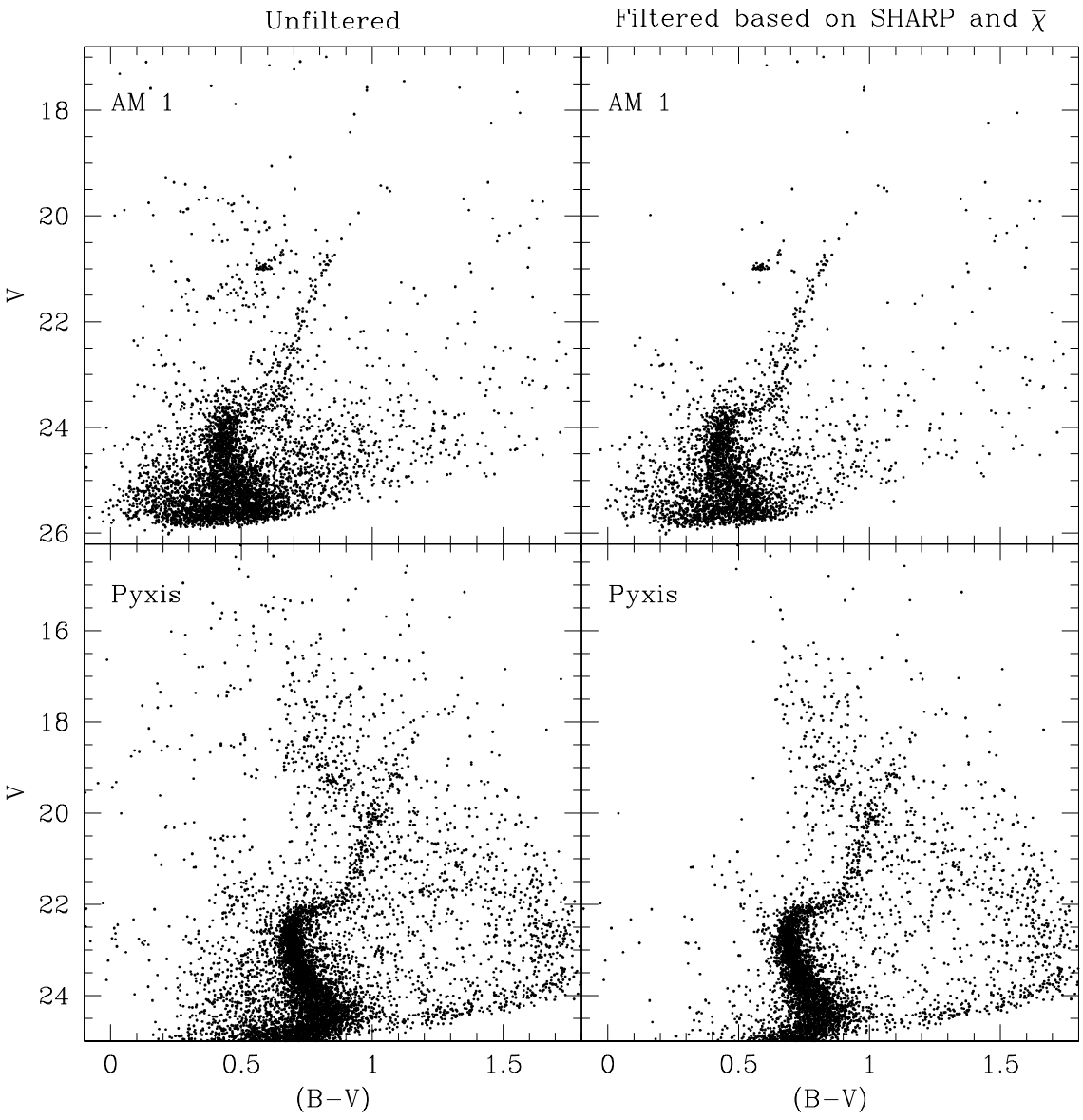


Figure 3.4 Comparison of cluster CMDs with and without the filtering criteria specified in equation 3.11.

### 3.2.2 Statistical Subtraction

Finally there is the problem of field stars infiltrating the color magnitude diagram. To address this, Carney & Seitzer (1993) described a method of determining the CMD of the field stars in a region near the cluster and subtracting away stars from the cluster that match the pattern. This technique is not perfect; it does not eliminate all stellar "noise" from the final CMD and it can even eliminate some actual cluster stars. The design is such that the technique is more efficient at the former than the latter.

To determine the CMD of the field stars, one must obtain data in as close enough to the cluster as to be an accurate representation of the field stars but not so close as to contain cluster stars. This is known as the "control field". In order to avoid adding noise to the CMD in the region of interest, the "program field", the SNR of the control field, and hence the total exposure time on it, must be comparable to the program field. It is common for control fields to be separate images. However, given the enormous amount of total integration time devoted to each cluster, imaging separate control fields of comparable SNR was deemed impracticable. Therefore, I used an aperture around the core of the cluster as the program field, and an outer annulus as the control field.

As is evident in Figure 3.5, the aperture-annulus technique only applies to AM 1. Pyxis' apparent size extends beyond SOI's field of view. The upper panels of Figure 3.5 show that 500 pixels, or $1.28'$, is a comfortable aperture for AM 1 to serve as the program field. It easily encompasses the half-light radius of $0.32'$ and about a third of the tidal radius, $r_t = 3.24'$ (Hilker 2006), but the cluster is centered too close to the left edge of the frame for a full circular annulus. Therefore I chose a semi-annulus with an inner radius of 620 pixels ($1.59'$) and an outer radius computed to give an equal area of the aperture to serve as a control field.

The basic algorithm is that for each star in the control field, search program field for stars within a four sigma window. If one or more stars are found in the program field, choose the

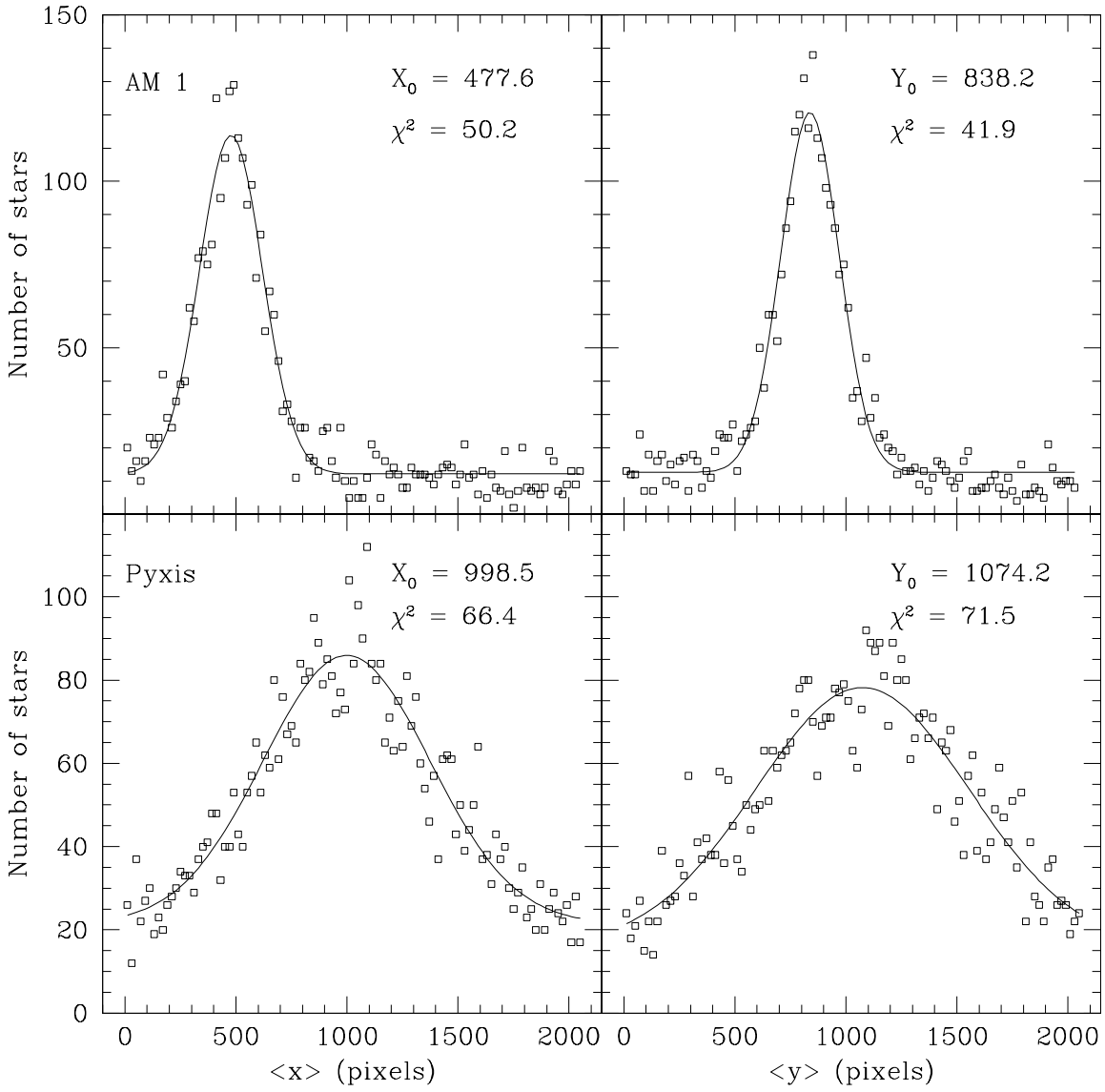


Figure 3.5 Histograms used to determine the center of the clusters in pixel space. Stars were summed in 20 pixel columns and rows to determine the $x$ and $y$ pixel centers respectively. The difference in width of the best fitting gaussian between AM 1 and Pyxis is accounted for by the apparent size of each cluster.

closest in color-magnitude space and subtract both the program and control star away. If no stars are found, preserve the control star in its output catalog. The input program and

control fields as well as the final, subtracted fields are shown in Figure 3.6.

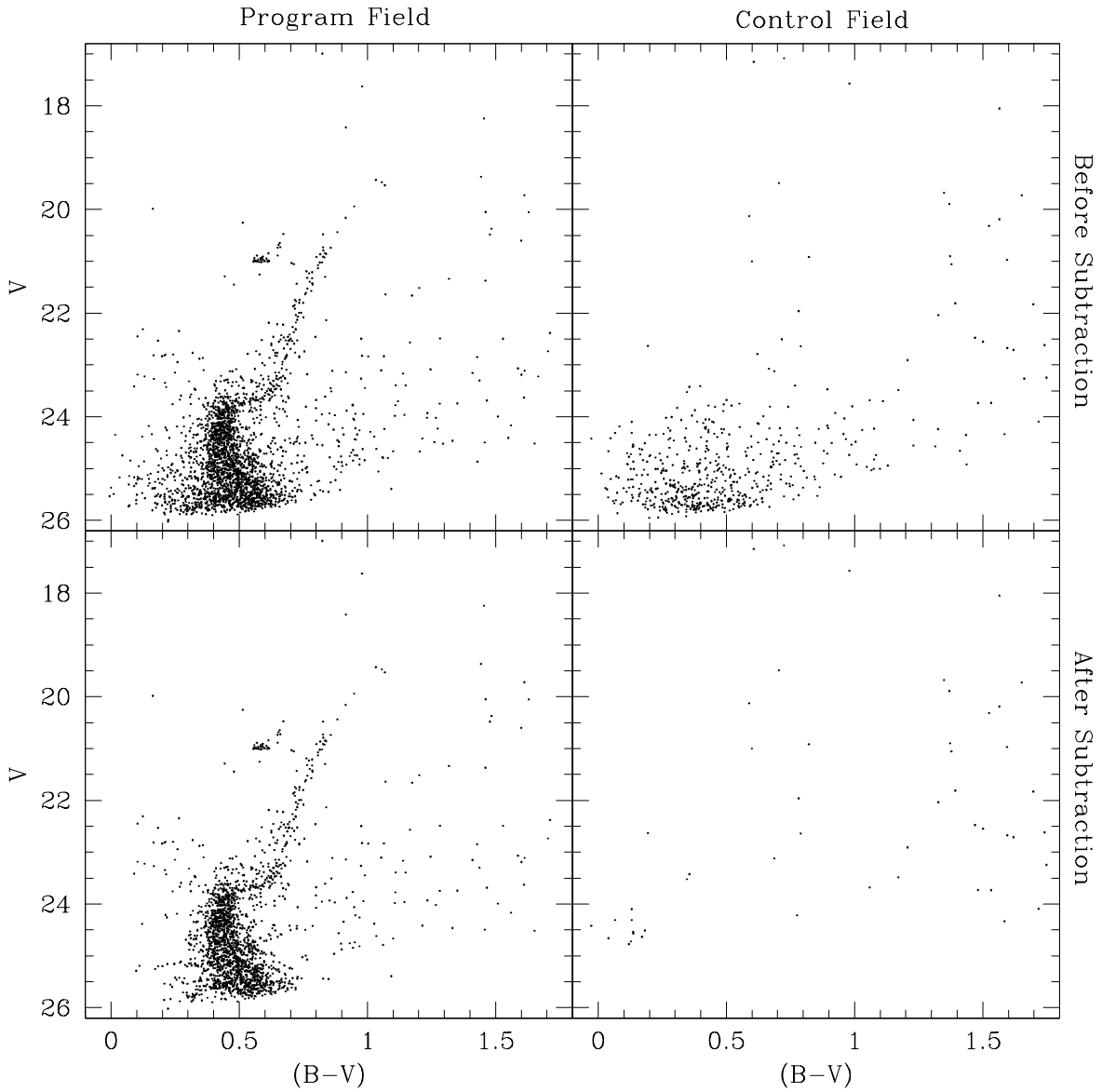


Figure 3.6 Results of the statistical subtraction technique for AM 1.

## 3.3 Automation

Most of the procedures outlined in this chapter require some degree of automation. In this section, words in `typeset` font refer to software I wrote to aid in the process, the source code of which is found in Appendix B.

For the calibration, I wrote a perl script called `daocal` that accepts as input the instrumental magnitude catalogs for the $b$ and $v$, the atmospheric extinction coefficients and the color transformation coefficients and applies Equation 3.7 to produce the final $V$ and $(B-V)$ magnitudes. The program also preserves the SHARP, $\bar{\chi}$, and the variability index, $\lambda$, for each filter. The variability index is a ratio of the standard deviation of the star's magnitude to its internal photometric error. Large $\lambda$ values indicate strong candidates for variability.

The program `statsub` performs the statistical subtraction. Given the aperture and inner radius of the annulus, it selects the program and control field stars, determines the selection window, which is four sigma by default, and executes the statistical subtraction.

## 3.4 The Final CMDs

The final color-magnitude diagrams used in the subsequent analysis are shown in Figure 3.7. Both clusters have been filtered in SHARP and $\bar{\chi}$ according to Equation 3.11. The statistical subtraction technique described in §3.2.2 was applied to AM 1 only. In order to further clean Pyxis, I only included stars within the core radius of $83''$ (Da Costa 1995). This significantly cleans the CMD and sharpens the RGB at the expense of further depleting the HB.

The red error bars were computed by averaging the internal errors the stars within in 0.2 mag width bins in $V$ centered on the mean magnitude of the HB and then integer magnitude values below. The width of each bin is 0.2 mag in $(B-V)$ centered roughly on the intersection of the center of mean $V$ magnitude of that bin and the cluster's predominant sequence in that region (RGB, SGB and MS).

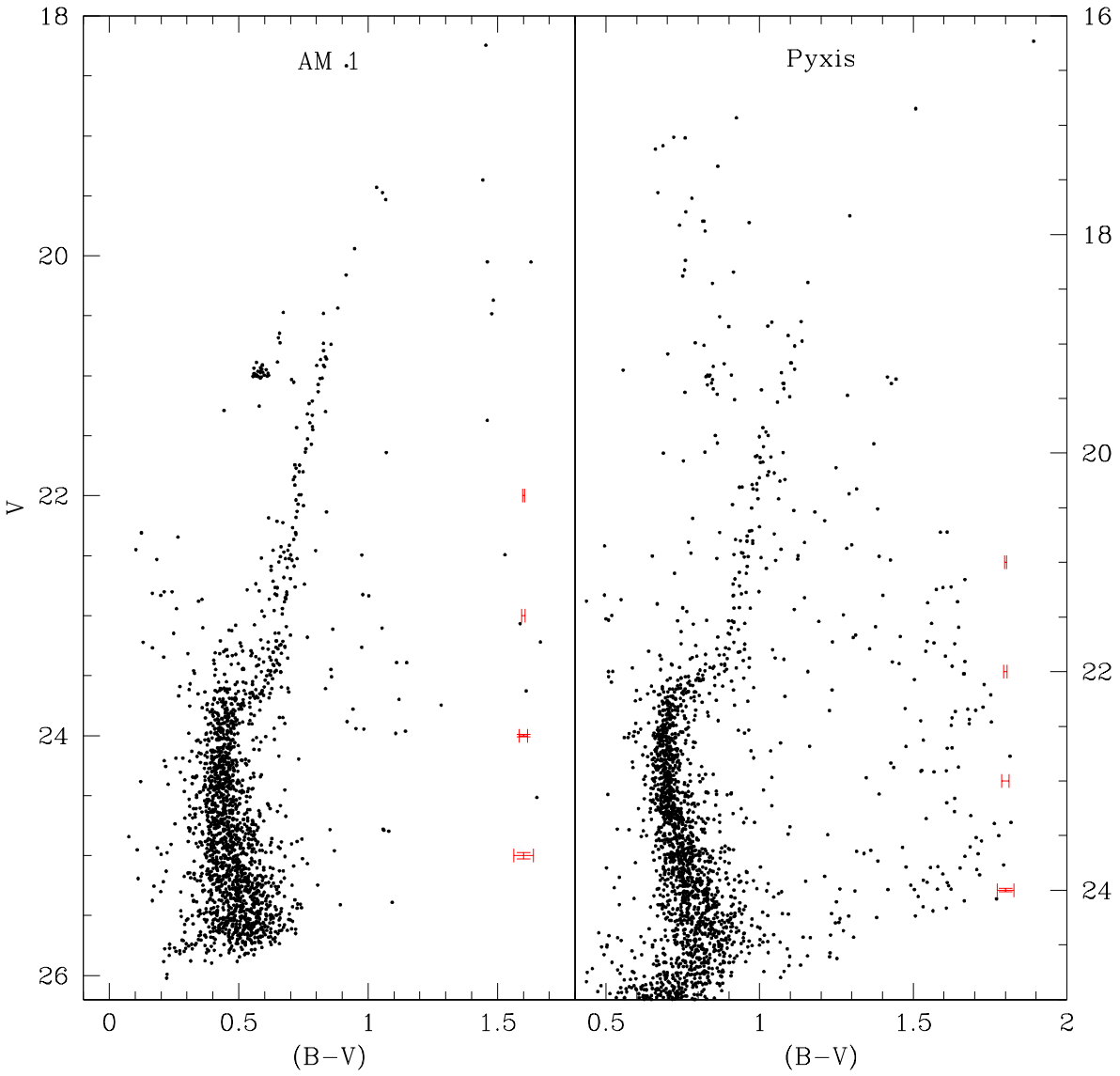


Figure 3.7 The final color-magnitude diagrams for AM 1 and Pyxis. The error bars are only shown when the separation between brackets is visible. Only the $(B-V)$ errors typically meet this criteria, whereas in the $V$ errors become distinguishable at the faintest magnitudes.

# Chapter 4

# Results

The properly calibrated color-magnitude diagrams reveal much of scientific interest about the clusters. In the process of determining the clusters' ages, the principal goal, other factors such as composition and distance reveal themselves. Many techniques rely on theoretical models, specifically isochrones, or loci of constant age in the color-magnitude space, that contain unresolved problems, and one must treat with caution the results they produce.

To reduce the general concerns of over reliance upon continually evolving theoretical models, the age techniques employed in this chapter fall into three broad categories; empirical, semi-empirical and theoretical. Section 4.1 employs a purely empirical approach in that the CMD data are compared directly with data from other clusters. Section 4.2 employs two techniques for establishing relative ages that compare our data with reference cluster data, but utilize theoretical isochrones to establish an age scale. Finally, section 4.3 compares our data directly with theoretical models. Broad agreement among the three approaches should lend credence to the conclusions they provide.

## 4.1 Empirical

Much can be learned about our program clusters by simply comparing their color magnitude diagrams to the mean ridge lines, or fiducial sequences, of other, well-known clusters. Intrinsic factors influence the shape of features in the CMD. For example, heavy element abundances affect the slope and curvature of the RGB and age influences the length of the SGB and its brightness relative to the HB. Extrinsic properties, namely interstellar extinction and distance, affect the overall position of the data in the CMD. Therefore, after correcting for extrinsic factors, a reasonable match between a fiducial sequence and a target cluster

provides, at the very least, a starting point, or first guess, for determining intrinsic factors of the cluster in question. Indeed, overlay of fiducial sequences reveal relative ages directly as exemplified by Sarajedini et al. (2007) and Marín-Franch et al. (2009) just to name two, but such techniques require photometry well below ($V \gtrapprox 3$ mag) the MSTO. Additionally, fiducial sequences are necessary for an determination techniques that does not require such depth in magnitude described by Vandenberg, Bolte, & Stetson (1990, hereafter VBS or simply "the horizontal method") to be discussed later. For the time being, we simply wish to find fiducial sequences that align reasonably well with our data to serve as a reference cluster and provide some starting points for inferring the intrinsic properties of AM 1 and Pyxis.

Stetson & Harris (1988) produced a collection of fiducial sequences spanning a broad range in metallicity that serve as a proof of concept for choosing appropriate comparison clusters. Three of these, M5, M92 and 47 Tuc, were registered to the observational planes of AM 1 and Pyxis, but only M3 (Ferraro et al. 1997) and M5 (Sandquist et al. 1996) provided a sufficient match worth consideration. Figure 36 of Stetson & Harris demonstrates the diversity of fiducial sequences and illustrate why it was not necessary to include them in Figure 4.2.

Ultimately the fiducial sequences of Sandquist et al. (1996) were chosen for analysis based on the depth of the MS, sufficient coverage along the RGB and a distinction in populations between AGB and RBG stars. I also consider the fiducial sequences for M3 of Ferraro et al. (1997) based on Dotter et al. (2008b) use of this cluster, but with his own fiducial constructed from HST data, for a fiducial comparison technique with AM 1 (the "horizontal method" discussed in §4.2.1). Figure 4.1 shows the fiducial sequences of M3 and M5 over-plotting the data from which they were produced. The M3 data are available online via the VizieR service (Ochsenbein, Bauer, & Marcout 2000), and Eric Sandquist (priv. comm.) supplied the M5 data. Both clusters main sequence fiducials were computed by determining the peak

of the color histograms in equal width magnitude bins in order to avoid the redward bias inherent to the mean and median colors due to binary stars (see §4.2.1 for further details).

The complete datasets for both M3 and M5 produced rather cluttered diagrams fraught with foreground stars, galaxies, blended stars and other undesirable artifacts. In order to make Figure 4.1 more presentable, known variable stars were excluded from the M3 data. Eric Sandquist did not include the M5 variable stars in the data he provided. Though the mean magnitude of the RR Lyrae stars fall along the HB fiducial line, they are not presented as mean magnitudes in the data and simply serve to clutter the HB. The diagonal feature bisecting the M3 diagram indicates two different datasets used to produce the diagram. The M5 data included the $\chi$ parameter output by DAOMASTER permitting filtering of the CMD according to the criteria described by Equation 3.11b.

The first step in the procedure of registering the fiducial sequences to the observational plane of the target clusters is to remove the effects of interstellar reddening and extinction via the following formulae;

$$V_0 = V - R_V\, E(B-V) = V - A_V \tag{4.1a}$$

$$(B-V)_0 = (B-V) - E(B-V), \tag{4.1b}$$

where the extinction parameter, $R_V = A_V/E(B-V) = 3.315$ from Schlegel et al. (1998, Table 6, Appendix C), matches the Landoldt standard system to which the data are calibrated, and the selective extinction, $E(B-V)$, is chosen appropriate to each fiducial cluster from the Harris (1996) catalog listed in Table 4.1. Harris' extinctions represent the average of those reported in Webbink (1985), Zinn (1985), and Reed et al. (1988) and have typical uncertainties of 10% but no less than 0.01 mag.

Next the extinction and reddening corresponding to the target clusters, AM 1 and Pyxis, were added to the fiducial sequences by solving equation set 4.1 backwards using extinction

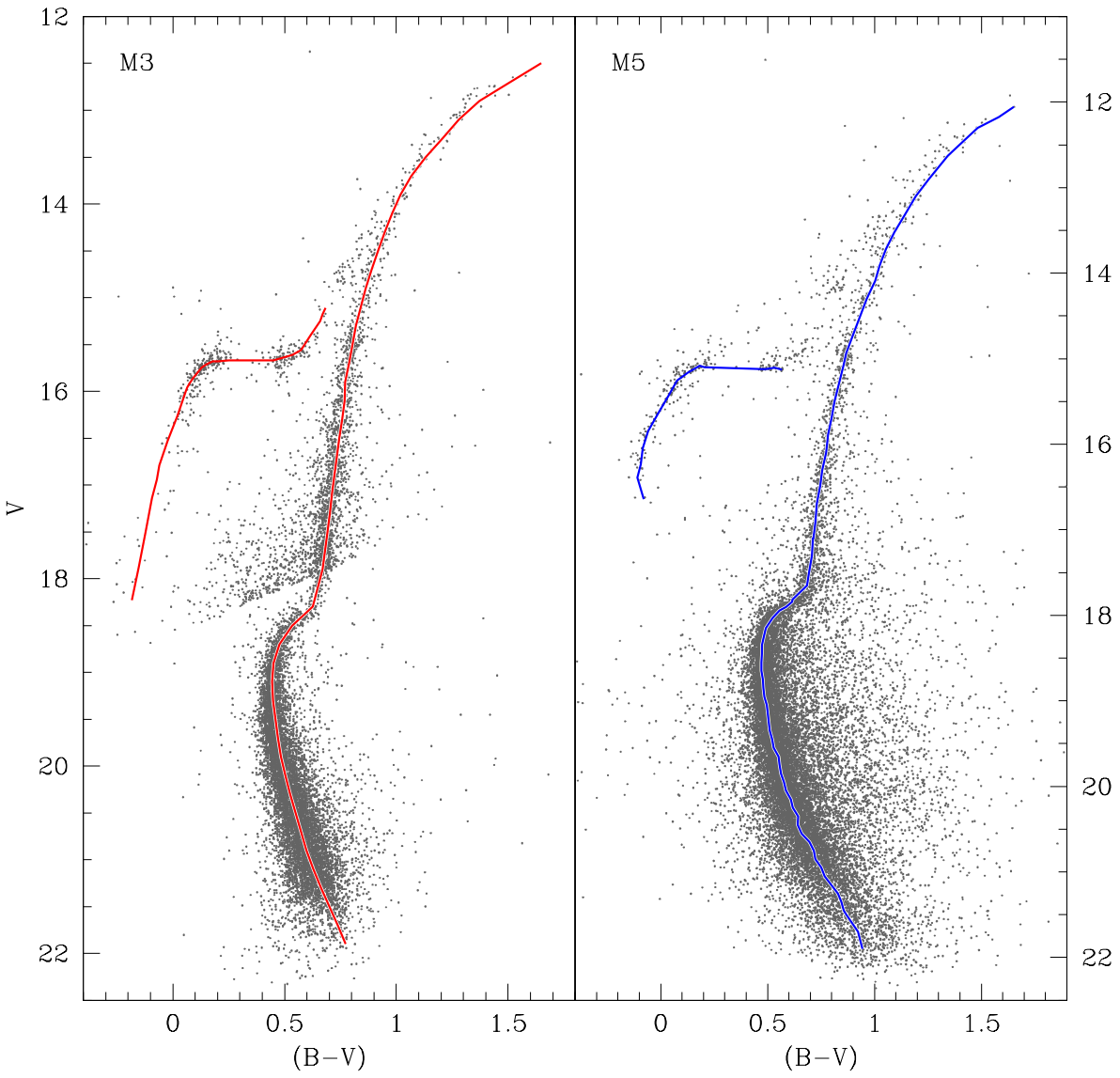


Figure 4.1 Fiducial sequences of M3 (Ferraro et al. 1997) and M5 (Sandquist et al. 1996) over plotting the data from which they were generated. The M3 data were obtained online and the M5 via private communication with the lead author. Known variable stars are excluded from the M3 data, and the M5 data are filtered by $\chi$ according to Equation 3.11b.

values appropriate to each target cluster. In this case, neither of the Harris extinction values for AM 1 and Pyxis provided decent alignment for the fiducial sequences. Lacking

Table 4.1. Data from the Harris (1996) catalog

| Target | [Fe/H] | $E(B-V)$ (Harris) | $E(B-V)$ (Adopted) | $V_{\rm HB}$ | $(m-M)_V$ |
|---|---|---|---|---|---|
| *Reference Clusters* | | | | | |
| NGC 5272 (M3) | -1.50 | 0.01 | ... | 15.64 | 15.07 |
| NGC 5904 (M5) | -1.29 | 0.03 | ... | 15.07 | 14.46 |
| *Target Clusters* | | | | | |
| AM 1 | -1.70 | 0.00 | 0.008[a] | 21.00 | 20.45 |
| Pyxis | -1.20 | 0.21 | 0.25[b] | 19.25 | 18.63 |

[a]Schlegel et al. (1998)

[b]Dotter et al. (2011)

any physical justification for treating extinction as a free parameter, I instead used values adopted by other authors that produced good agreement. For AM 1, the extinction of 0.008 comes from the infrared dust maps of Schlegel et al. (1998), and the value of 0.25 used for Pyxis was obtained by Dotter et al. (2011) from isochrone fits.

Differences in the distances between the clusters are accounted for by equating the mean magnitude of the horizontal branches, $V_{\rm HB}$, of the fiducial sequences to that of the target clusters. RR Lyrae variable stars occupy the portion of the HB within the color domain $0.18 \leq (B-V) \leq 0.42$, also known as the "RR Lyrae gap" due to the apparent lack of HB stars in this region. When sufficient data are collected to determine average magnitudes for the RR Lyres, $\langle V_{\rm RR} \rangle$, the gap fills in and becomes an excellent measure of the mean magnitude of the HB as a whole. As such, $\langle V_{\rm RR} \rangle$ and $V_{\rm HB}$ are effectively interchangeable.

Lee & Carney (1999) measured the intensity-weighted average magnitude of 35 RR Lyraes in M3 to find $\langle V_{\rm RR} \rangle = 15.665 \pm 0.013$. For M5, Arp (1962) measured the magnitude of the RR Lyrae gap to determine $V_{\rm HB} = 15.11$, and Reid (1996) finds $V_{\rm RR} = 15.054 \pm 0.058$ from the average magnitude of 44 RR Lyraes after excluding five of their total sample as outliers.

Lacking RR Lyraes in AM 1 or Pyxis, I determined $V_{\rm HB}$ by averaging the $V$ magnitudes, after filtering outliers by a two sigma rejection algorithm, of the stars within the black rectangles in the HB regions of Figure 4.2. Stars not included in the final average are

indicated by open circles in the inset regions of Figure 4.2.

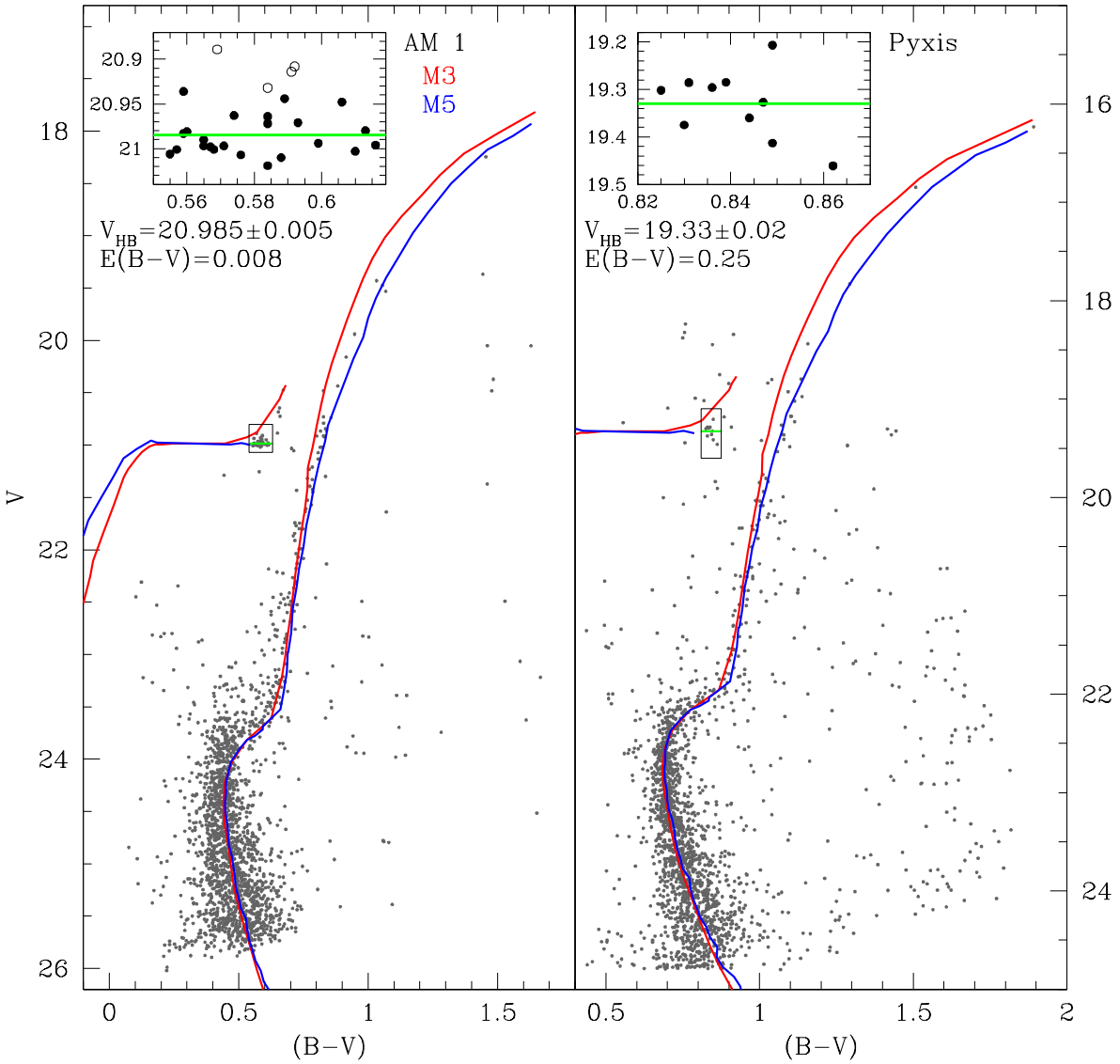


Figure 4.2 Fiducial sequences of M3 and M5, the solid red and blue lines respectively, transformed to the same distance and reddening of the AM 1 and Pyxis. The insets expand the HB for each cluster indicated by the solid black rectangular regions in the main figures. The green line represents the average V magnitude of the stars in the HB region after a two sigma clipping algorithm. The open circles in the insets represent stars omitted by the sigma clipping filter.

Examining Figure 4.2 reveals that both AM 1 and Pyxis are more similar to M5 than M3, indicating that the former serves as a better choice for relative age determination techniques. We are also able to formulate the following hypotheses about the intrinsic properties of the target clusters;

i) the metal content of both clusters are probably closer to M5 than M3 as evidenced by the common shape and slope of the RGBs.

ii) the difference in brightness in the SGB indicates AM 1 is noticeably younger and Pyxis is either slightly younger or the same age as M5.

The more robust techniques discussed in the ensuing sections test these hypotheses.

## 4.2 Semi-Empirical Methods

### 4.2.1 The Horizontal Method

The fiducial sequence of M5 may be used to employ a powerful, relative age determination method described by Vandenberg, Bolte, & Stetson (1990, VBS). The technique exploits the fact that the length of the SGB decreases with age, hence the relative length between the MSTO and the RGB is an age indicator. Registration of two clusters to a common color and magnitude reveals relative age as a function of color difference between their RGBs provided the RGBs are parallel (see Figure 4.5 (c)). Iron and alpha[1] abundance influences the slope and shape of the RGB due to their contribution of electrons to the major opacity source, $H^-$, therefore differences in metallicity between the target and reference clusters within $\Delta$[Fe/H]$\leq$ 0.2 dex maximize the reliability of the technique. As shown in the previous section, particularly in Figure 4.2, the shape of the RGB of M5 matches both AM 1 and

[1]Alpha elements are those whose atomic number is an integer multiple of a helium nucleus. For elements lighter than Iron, they include C, N, O, Ne, Mg, Si, S, Ar, Ca, and Ti. Spectroscopic measurements summarize the [$\alpha$/Fe] ratio as the average of Mg, Ca and Ti abundances.

Pyxis quite well, making it an excellent reference cluster for this technique without any *a priori* knowledge of the metal enrichment of the clusters.

Horizontal registration of the clusters is quite straightforward due to the ease of measuring color of the MSTO by locating the bluest region of the main sequence. However, complication arises in measuring the vertical position, or magnitude, of the MSTO, a feature vertical as seen in data and isochrones. For example, notice the MSTO regions of M3 and M5 shown in Figure 4.1 appear nearly vertical for about a half magnitude. VBS conclude that the point 0.05 magnitudes redward and below the MSTO, indicated by the symbol $V_{+0.05}$, serves as a good registration point due to the consistency of the slope of the main sequence at this relative magnitude.

**Registration Point Determination**

Initially, mean ridge lines for AM 1 and Pyxis were computed by averaging the color of the stars, after eliminating stars beyond $3\sigma$, in ten equal magnitude bins in the ranges $25.5 \geq V \geq 23.75$ and $24.0 \geq V \geq 22.25$ respectively. Figure 4.4 shows the results as orange squares. Stars included in the averages are shown as green dots in Figure 4.4, and red dots signify stars eliminated by the sigma clipping algorithm. The wide and narrow error bars associated with each orange square represent the standard deviation and the standard deviation of the mean respectively.

However, a careful reading of both Ferraro et al. (1997) and Sandquist et al. (1996) reveals that both authors used a modal technique for determining the main sequences of M3 and M5 in order to avoid the effects of double stars and blended stars. Binaries manifest themselves as a parallel main sequence brighter than the single-star main sequence. Imagine, for simplicity, a binary sequence composed solely equal mass pairs; the effect would be a sequence of twice the apparent flux, or $2.5 \log 2 \approx 0.75$ mag brighter, at each color interval. Actual binary pairs have a variety of companion masses blurring the binary sequence (for example see Figure 5

of Davis et al. 2008). A main sequence divided into bins of equal magnitude would show two distributions with the redward comprised of binaries. Clearly an average of the stars in such bins would be driven redward due to the binaries. The remedy is to use the mode, or the peak, of the main distribution.

Employing this technique, I divided the main sequence regions of AM 1 and Pyxis into equal bins of width $\Delta V = 0.2$ mag. Each magnitude bin was subdivided into histogram bins of width of $\Delta(B-V) = 0.04$ and 0.02 mag respectively. Figure 4.3 shows the best fitting gaussians to the color histograms in each magnitude bin. The peak of each gaussian reflects the ridge line point shown as blue squares in Figure 4.4 and listed in Table 4.2. The blue error bars in Figure 4.4 show the FWHM of the fit. To compare the FWHM of the gaussian fits to the internal error, the red error bars in Figure 4.3 are the mean internal error for each magnitude bin scaled according to

$$\mathrm{FWHM} = 2\sqrt{2\ \log 2}\ \sigma \approx 2.355\ \sigma. \tag{4.2}$$

Table 4.2. Mean and modal ridgeline points

| AM 1 | | | | | | | Pyxis | | | | | | |
|---|---|---|---|---|---|---|---|---|---|---|---|---|---|
| | Mean | | | | Mode | | | Mean | | | | Mode | |
| $V$ | $(B-V)$ | $\sigma$ | $\frac{\sigma}{\sqrt{N}}$ | $V$ | $(B-V)$ | FWHM | $V$ | $(B-V)$ | $\sigma$ | $\frac{\sigma}{\sqrt{N}}$ | $V$ | $(B-V)$ | FWHM |
| 23.84 | 0.455 | 0.049 | 0.0055 | 23.7 | 0.482 | 0.178 | 22.34 | 0.716 | 0.043 | 0.0056 | 22.3 | 0.709 | 0.080 |
| 24.01 | 0.438 | 0.047 | 0.0054 | 23.9 | 0.444 | 0.085 | 22.51 | 0.694 | 0.040 | 0.0044 | 22.5 | 0.694 | 0.063 |
| 24.19 | 0.435 | 0.048 | 0.0047 | 24.1 | 0.436 | 0.086 | 22.69 | 0.699 | 0.035 | 0.0040 | 22.7 | 0.694 | 0.076 |
| 24.36 | 0.437 | 0.055 | 0.0050 | 24.3 | 0.446 | 0.102 | 22.86 | 0.698 | 0.038 | 0.0042 | 22.9 | 0.691 | 0.063 |
| 24.54 | 0.440 | 0.064 | 0.0064 | 24.5 | 0.437 | 0.127 | 23.04 | 0.704 | 0.036 | 0.0037 | 23.1 | 0.703 | 0.068 |
| 24.71 | 0.449 | 0.070 | 0.0060 | 24.7 | 0.443 | 0.150 | 23.21 | 0.710 | 0.038 | 0.0036 | 23.3 | 0.717 | 0.089 |
| 24.89 | 0.472 | 0.078 | 0.0064 | 24.9 | 0.466 | 0.175 | 23.39 | 0.739 | 0.051 | 0.0052 | 23.5 | 0.732 | 0.080 |
| 25.06 | 0.469 | 0.071 | 0.0064 | 25.1 | 0.466 | 0.176 | 23.56 | 0.748 | 0.057 | 0.0058 | 23.7 | 0.749 | 0.104 |
| 25.24 | 0.493 | 0.082 | 0.0062 | 25.3 | 0.504 | 0.193 | 23.74 | 0.758 | 0.050 | 0.0043 | 23.9 | 0.764 | 0.127 |
| 25.41 | 0.510 | 0.095 | 0.0075 | 25.5 | 0.514 | 0.227 | 23.91 | 0.786 | 0.070 | 0.0064 | .... | ..... | ..... |

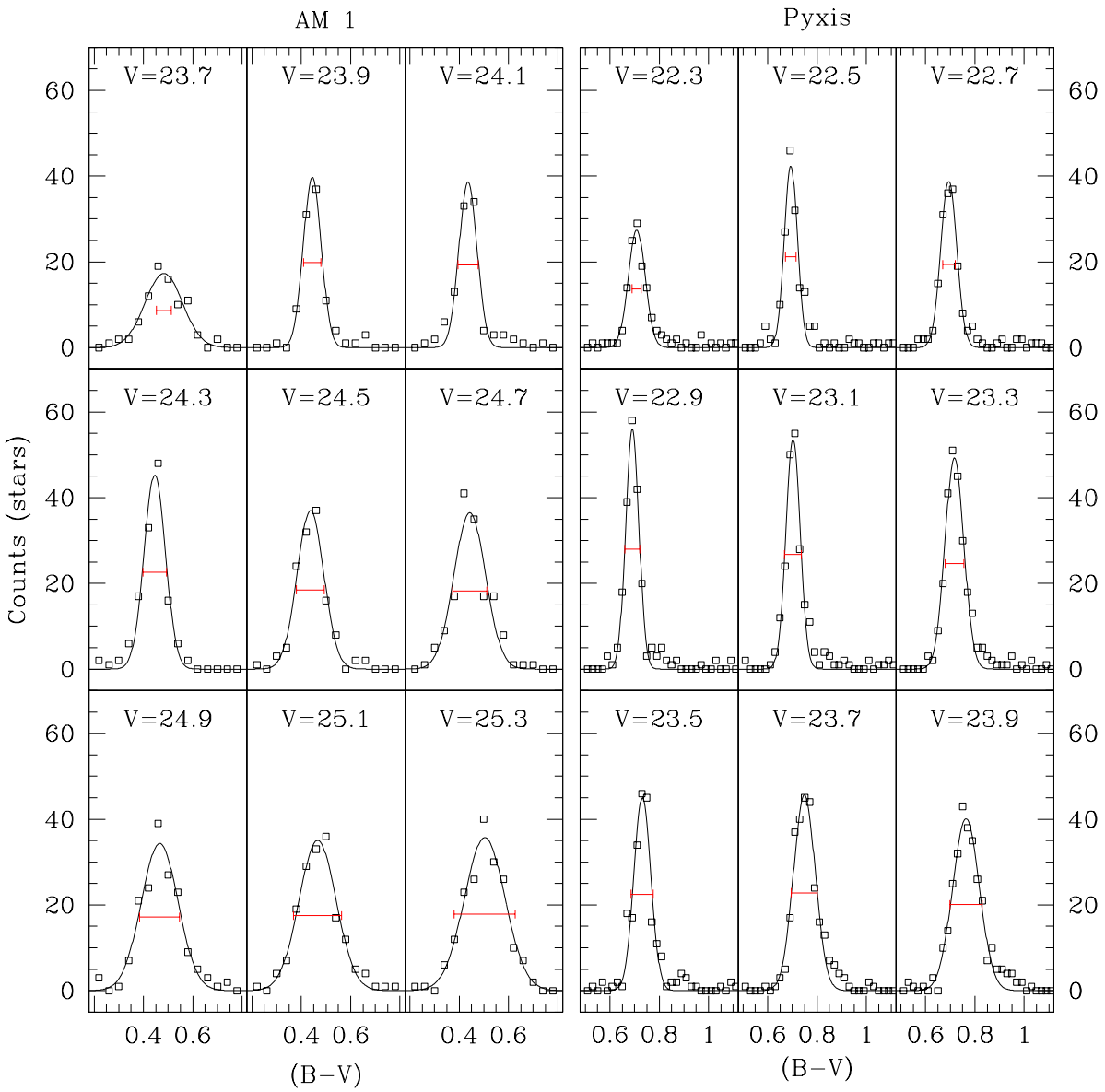


Figure 4.3 Gaussian fits to color histograms in the main sequence region of the clusters. The red error bars represent the average internal error of the stars in each magnitude bin scaled to the FWHM by Equation 4.2 and drawn at the half maximum level. Note the presence of a hump-like structure redward of the main peaks in Pyxis for $V \leq 22.9$, most likely caused by binary stars.

The solid lines in Figure 4.4 show third order polynomials fit to the ridge line points of the

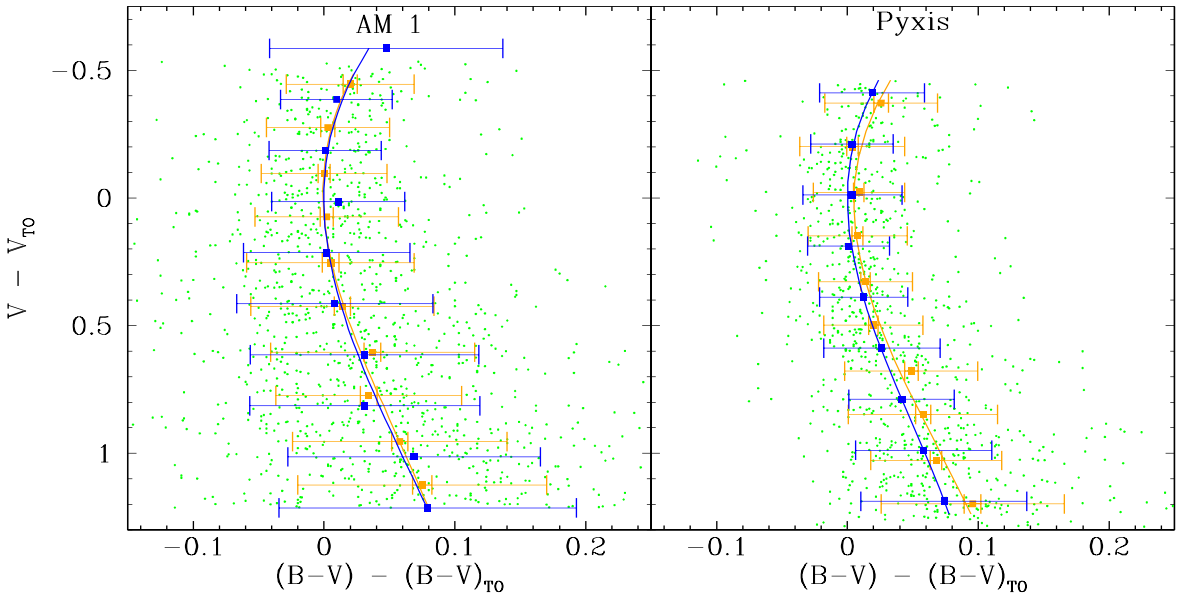


Figure 4.4 Ridgeline fits used to determine the registration points for the VBS horizontal method. Blue squares and error bars represent the mode and FWHM of the best fitting gaussians to the color histogram in each magnitude bin. Orange squares indicate the mean color of the stars with the outer and inner associated error bars reflecting the standard deviation and standard error. Green circles represent stars included in the averaging after the three sigma filtering algorithm. The solid lines show the best fitting, third order polynomial, weighted inversely proportional to the standard deviation or FWHM according to Equation 4.3, to the squares of corresponding color.

clusters using a weighted least-squares algorithm with the weighting inversely proportional to the square of the sigma of each point,

$$w_i = \frac{1}{\sigma_i^2}. \tag{4.3}$$

While AM 1 shows very little difference in the ridge line computed with each technique, Pyxis clearly demonstrates why one should use the modal technique as the ridge line computed with the mean value points is clearly offset to the red. A close look at Figure 4.3 shows a persistent hump feature redward of the main gaussian in panels $V \geq 22.9$. The likeliest explanation for this feature is double stars as both clusters are equally susceptible to the

Table 4.3. Registration points for the VBS method.

| Cluster | $V_{\rm TO}$ | $(B-V)_{\rm TO}$ | $V_{+0.05}$ |
|---|---|---|---|
| AM 1 | 24.29 | 0.435 | 25.19 |
| Pyxis | 22.71 | 0.690 | 23.60 |
| M5 | 18.53 | 0.471 | 19.44 |
| | $18.57 \pm 0.05$[a] | ... | ... |

[a]Sandquist et al. (1996)

software processing effects of blended stars.

For M5, I fit a non-weighted polynomial to the fiducial points supplied by Sandquist et al. (1996) after correcting for reddening and extinction. Minimizing the ridge line polynomial functions reveals the MSTO, and solving for $(B-V) = (B-V)_{\rm TO} + 0.05$ gives $V_{+0.05}$. Table 4.3 lists the MSTO and $V_{+0.05}$ points for the clusters.

### Age Scale Determination

The horizontal method ultimately relies on measuring a color difference between the red giant branches of the reference and target clusters. To do so, one must establish a scale factor to translate color difference into an age. The procedure starts with fitting the fiducial sequence with a model isochrone. For this purpose, and indeed whenever theoretical models are required in this work, I use the Dartmouth Stellar Evolution Database (Dotter et al. 2008a, DSED). The choice of theoretical model code depends on a number of factors to be discussed elsewhere (§4.3), but principle among them at this point is the fact that Dotter et al. (2008b, D08b) employs the VBS method on AM 1 using these same isochrones.

The upper left panel of Figure 4.5 shows the best fitting DSED isochrone for M5 and the requisite parameters. These parameters most closely match those used by VandenBerg, Brogaard, Leaman, & Casagrande (2013, VBLC) that the DSED interface allows. The fit was performed "by eye" and, though they used the Victoria Regina isochrones (VandenBerg, Bergbusch, & Dowler 2006), the VBLC parameters provide the best fit while simultaneously

matching the magnitude of the MSTO without any vertical correction beyond the distance modulus of $(m - M)_V = 14.46$ provided by the Harris (1996) catalog.

The effects of reddening and extinction were removed from the fiducial points via equation set 4.1 prior to comparison with theoretical models. However, a horizontal correction of $\Delta(B - V) = +0.045$ was necessary to align the MSTO colors of the best fitting isochrone with the fiducial sequence of M5. Uncertainties in the color-$T_{\rm eff}$ transformations frequently introduce a color offset in the theoretical models. This color correction may be metallicity-dependent, but the metallicities of M5 and the program clusters are similar enough to preclude any unforeseen consequences. The correction above serves as the implicit horizontal calibration applied to all isochrones DSED throughout this work.

A set of isochrones, generated using the best fitting parameters for M5 with spread of ages intended to reasonably encompass the expected age differences between the fiducial and target clusters, forms the basis for the age scale. In this case, I chose the spread in age to be $\pm$1.5 Gyr of the best fitting isochrone age of 11.5 Gyr. Each isochrone in the set is registered by setting colors of the MSTO set equal to one another and the vertical registration points, $V_{+0.05}$, likewise equated. The lower left panel of Figure 4.5 shows these isochrones registered in this fashion. As one can see, the principal consequence among these registered isochrones is the horizontal position of their RGBs.

Finally, we choose a reference level along the RGBs at which to determine the scale. VBS recommends the point 2.5 magnitudes brighter than $V_{+0.05}$, but the choice is somewhat arbitrary provided that the level is sufficiently bright as not to be confused with SGB stars but still low enough that the RGB remains well populated.

For this work, the VBS-recommended level of $V - V_{+0.05} = -2.5$, indicated by the dashed line in Figure 4.5, suffices. The upper right panel of Figure 4.5 shows a zoom in on this region with the plus marks indicating where the isochrones intersect the scale magnitude level. The isochrones remain parallel and evenly spaced in an interval of $\approx \pm 0.2$ mag. The

slope of the best fitting line to the age vs. color plot, shown in the lower right panel of Figure 4.5 provides the scale factor of -87.85 Gyr/mag.

**Results**

We now employ the horizontal method by registering the fiducial sequence to the target clusters using the age scale and registration points determined above. The procedure is to first align the turnoff color of the M5 fiducial sequence with that of the target cluster, then vertically register the $V_{+0.05}$ points. The results are shown in Figure 4.6 where the solid blue and red lines represent the fiducial sequences of M5 and M3 respectively. The dotted green line marks the point 2.5 mag brighter than $V_{+0.05}$ where the color-age scale is established, and the green plus marks the $V_{+0.05}$ registration point common to both clusters.

I include the M3 sequence in Figure 4.6 to duplicate the work of D08b and to reinforce my earlier conclusion that M5 provides a better match to the shape of the RGB. Though M3 and M5 differ only slightly in the region where the color-age scale is established, the fact that M3 deviates significantly from both M5 and AM 1 brighter than the region of the HB indicates a fundamental mismatch in heavy element composition between the clusters.

Examination of Figure 4.6 leads to two conclusions; that AM 1 is noticeably younger than M5 and Pyxis is indistinguishable in age, both of which support the hypotheses presented by simply matching the HB magnitudes and reddening of the fiducial sequence to the clusters (§ 4.1). These conclusions are softened by the artificial broadening of the RGB by foreground stars and galaxies. Therefore, I can only conclude that Pyxis and M5 are the same age to within $\pm 0.5$ Gyr.

The RGB of AM 1, however, appears noticeably offset from the registered fiducial sequence. The inset panel enhances the region of the RGB near the color-age scale height indicated by the green dashed line. Here the solid blue dots are the individual fiducial sequence points and the solid blue line fits the best second-order polynomial. The dashed blue

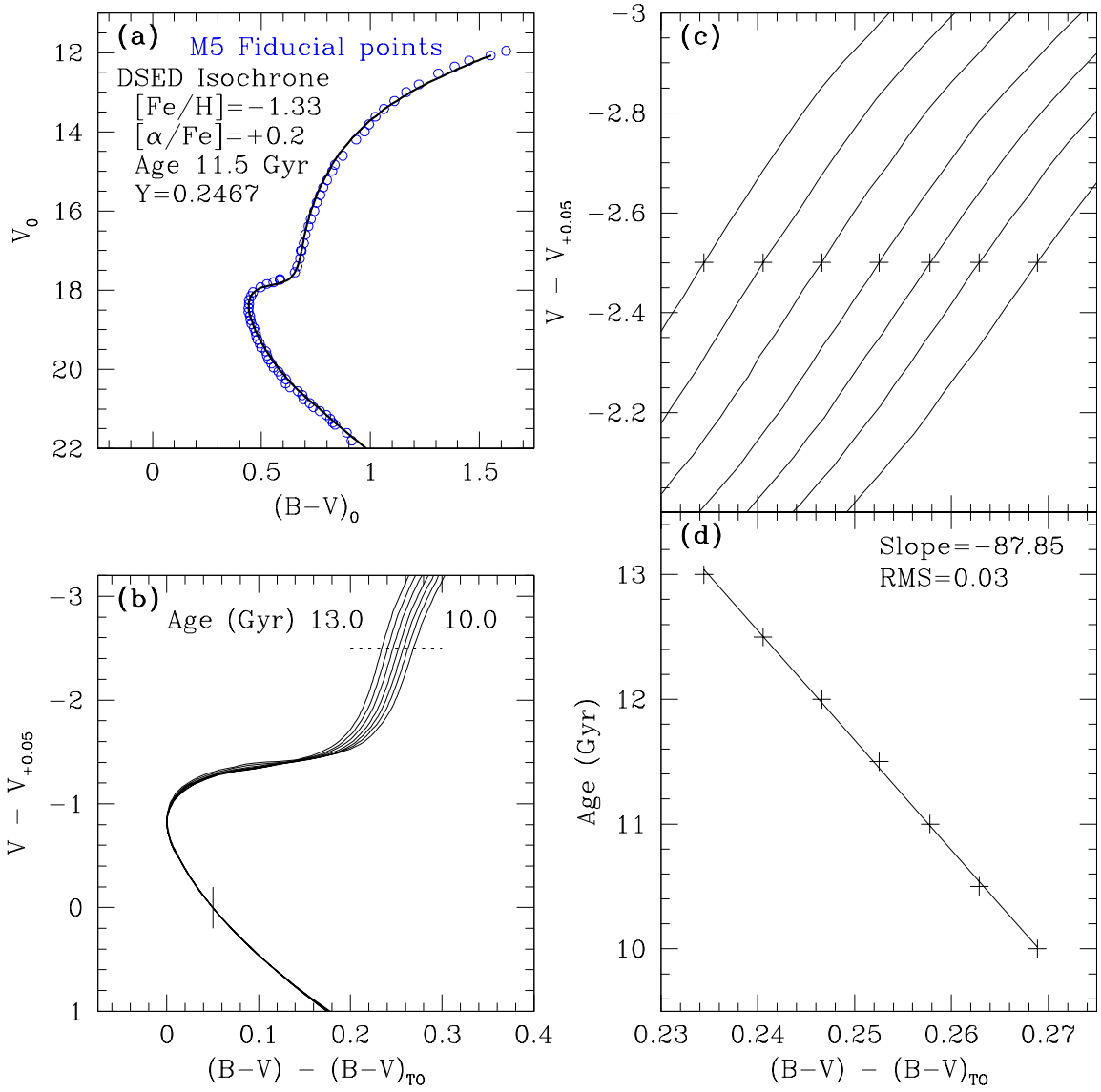


Figure 4.5 **(a)** Best fitting isochrone to the ridge line points of Sandquist et al. (1996). The parameters also best match those used by VandenBerg et al. (2013). **(b)** M5 best fitting isochrones varied by age registered to the common VBS points. The horizontal line at $V - V_{+0.05} = -2.5$ indicates the relative magnitude at which the scale is determined. **(c)** Zoom in on the dotted line region of the lower left panel (b). **(d)** Best fitting line to the points in the panel above gives the color-age scale as **-87.85 Gyr/mag**.

line is the same polynomial shifted in age by $-1.0$ Gyr according to the scale factor established in Figure 4.5. This relative age provides the best match to the data, but again the broadening of the RGB and contamination from non-cluster sources imposes an uncertainty of 0.5 Gyr.

### 4.2.2 The Vertical Method

Many permutations of the vertical method, also known as the $\Delta V$ method, exist, but they all rely on the fact that for a single cluster, the luminosity the zero age horizontal branch (ZAHB) varies slowly with time compared to the rate at which the brightness and color of the MSTO creep fainter and redward as the cluster ages. As HB stars evolve, they grow more luminous as the inert products of helium burning, mostly carbon and oxygen, accumulate in the core. This pushes the helium burning region into an expanding shell making the star brighter but not altering its color. Eventually the star forms a double shell of hydrogen and helium burning regions leading to a rapid blueward evolution until they ascend the asymptotic giant branch (AGB). Therefore, a measure of the difference in magnitude between the MSTO and the ZAHB, commonly denoted as $\Delta V_{\rm TO}^{\rm HB}$, relates to a cluster's age (see, for example, the Appendix of Sandage 1982, particularly Equation A9).

However, several problems arise with this classical implementation of the vertical method. In particular, the difficulty of measuring the vertical position, or brightness, of a feature, the MSTO, that is essentially vertical. Other problems include the fact that the horizontal portion of the HB may be poorly populated, complicating the measurement of mean HB magnitude, $V_{\rm HB}$, and the choice of model isochrones, which are used to derive $V_{\rm TO}$ as a function of age, lead to varied $\Delta V_{\rm TO}^{\rm HB}$ age relations.

To address these problems, VandenBerg, Brogaard, Leaman, & Casagrande (2013, VBLC) conceived a more robust implementation of the vertical method. Their method relies on using the same set of models to simultaneously fit the synthetic, ZAHB and the MSTO, obviating

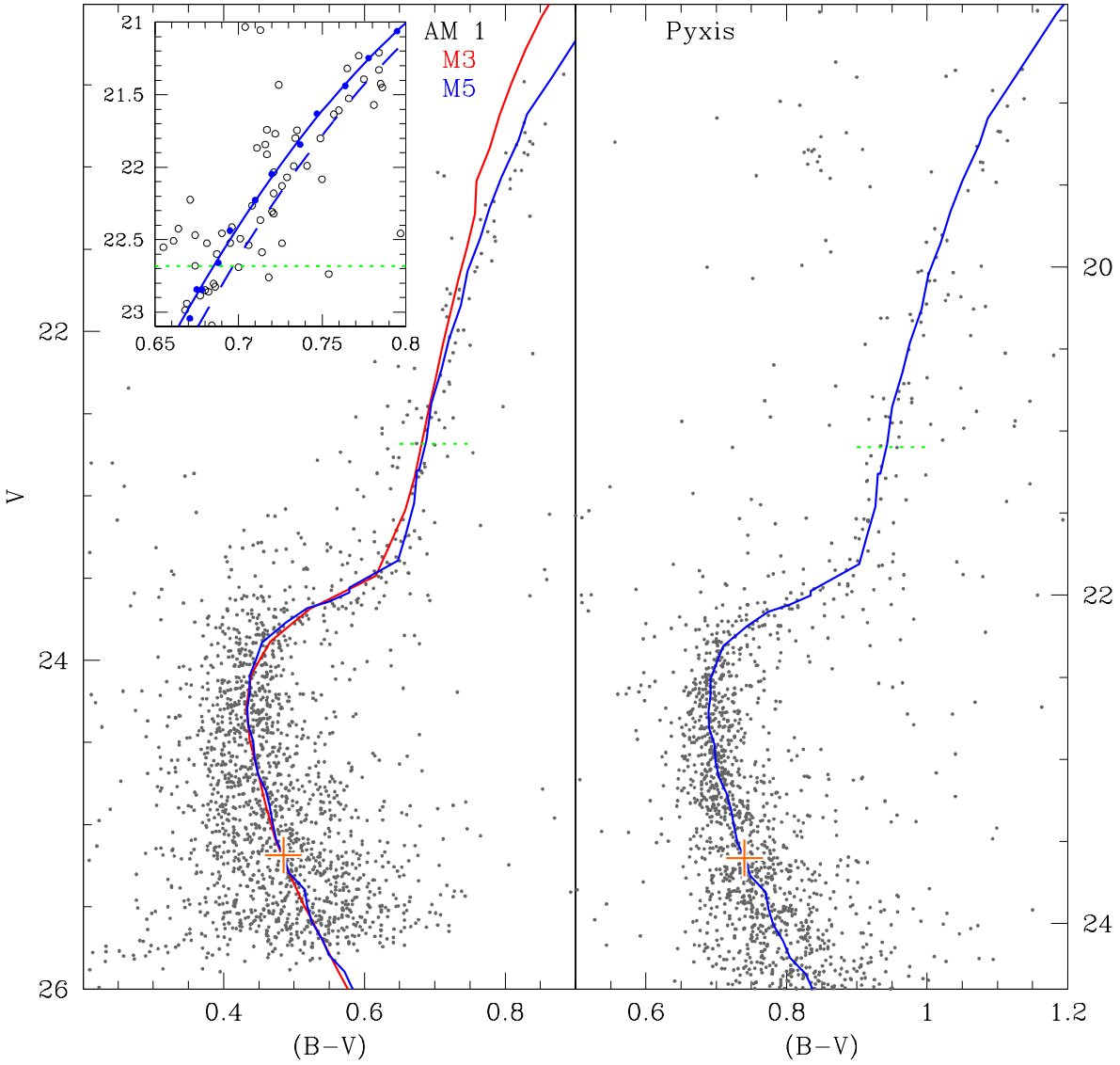


Figure 4.6 The VBS method applied to AM 1 and Pyxis. The blue and red lines are the fiducial sequences for M5 and M3 respectively. The orange cross represents the $V_{+0.05}$ registration point and the green horizontal line represents the $V_{+0.05} - 2.5$ color-age scale level. *Left panel inset:* Zoom in on the RGB of AM 1. The solid blue line represents the best fit, second order polynomial to the M5 fiducial points (solid blue dots). The dashed blue line is the same polynomial shifted by $-1.0$ Gyr according to the scale value derived in Figure 4.5.

the uncertainties imposed on the classic vertical method by the models themselves. The synthetic ZAHB models span the full range possible in color allowing a reliable measurement of $V_{\rm HB}$ for clusters whose HBs are purely redward or blueward of the horizontal part of the HB. Finally, the vertical determination of the MSTO is addressed by fitting the isochrones to the region bound within $(B-V)_{\rm TO}+0.05$ both above and below the MSTO encapsulating the lower sub giant branch and upper main sequence. This region is shown as the red dotted rectangle in Figure 4.7, the redward edge of which is bound by the same position as the $V_{+0.05}$ registration point used in the horizontal method discussed in §4.2.1 plus its counterpart on the SGB at the same color (see Figure 7 of VBLC as an example of isochrones fit to this region of M5).

The method works by first establishing the theoretical model input parameters for the ZAHB, or synthetic HB in the case of the DSED, and isochrones. Then the synthetic HB is fit to the data with an emphasis on matching the faintest edge of the HB due to the fact that core helium burning stars grow brighter as they age, hence the faintest stars most closely represent the ZAHB. Finally isochrones of the same input parameters, but varied in age, are registered to the same color as the cluster's observed MSTO, $(B-V)_{\rm TO}$. The isochrone that best fits the data in the region mentioned above, with an emphasis on the sub giant branch stars, represents the age of the cluster.

However, this method suffers from the same perils of absolute age determination as every other method that relies on isochrones. Thus the method must be applied in a relative sense, with the age of a reference cluster similarly established. M5 serves as a suitable reference cluster just as it does for the horizontal method of §4.2.1. However, the poor definition of the HB of Pyxis exacerbates the application of this method to the point of impracticality.

Figure 4.7 shows the results of the VBLC method applied to AM 1 and the reference cluster M5. The insets enhance the HB, and the dashed green lines therein represent $\langle V_{\rm HB}\rangle$. The green squares are the fiducial points derived in §4.2.1 (see Figure 4.3 and Table 4.2) for

AM 1 and by Sandquist et al. (1996) for M5 who includes ridge line points for the SGB, RGB and HB. Input parameters for AM 1 and M5 are established in §4.3.3 (see Table 4.5 and Figure 4.9) and §4.2.1 (upper left panel of Figure 4.5) respectively. The parameters for M5 agree as closely as the inputs will allow with those used by VBLC (see §3.2 and Figure 7), despite the fact that VBLC uses the Victoria Regina models (VandenBerg et al. 2006). The cyan lines in Figure 4.7 represent isochrones that best fit the SGB region whereas the blue lines best fit the MSTO region. In both cases, the relative age between AM 1 and M5 is $-1.5$ Gyr, generally consistent with both the horizontal method and the fiducial registration method. The poor match between the isochrones and the RGB, particularly with M5, are not a concern as the method relies on the best match to the data in the region bound by the $V_{+0.05}$ registration point indicated by the red, dotted line rectangles in the figure.

## 4.3 Theoretical

I chose the model isochrones of the Dartmouth Stellar Evolution Database (Dotter et al. 2008a, DSED) for comparison with the clusters. The DSED offers state-of-the art physics, a broad range of metallicities and $\alpha$ enhancements, flexibility with helium mass fraction ($Y$) and a handy web based interface. However, the principle reason for the choice of models is the fact that Aaron Dotter himself looked at both AM 1 (D08b) and Pyxis (Dotter et al. 2011, D11b) using HST in the $VI$ system and fit DSED isochrones to both (see Table 4.5 for a summary of results from both studies).

### 4.3.1 Input Parameters

The DSED isochrone software accepts as input age, metallicity ([Fe/H]), helium mass fraction ($Y$), and alpha elemental abundance ([$\alpha$/Fe]). Figure 4.8 shows how adjusting the various parameters affects the shape of the isochrones. The blue lines in each panel represent the best fitting isochrone values from AM 1 by D08b. These do not agree with the

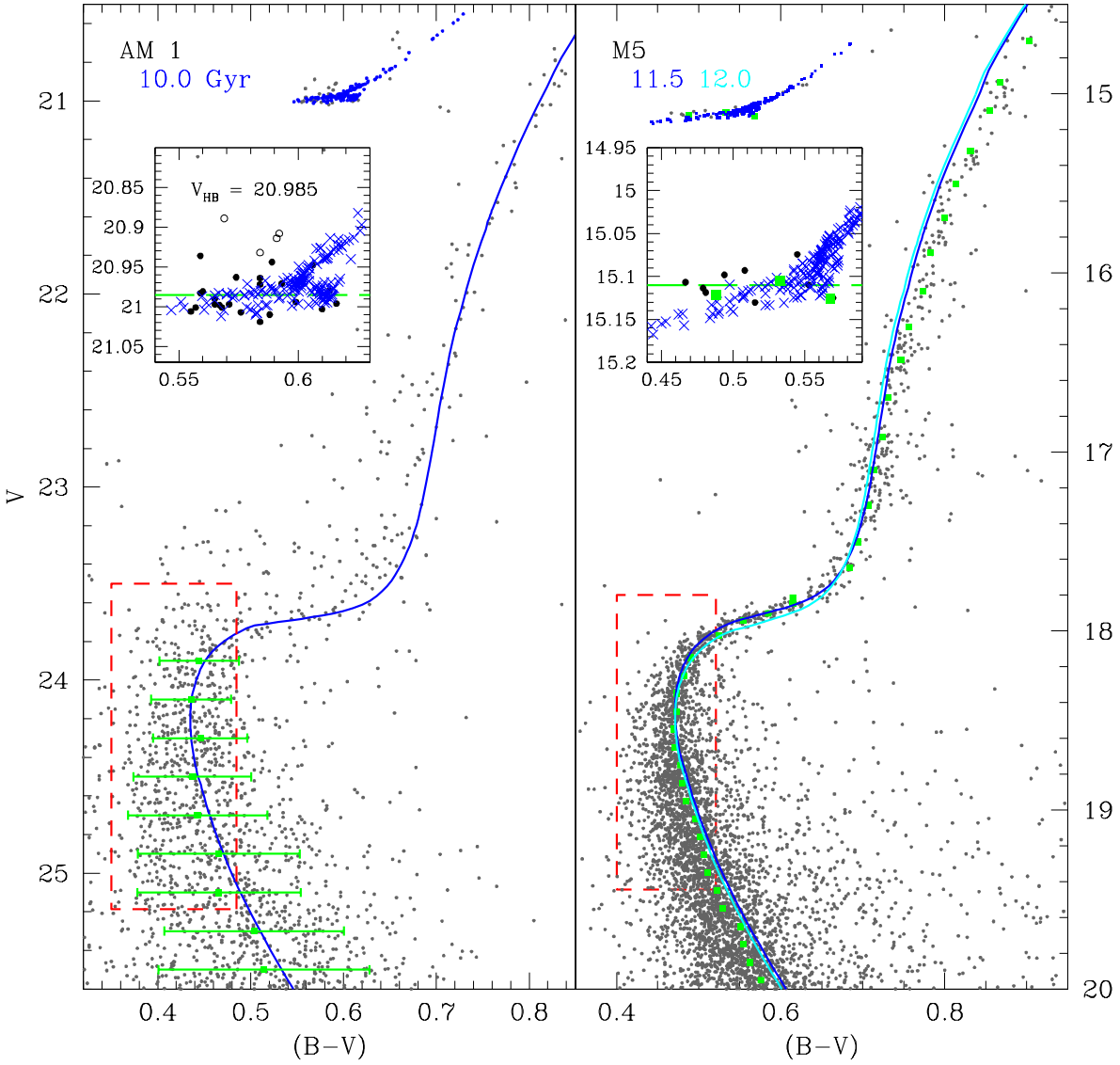


Figure 4.7 The vertical method of VBLC applied to AM 1. Cyan lines represent the ages that best fit the SGB region within the red dotted region and blue lines best fit the MSTO.

final parameters I used for AM 1, but serve rather as a staring point. Before proceeding, let us consider the physics behind each parameter's affect on the model isochrone.

**Age**

Of all the parameters, age is, perhaps, the simplest to describe. Main sequence stars of mass between 0.5 and 2.0 $M_{\odot}$, though the most massive stars that remain in a globular cluster are only $< M_{\odot}$, obey a mass luminosity relationship given by (Clayton 1968, Equation 1-50)

$$L \propto M^{\nu} \tag{4.4}$$

where $\nu$ is in the range of 3.5 to 4.0. Thus the main sequence in the CMD is really a mass sequence; higher mass stars are more luminous and consume their fuel more rapidly. Therefore, as the cluster ages, the MSTO descends the main sequence moving fainter and redward.

The elbow between the subgiant branch and RGB is governed by the size at which the outer envelope of the star is fully convective and cannot cool further (Hayashi & Hoshi 1961, the "Hayashi Track"). This feature remains nearly uniform in color as the cluster ages, and the luminosity of the SGB decreases because the stars at the TO become fainter as the cluster ages. The net effect, as shown in panel (c) of Figure 4.8 is an apparent contraction and dimming of the subgiant branch as the RGB and MS remain coincident.

**Helium**

The effect of helium is to increase the temperature and luminosity of a main sequence star according to the following basic argument. All other properties being equal, specifically metallicity, helium mass fraction, $Y$, dominates the mean molecular weight, $\mu$, of the star as shown in Equation 22 of Carney & Harris (2001)

$$\mu \approx \frac{4}{8 - 5\,Y}. \tag{4.5}$$

Once can think of main sequence stars as being in equilibrium between gravitational contraction and the outward pressure of the gas. Rewriting the equation of state of an ideal gas in terms of mean molecular weight,

$$P = \frac{\rho\, k\, T}{\mu\, m_{\rm H}} \tag{4.6}$$

where $\rho$ is the mean stellar density and $m_{\rm H}$ is the mass of hydrogen, it is apparent that pressure is directly proportional to temperature and inversely proportional to $\mu$. For the star to remain in hydrostatic equilibrium, the pressure in the core must offset the fixed gravitational weight of the envelope. Therefore, in order for pressure to remain constant as helium, and hence the $\mu$, increase, both the temperature and density must also increase.

Nuclear reaction rates in MSTO stars undergoing the proton-proton chain reaction burning hydrogen into helium are proportional to $\rho^2 T^4$. Greater reaction rates increases the luminosity, which means faster fuel consumption. Thus the helium enriched stars at the MSTO have lower mass and luminosity. The junction of the SGB and the RGB depends on the thickness of the convective envelope and hence mass. The total effect of helium enrichment in the observational plane, as shown in panel (d) of Figure 4.8, is a shift of the MS and RGB to hotter surface temperatures and higher luminosities, a lowering of the MSTO and a steepening of the SGB.

**Metallicity**

To understand the effects of metallicity on the main sequence, we must first derive an appropriate model of main sequence stars. Fortunately, Eddington (1926) supplied the classic and useful standard model that bears his name. The derivation starts with a polytropic approach to the solution to the equations of stellar structure in which pressure is a function of density. This approach invokes a relatively simple model relationship between pressure and density. A comprehensive description requires the simultaneous solution of the differential

equations of stellar structure.

For the Sun and other low mass stars, which are all that remain on the main sequence in GCs, the appropriate polytrope, of index 3, is given by Equation 2-290 of Clayton (1968)

$$P = K\,\rho^{\frac{4}{3}} \tag{4.7}$$

Couple this with Kramer's opacity law, an approximation appropriate for low mass stars given by

$$\kappa = \kappa_0\,\rho\,T^{-3.5}, \tag{4.8}$$

and the equations of stellar structure may be reduced to the form given by Equation 6-20 of Clayton (1968)

$$L_{\rm MS} \propto \mu^{7.5}\,M^{5.5}/\kappa_0. \tag{4.9}$$

The constant term from Kramer's opacity, $\kappa_0$, in Equation 4.9 above is directly proportional, though weakly, to heavy element mass fraction, $Z$ (Clayton 1968, §6-6). Therefore, an obvious effect of increasing metallicity of a star is lowering its luminosity. The lower luminosity means greater stellar lifetime due to slower fuel consumption rates. Thus stars on at the turnoff in metal rich clusters tend to have higher masses due to longer stellar lifetimes. However, despite the high power on the mass term in Equation 4.9, the mass difference is small enough that the opacity term dominates leading to a lower turnoff luminosity with increased $Z$.

But the energy of the star must still ultimately escape the core. The increased opacity forces the star has to swell up, putting the energy into gravitational potential of the outer envelope that otherwise would radiate away as light. This increased size cools the outer atmosphere leading to a lower $T_{eff}$. The combined effect in the observational plane is that

all stars appear redder and fainter with increased metallicity, as shown in panel (a) of Figure 4.8.

Metallicity affects the RGB through line blanketing. Heavy element lines predominantly occupy the blue portion of the spectra, thus increased metallicity means smaller net flux in blue bandpasses. The effect on the $(B-V)$ index of reduced $B$ flux is a steeper RGB. In this way, the slope of the RGB at the level of the HB is a common indirect measurement of metallicity. Furthermore, the heavy elements serve as electron donors, increasing the production of $H^-$, the principle continuum opacity source. This causes the entire RGB to shift toward cooler effective temperatures.

**Alpha Element Enrichment**

As stars ascend the RGB, they become more luminous and cooler as indicated by the general shape of the RGB in the observational plane. The principle continuum opacity source is $H^-$ which requires excess electrons in the stellar atmosphere. Several $\alpha$ elements, specifically Mg, Ca, Ti and Cr, have lower ionization potentials than iron and, therefore, serve as electron donors at cooler temperatures. Despite its very high abundance, oxygen has little effect because its ionization potential, 13.6 eV, is very high. The effect of increased $\alpha$ enhancement, shown in panel (b) of Figure 4.8, is increased opacity at cooler temperatures resulting in a flatter RGB at higher luminosities.

### 4.3.2 Input Parameter Constraints

Examination of Figure 4.8 shows how, when coupled with the extrinsic parameters of distance and reddening that are applied as additive offsets to magnitude and color, certain combinations of input parameters produce redundant fits to the data. Therefore, where possible, independent measurements of the physical properties these parameters represent must constrain the inputs.

**Metallicity**

The faintness of the brightest RGB stars in both clusters limit spectroscopic studies to measuring the relative strength of the H + K calcium II lines at 3968.5Å and 3933.7Å respectively, the same technique and metallicity scale employed by Zinn & West (1984, ZW) hence the subscript "ZW". This was calibrated, however, using high-dispersion, high SNR spectroscopic analysis of many globular clusters. Another commonly used metallicity scale is that of Carretta & Gratton (1997) distinguished with a "CG" subscript. They used different high-dispersion spectra than ZW to calibrate their results. Differences of $\sim 0.2$ dex were seen between CG and ZW at intermediate metallicities but not at the highest or lowest [Fe/H]. Marín-Franch et al. (2009) lists all all MW globular clusters in both metallicity scales and provides transformation equations between the two. Suntzeff, Olszewski, & Stetson (1985) measured $[\mathrm{Fe/H}]_{\mathrm{ZW}} = -1.7 \pm 0.2$ for AM 1 based on the brightest two RGB stars, and Palma, Kunkel, & Majewski (2000) obtain $[\mathrm{Fe/H}]_{\mathrm{ZW}} = -1.4 \pm 0.1$ for Pyxis based on multiple spectra of the brightest star in the cluster.

Both spectroscopic measurements tend to the metal-rich end of the uncertainty range compared to photometric techniques. For instance, Sarajedini & Geisler (1996) find Pyxis to have $[\mathrm{Fe/H}] = -1.20 \pm 0.15$ using the simultaneous reddening and metallicity technique (SRM. Sarajedini 1994), and the best fitting isochrones for AM 1 by D08b use $[\mathrm{Fe/H}] = -1.5$.

Recall, however, the ridge line overlay technique discussed in §4.1. As shown in Figure 4.2, due to the steeper slope of the RGB, both AM 1 and Pyxis are more metal rich than M3, and the departure of the RGB of M3 at brighter magnitudes hints at a greater $\alpha$ enrichment or a higher [Fe/H] in both target clusters. Though this is not a precise measurement, the close match with the slope and curvature of M5 indicates both target clusters are of similar metallicity and $[\alpha/\mathrm{Fe}]$. Using the ZW84 scale to be consistent with the spectroscopic measurements mentioned above, M3 and M5 have $[\mathrm{Fe/H}]_{\mathrm{ZW}} = -1.66$ and $-1.38$ respectively (Marín-Franch et al. 2009, and references therein).

### $\alpha$ Enhancement

Undertaking a comprehensive review of the measurements available at the time, Carney (1996, Table 3 in particular) showed that halo GCs share [$\alpha$/Fe] at or very near +0.3. The most recent spectroscopic studies of the extreme outer halo, particularly the "typical" halo clusters Pal 3, Pal 4 and Pal 15, support Carney's characterization (see Table 1.1). Unfortunately, the DSED does not include inputs at exactly this value, instead bracketing it by +0.1 on either side. The effect of [$\alpha$/Fe] on the isochrone is to increase the slope and curvature of the RGB, particularly steepening the upper RGB and leaving the lower portion near the intersection of the SGB unaffected because of the $H^-$ effect noted earlier.

The choice of [$\alpha$/Fe] = +0.4 for both clusters, while providing the best looking fit to the data, relies on the brightest stars along the RGB track of the isochrone to be actual members of the cluster. A kinematic study of the brightest two giants in AM 1 by Suntzeff et al. (1985, see Table III) shows that these stars' radial velocities are consistent with each other as well as the radial velocity of the cluster as a whole providing some support to their inclusion as members of the cluster. Similarly, Palma et al. (2000, see Table 1) shows uniformity among the radial velocities of the brightest six stars in Pyxis. The results from both studies are listed in Table 4.4. The former study's inclusion of only two stars, shown as red plus signs in the left panel of Figure 4.9, as well as greater spread in radial velocity than the latter, lends some caution to the brightest star being a member of AM 1. The magnitudes and colors for Pyxis in Table 4.4 ultimately come from Sarajedini & Geisler (1996), but they observed in the $BR$ filter system preventing a direct identification of these stars in my CMD that uses the $BV$ system. However, Palma et al. (2000) encounters the same problem and invokes color-color transformations to list $V \approx 17.77$ for the brightest star in their survey which they label Pyxis A. Lacking a $(B-V)$ color, I chose the color for the star closest in magnitude among my data for the position of the red plus in the right panel of Figure 4.9. Palma et al. (2000) does not supply the $V$ transformation for the remainder of the stars in his survey nor

Table 4.4. Radial Velocities of the Brightest Red Giants

| AM 1 (Suntzeff et al. 1985) | | | | Pyxis (Palma et al. 2000) | | | |
|---|---|---|---|---|---|---|---|
| Star ID[a] | $V$ | $(B-V)$ | $v_{\rm helio}$ (km/s) | Star ID[a] | $R$ | $(B-R)$ | $v_{\rm helio}$ (km/s) |
| 45 | 18.21 | 1.46 | 102 | A | 17.08 | 2.01 | 32.7 |
| 36 | 19.38 | 0.97 | 130 | B | 17.75 | 1.80 | 38.4 |
| | | | | C | 18.28 | 1.78 | 36.6 |
| | | | | D | 18.33 | 1.75 | 26.1 |
| | | | | E | 18.08 | 1.78 | 37.9 |
| | | | | F | 18.09 | 1.71 | 33.9 |

Note. — The uncertainties associated with the radial velocities for AM 1 and Pyxis are ±9 and ±4.6 km/s respectively.

[a]Star identification assigned by the respective authors.

cite the source of the color-color transformations, but they are all fainter in $R$ than Pyxis A. Thus I lack strong support to conclude that the brightest two stars along the isochrone track are cluster members, but their membership is, at least, plausible.

### Distance

Distance modulus relates the difference between the apparent, $m$, absolute magnitude, $M$, of stars to their distance, $D$, in parsecs via

$$\mathrm{DM_{HB}} = (m-M)_{\rm HB} = (V_{\rm HB} - M_{V(RR)}) = 5\log D - 5. \tag{4.10}$$

The mean level of the horizontal branch, determined in §4.1 (see Figure 4.2), serves as the apparent magnitude, and the absolute magnitude of the HB is based on the compilation by Cacciari & Clementini (2003, CC03, Equation 6.1[2])

$$M_{V(RR)} = (0.23 \pm 0.04)[\mathrm{Fe/H}] + (0.93 \pm 0.05) \tag{4.11}$$

[2]This equation is actually a reprint from Chaboyer (1999, Equation 6) who cites the uncertainty on the offset term as ±0.12. By applying a weighted mean of all the available techniques, Cacciari & Clementini reduce the uncertainty to the value listed in Equation 4.11.

where $M_{V(RR)}$ refers to the mean magnitude of the RR Lyrae variable stars in the cluster, and is interchangeable with the mean magnitude of the HB.

Given that metallicity is a free parameter in the isochrone models as well as dependent variable on the absolute magnitude of the HB, finding a match between the isochrone distance modulus, denoted as $\mathrm{DM_{iso}}$, and the measured distance modulus correction, $\mathrm{DM_{HB}}$, lends credence to the quality of the fit. As indicated in Figure 4.9, the isochrone and measured values of distance match nearly exactly. Looking back at Figure 4.2, the HB for Pyxis is poorly defined, and the uncertainty for $V_{\mathrm{HB}}$ reflects the standard deviation of the mean magnitude. The uncertainty for $\mathrm{DM_{HB}}$ includes this as well as the uncertainties on the coefficients in Equation 4.11 added by quadrature with the uncertainty on the mean RR Lyrae magnitude, $M_{V(RR)}$. The latter uncertainty requires some additional explanation. Adopting the notation of Chaboyer (1999, Equation 1), we rewrite Equation 4.11 as

$$M_{V(RR)} = \alpha\,[\mathrm{Fe/H}] + \beta \tag{4.12}$$

where the coefficients have associated uncertainties $\sigma_\alpha$ and $\sigma_\beta$. Employing the regular rules of error propagation, we derive a total uncertainty for the mean RR Lyrae magnitude as

$$\sigma^2_{M_{V(RR)}} = \left([\mathrm{Fe/H}]\,\sigma_\alpha\right)^2 + \left(\alpha\,\sigma_{[\mathrm{Fe/H}]}\right)^2 + \sigma^2_\beta. \tag{4.13}$$

Using the metallicity measurement of Palma et al. (2000) of $[\mathrm{Fe/H}] = -1.4 \pm 0.1$ as well as the statistical uncertainty on the mean horizontal branch magnitude shown in Figure 4.2, we find the total uncertainty $\sigma_{\mathrm{DM_{HB}}} = \pm 0.08$.

### 4.3.3 Results

Figure 4.9 shows the best fitting isochrones to the clusters along with the requisite parameters. Table 4.5 shows a side by side comparison between these results and those of D08b and D11b.

When considering side-by-side comparisons between my results and those of Dotter, an important distinction must be made in the choice of model atmosphere code. D08a offers two methods commonly referred to as "synthetic" and "empirical". The synthetic approach relies on the PHOENIX model atmosphere grid (Hauschildt et al. 1999a,b) for determination of the color-$T_{\rm eff}$ transformations and are used as boundary conditions in the stellar evolution code. The "empirical" method, which is really is really semi-empirical at best, uses the MARCS model atmospheres of VandenBerg & Clem (2003) for the Johnson-Cousins $BV(RI)_C$ system. This method is empirical in the sense that the synthetic transformation results are constrained by observational data.

Dotter, working in the HST $VI$ system, employs synthetic transformations described above whereas I use the empirical transformations based on side-by-side comparisons between the two methods using my data and the ridge lines of M5. My tests confirm Dotter's own conclusions about which to use in the $BV$ system. Quoting Dotter et al. (2008a, §4 ¶4 pg. 93) directly on the issue,

> "The synthetic colors have been tested and perform well in bandpasses equivalent to $V$ or redder (with central wavelengths longer than 5000 Å), but the blue and ultraviolet bands (with central wavelengths shorter than 5000 Å) suffer from inaccuracy of the synthetic fluxes at shorter wavelengths. In cases in which analysis in the bluer bands is important, empirical color transformations are strongly recommended."

Table 4.5 shows good agreement between my results and Dotter's. The choice of metallicity and $\alpha$ enhancement differ slightly, but they agree in a relative sense in that both Dotter and I find AM 1 and Pyxis to have the same relative chemical composition compared to each other. Dotter's reported distance moduli are based on the apparent HB magnitude. To bring them to the absolute scale for direct comparison with my results, I correct $V_{\rm HB}$ for extinction by applying Equation 4.1a with $R_V = 2.889$ corresponding to the HST WFPC

Table 4.5. Isochrone parameters compared to Dotter

| | AM 1 | | Pyxis | |
|---|---|---|---|---|
| Parameter | This work | D08b | This work | D11b |
| Age | 10.5 | 11.1 | 11.5 | $11.5 \pm 1.0$ |
| [Fe/H] | -1.40 | -1.50 | -1.40 | -1.50 |
| [$\alpha$/Fe] | +0.4 | +0.2 | +0.4 | +0.2 |
| $(m-M)_0$ | 20.36 | 20.36[a] | 17.91 | 17.92[a] |
| $E(B-V)$ | 0.005 | 0.016 | 0.24 | 0.25 |

[a]Dotter reports a distance modulus based on the apparent magnitude of the HB. The values listed here are extinction corrected for comparison with my results. See the text for details.

F606W filter (Schlegel et al. 1998, Table 6) and Dotter's adopted extinction values for each cluster to Equation 4.10. As seen in Table 4.5, Dotter's DM matches mine exactly.

## 4.4 Summary

Table 4.6 summarizes the results of the techniques used in this chapter. The isochrones agree with the hypothesis that both target clusters are of similar iron and $\alpha$ abundance as M5. Marín-Franch et al. (2009) and Carney (1996) report $[\mathrm{Fe/H}]_{\mathrm{ZW}} = -1.38$ and $-1.40$ respectively, in near perfect agreement with the results listed in Table 4.6. The most recent high resolution spectroscopic survey of M5 was undertaken by Lai et al. (2011), who report $[\mathrm{Fe/H}]_{\mathrm{I}} = -1.51 \pm 0.14$, $[\mathrm{Fe/H}]_{\mathrm{II}} = -1.42 \pm 0.09$ and $[\alpha/\mathrm{Fe}] = 0.29 \pm 0.08$.[3] Carney reports $[\alpha/\mathrm{Fe}] = +0.3 \pm 0.03$ for M5 differing from my results, but the closest input values the DSED isochrone software allow are +0.2 and +0.4.

I refer to the isochrones as a purely theoretical technique, but it requires a fair bit of empiricism. Both metallicity and extinction affect the distance calculation, the latter somewhat subtly as the correction of the absolute magnitude of the HB requires it. A delicate dance exists when finding an isochrone that best matches the data while simultaneously keeping

[3]Lai et al. (2011) does not explicitly report [$\alpha$/Fe]. The number listed represents the average of Ca, Mg and $(\mathrm{Ti_I} + \mathrm{Ti_{II}})/2$.

Table 4.6. Summary of Results

| Measurement | Technique | AM 1 | Pyxis |
|---|---|---|---|
| Age Relative to M5 (Gyr) | Horizontal Method (VBS) | −1.0 | 0.0 |
| | Vertical Method (VBLC) | −1.5 | ... |
| | Isochrones (DSED) | −1.0 | 0.0 |
| [Fe/H] | Isochrones (DSED) | −1.4 | −1.4 |
| [$\alpha$/Fe] | " | +0.4 | +0.4 |
| $E(B-V)$ | " | 0.005 | 0.24 |
| Distance Modulus | " | 20.36 | 17.91 |
| | $M_{V(RR)}$ (CC03) | 20.36 | 17.92 ± 0.08 |

the metallicity and extinction within constraints provided by independent measurements of these values as well as matching the distance parameter to that expected by the magnitude of the HB (see Equations 4.10 and 4.11.)

Three independent techniques support the principle conclusion of this work, the ages of the clusters. The initial hypothesis derives from a purely empirical technique. Two semi-empirical methods, only one of which applies to Pyxis, as well as a purely theoretical technique confirm this hypothesis. The fact that such diverse approaches show broad agreement lends considerable support to the conclusion that, compared to M5, AM 1 is 1.0 to 1.5 Gyr younger and Pyxis is the same age.

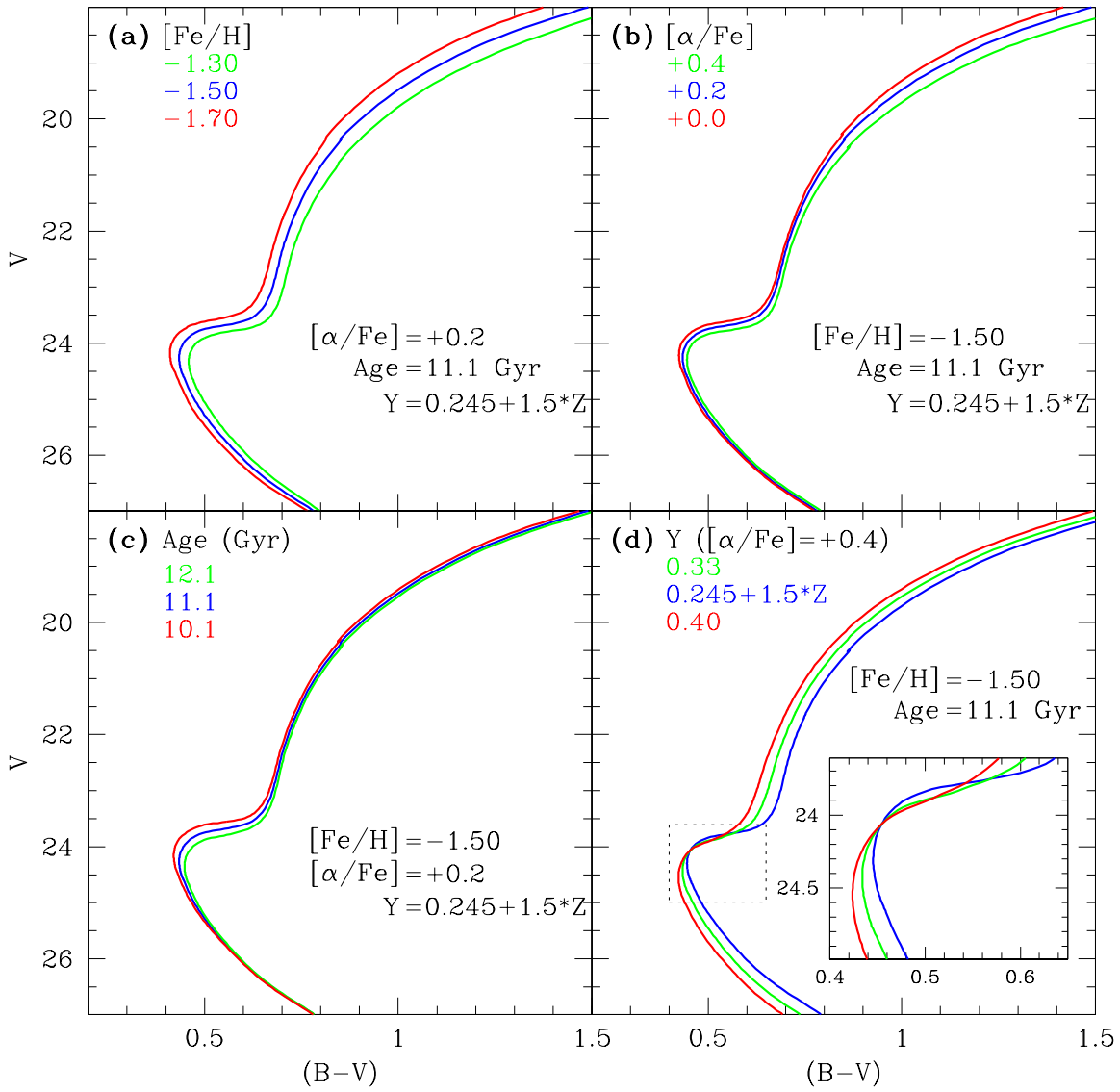


Figure 4.8 Examples of how input parameters affect the DSED models. The blue lines match the best fitting parameters for AM 1 derived by D08b. For each panel, the non-varying parameters, listed in the lower right, correspond to the blue curves in the other panels. The exception is panel (d) which required an [$\alpha$/Fe] of +0.4 as the other $Y$ values are unavailable for [$\alpha$/Fe] of +0.2 used in the other panels. The helium enrichment equation reflects the primordial helium mass fraction consistent with Spergel et al. (2003) plus the accumulation of helium along with the production of heavy metals at a rate of $\Delta Y/\Delta Z = 1.54$ (Dotter et al. 2008a, §3).

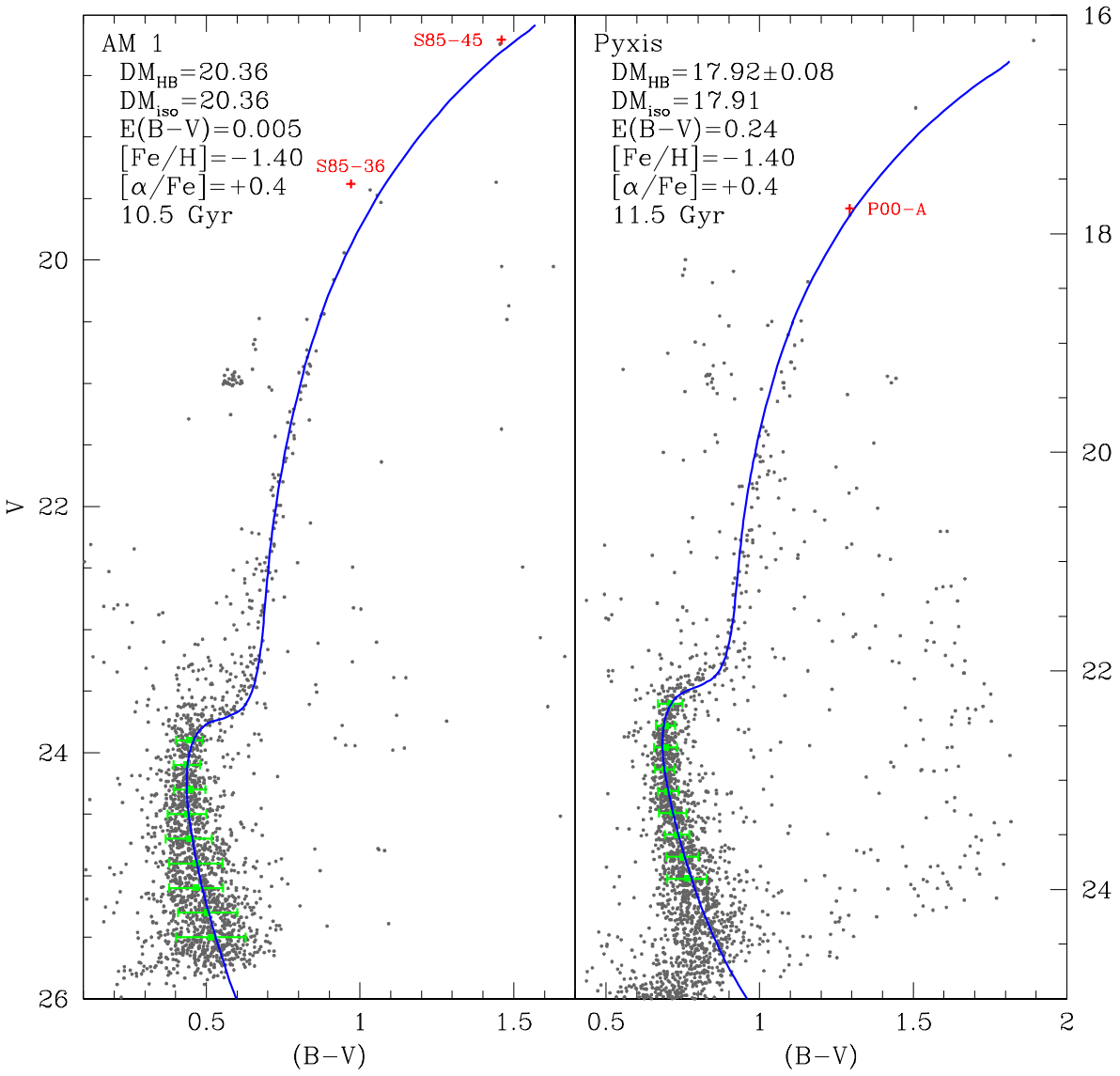


Figure 4.9 Best fitting isochrones for AM 1 and Pyxis. The green squares and error bars are the mode and FWHM of the ridge line points determined in §4.2.1 (see Figure 4.3.) The red plus signs represent stars studied in the radial velocity surveys of Suntzeff et al. (1985, S85) and Palma et al. (2000, P00) for AM 1 and Pyxis respectively. The red text corresponds to the star's identifier code listed in Table 4.4. The color for P00-A matches that of the closest star in my catalog to the converted magnitude listed in Palma et al. (2000).

# Chapter 5

# Conclusions

We discuss the results in the context of the Lee diagram, reproduced here as Figure 5.1 and with the addition of extragalactic clusters from Mackey & Gilmore (2004, Table 2). The results for AM 1 and Pyxis are shown as the solid, black pentagram in Figure 5.1. I retained their original positions from Figure 1.1, as well as M5, for comparison. I present the figure here because it drives the discussion in the subsequent sections regarding the second parameter problem and accretion. The conclusions discussed here are tenuous at best. Intermediate and high resolution spectroscopy will resolve the questions of the ultimate origins of AM 1 and Pyxis.

## 5.1 The Second Parameter Problem

It is worth noting that the results (see Figure 5.1) show that both AM 1 and Pyxis share similar metallicity to M5 but widely different HB morphologies; each cluster forming a second parameter pair with M5 similar to NGC 288/362 (Catelan et al. 2001). As we see in the subsections below, both clusters provide different explanations for this effect.

### 5.1.1 AM 1

The results for AM 1 come as little surprise. The results show a relative age of $-1.0$ to $-1.5 \pm 0.5$ Gyr compared to M5, which is consistent with age being the predominant factor in the second parameter phenomena in accordance with the conclusions of Searle & Zinn (1978), Zinn (1993) and Lee, Demarque, & Zinn (1994) to name a few.

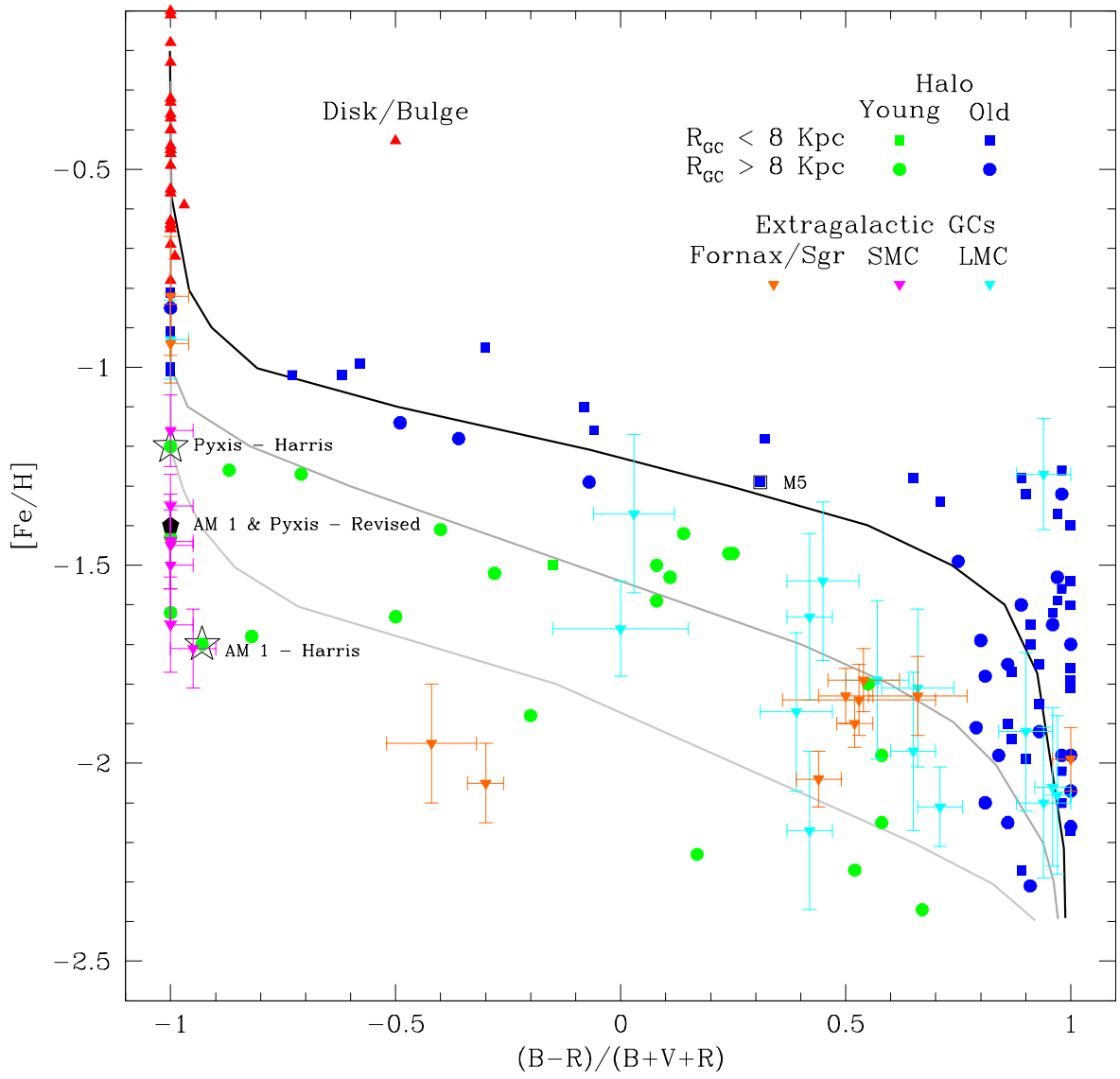


Figure 5.1 The same as Figure 1.1 but with the addition of extragalactic clusters from Mackey & Gilmore (2004, Table 2). The position of AM 1 and Pyxis based on the results of this work are shown as the solid, black pentagon and annotated as "Revised". Their original positions based on the Harris (1996, 2003 and 2010 revisions) catalog are shown as open stars and annotated as "Harris".

### 5.1.2 Pyxis

The results for Pyxis, by contrast, are quite enigmatic. Based on its position in the Lee diagram, we would expect it to be noticeably younger than M5. However, the results show no noticeable difference in age between the two (to within the uncertainties of the techniques employed, $\pm 0.5$ Gyr). The relative age of Pyxis, with respect to M5, shows that another factor, aside from age, drives the second parameter phenomena displayed in Pyxis.

This conclusion is speculative due to the poor definition of Pyxis' HB. Recall that I could not employ a statistical subtraction technique to filter foreground stars and relied on using only stars within the core radius, shown in Figure 3.7 for subsequent analysis. By comparison, the full CMD including all the "stellar noise" from foreground stars is shown in the lower right panel of Figure 3.4. The full HB of Pyxis may be bluer than determined in this work, but a more sophisticated filtering technique must be employed to disentangle it from the non-cluster sources in the CMD. The most conclusive method of determining the appropriate HB members is through kinematics, requiring high resolution spectroscopy for radial velocities, and long time baseline astrometry to establish proper motions.

Even with the best filtering and selection techniques employed, Pyxis shows a sparsely populated HB. The final uncertainty on the HB type will be large and dominated by small number statistics. Any conclusions about the second parameter problem involving Pyxis alone are dubious at best.

## 5.2 Accretion

In terms of the Lee diagram, the results of this work are consistent with AM 1 and Pyxis being an accretion relics. Mackey & Gilmore (2004) argued that younger age alone suffices to distinguish accreted GCs due to the location of most external GCs in the Lee diagram (Figure 5.1) in common with the "young halo" population described by Zinn (1993). An obvious, albeit non sequitur, conclusion from Figure 5.1 is that both Pyxis and AM 1 were

born in environments similar to the Small Magellanic Cloud (SMC).

Pyxis' similar age with M5 casts doubt on the conclusion above. To resolve this issue, we need to explore the ages of AM 1, Pyxis and M5 in the context of the MW GC system as a whole. Marín-Franch et al. (2009) surveyed 64 GC using HST data and established relative ages with a technique very similar to the empirical method I employ in §4.1. Forbes & Bridges (2010) expanded the study to 93 MW clusters. A plot of metallicity vs. age (reproduced here as Figure 5.2a), or the age-metallicity relationship (AMR), shows a bifurcated distribution with most MW clusters following a vertical trend of constant age of $\sim$ 12.8 Gyr, whereas another group of clusters follows a roughly linear trend with the youngest clusters being most metal rich. Many of the clusters in this latter group are known, or are suspected of being, members of the accreted Canis Major and Sagittarius dwarf spheroidal galaxies. They conclude that all the members of the group in the young branch of the AMR are accretion relics. VandenBerg et al. (2013) supports this conclusion with even more precise age determinations. His results (Figure 5.2b) show that the young branch of the AMR is itself bifurcated into two parallel sequences, the more metal rich of which having disk like kinematics and the metal poor show halo kinematics. .

The curious result from both Forbes & Bridges (2010) and VandenBerg et al. (2013) is that M5 lies in the young population. The fact that Pyxis is the same age as M5 does not necessarily preclude it as an accretion relic. As shown in Figure 5.2, AM 1, Pyxis and M5 all lie within the young fork of the AMR along with the accretion relics of the Canis Major and Sagittarius dSph clusters. While this alone is insufficient to make strong conclusions about the origins of these clusters, these results coupled with their positions in the Lee diagram are consistent with both AM 1 and Pyxis being accretion relics, and we are left to wonder why M5 shows a blue HB at all despite its relatively young age.

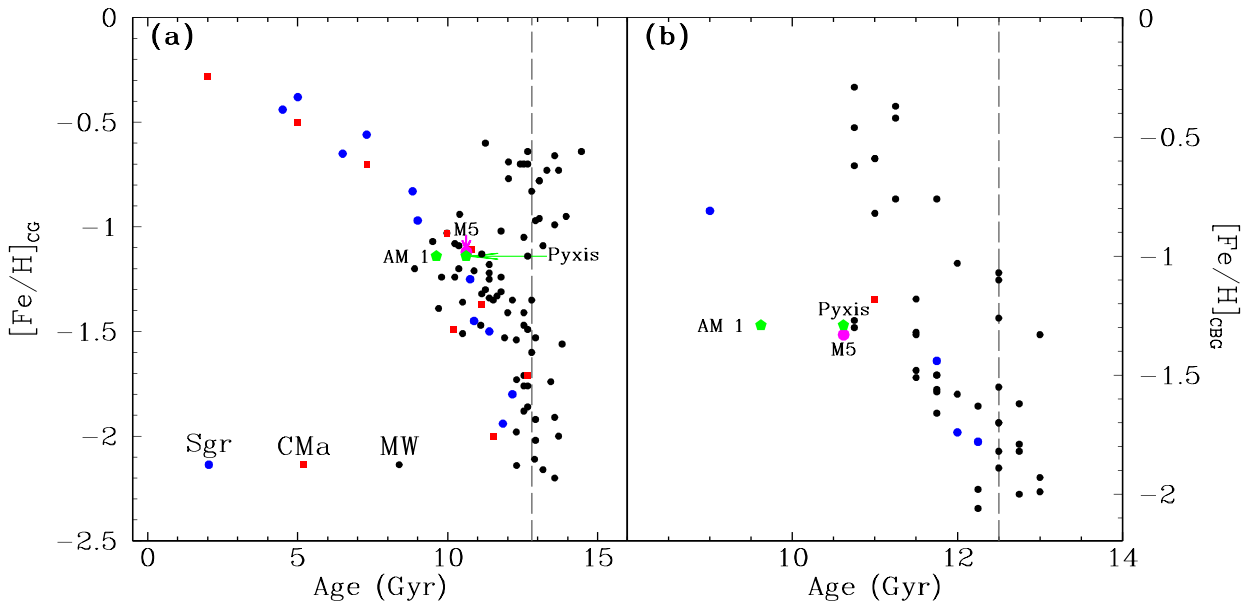


Figure 5.2 The age-metallicity relationships (AMR) based on two different datasets. The results from this study are shown as green pentagons. The magenta circle represents M5. Clusters known or believed to be associated with the Canis Major (CMa) and Sagittarius (Sgr) dSph galaxies are indicated by the legend. **(a)** AMR constructed using data from Forbes & Bridges (2010). The authors of this study use the Carretta and Graton (CG) metallicity scale. The results for AM 1 and Pyxis were transformed to this scale via Equation 3 of Carretta et al. (2001). The grey line at 12.8 Gyr indicates the mean age of the old MW population as determined by Marín-Franch et al. (2009). **(b)** AMR from VandenBerg et al. (2013) who uses the metallicity scale of Carretta et al. (2009, CBG). The dashed line at 12.5 Gyr represents their mean age for the old MW population.

## 5.3 Future Work

Many of the issues discussed here are best solved through intermediate or high resolution spectroscopy. Unfortunately, this is currently prohibitive with AM 1 and only possible with the brightest RGB stars in Pyxis. As larger telescopes and more efficient spectrographs become available, the chemical mysteries of the OH will unravel. In the interim, there are a few projects I can undertake to further explore the OH.

Astrometry supports future spectroscopic and proper motion studies. Measurement of precise positions for the stars I measured in AM 1 and Pyxis is a good first step.

As mentioned before, the problem of Pyxis being polluted by "stellar noise" needs to be addressed. One option is to use SOAR to image a nearby control field for use in the statistical subtraction technique would be relatively straightforward if the telescope time can be spared. Another approach involves the use of synthetic MW field star CMDs using the models of Robin et al. (2004).

# APPENDIX A

## Observing Logs

The complete observing log for our clusters is listed in Tables A.1 and A.2 below. The seeing was recorded as soon as the exposure ended by selecting a sample star of intermediate brightness in a non-crowded part of the field and measuring it's full width half max (FWHM) by using the IRAF `imexamine` command (specifically hovering the cursor over the sample star and hitting the `r` key). We converted the FWHM from pixels to arcseconds by multiplying by the SOI pixel resolution scale factor of 0.154 arcseconds/pixel. The results were recorded in the SOI paper logs.

Table A.1. AM1 Observations log

| Filter | UT Date (mid-exposure) | UT Time (mid-exposure) | Exposure time (seconds) | Seeing (arcseconds) | Comments |
|---|---|---|---|---|---|
| V | 2007-10-08 | 06:04:19.4 | 20.0 | 0.69 | |
| V | 2007-10-08 | 06:07:45.2 | 20.0 | 0.69 | |
| V | 2007-10-08 | 06:09:13.4 | 20.0 | 0.61 | |
| V | 2007-10-08 | 06:15:48.2 | 300.0 | 0.72 | |
| B | 2007-10-08 | 06:23:10.0 | 500.0 | 0.88 | |
| V | 2007-10-08 | 06:30:35.2 | 300.0 | 0.77 | |
| B | 2007-10-08 | 06:38:24.0 | 500.0 | 0.81 | |
| V | 2007-10-08 | 06:45:60.0 | 300.0 | 0.74 | |
| B | 2007-10-08 | 06:53:17.2 | 500.0 | 0.78 | |
| V | 2007-10-08 | 06:60:40.8 | 300.0 | 0.80 | |
| B | 2007-10-08 | 07:08:23.0 | 500.0 | 1.04 | |
| V | 2007-10-08 | 07:15:47.0 | 300.0 | 0.85 | |
| B | 2007-10-08 | 07:22:58.4 | 500.0 | 0.74 | |
| V | 2007-10-08 | 07:30:24.0 | 300.0 | 0.71 | |
| B | 2007-10-08 | 07:37:41.6 | 500.0 | 0.73 | |
| V | 2007-10-08 | 07:45:11.8 | 300.0 | 0.69 | |
| B | 2007-10-08 | 07:52:22.2 | 500.0 | 0.81 | |
| V | 2007-10-08 | 07:59:41.8 | 300.0 | 0.76 | |
| B | 2007-10-08 | 08:07:16.6 | 500.0 | 0.71 | |
| V | 2007-10-08 | 08:14:43.8 | 300.0 | 0.74 | |
| B | 2007-10-08 | 08:22:17.8 | 500.0 | 0.83 | |
| V | 2007-10-08 | 08:29:51.8 | 300.0 | 0.77 | |
| B | 2007-10-08 | 08:37:25.4 | 500.0 | 1.01 | |
| V | 2007-10-08 | 08:44:42.4 | 300.0 | 1.04 | |
| B | 2007-10-08 | 08:52:11.6 | 500.0 | 1.13 | |
| V | 2007-10-08 | 08:59:27.4 | 300.0 | 1.02 | |
| B | 2007-10-09 | 06:12:23.4 | 60.0 | 1.75 | |
| B | 2007-10-09 | 06:15:45.8 | 60.0 | 1.49 | |
| B | 2007-10-09 | 06:18:01.6 | 60.0 | 1.42 | |
| B | 2007-10-09 | 06:26:47.0 | 500.0 | 1.14 | |
| V | 2007-10-09 | 06:35:26.4 | 300.0 | 1.16 | |
| B | 2007-10-09 | 06:43:05.4 | 500.0 | 1.06 | |

Table A.1 (cont'd)

| Filter | UT Date (mid-exposure) | UT Time (mid-exposure) | Exposure time (seconds) | Seeing (arcseconds) | Comments |
|---|---|---|---|---|---|
| V | 2007-10-09 | 06:51:00.4 | 300.0 | 1.07 | |
| B | 2007-10-09 | 06:58:37.2 | 500.0 | 1.21 | |
| V | 2007-10-09 | 07:06:20.6 | 300.0 | 1.10 | |
| B | 2007-10-09 | 07:13:54.2 | 500.0 | 1.41 | |
| V | 2007-10-09 | 07:22:22.6 | 300.0 | 1.60 | |
| B | 2007-10-09 | 07:30:33.0 | 500.0 | 1.34 | |
| V | 2007-10-09 | 07:38:01.4 | 300.0 | 1.08 | |
| B | 2007-10-09 | 07:45:33.0 | 500.0 | 1.17 | Where's the V? |
| B | 2007-10-09 | 08:00:10.4 | 60.0 | 1.03 | |
| B | 2007-10-09 | 08:05:44.0 | 500.0 | 1.13 | |
| V | 2007-10-09 | 08:13:01.8 | 300.0 | 1.08 | |
| B | 2007-10-09 | 08:20:20.6 | 500.0 | 1.11 | Satellite/airplane streaks |
| B | 2007-10-09 | 08:50:00.5 | 120.0 | 9.99 | No stars visible |
| B | 2007-10-09 | 08:54:37.0 | 120.0 | 9.99 | No stars visible |
| B | 2007-10-09 | 09:01:30.6 | 60.0 | 1.05 | |
| B | 2007-10-09 | 09:05:26.4 | 60.0 | 1.10 | |
| B | 2007-10-09 | 09:10:56.0 | 500.0 | 1.12 | |
| V | 2007-10-10 | 06:11:19.3 | 20.0 | 0.87 | |
| V | 2007-10-10 | 06:13:29.4 | 20.0 | 0.95 | |
| V | 2007-10-10 | 06:16:42.0 | 300.0 | 1.04 | |
| B | 2007-10-10 | 06:27:09.2 | 500.0 | 0.87 | |
| V | 2007-10-10 | 06:35:03.8 | 300.0 | 0.80 | |
| B | 2007-10-10 | 06:42:15.8 | 500.0 | 0.73 | |
| V | 2007-10-10 | 06:49:32.6 | 300.0 | 0.68 | |
| B | 2007-10-10 | 06:57:59.0 | 500.0 | 0.71 | |
| V | 2007-10-10 | 07:05:25.0 | 300.0 | 0.69 | |
| B | 2007-10-10 | 07:13:01.2 | 500.0 | 0.71 | |
| V | 2007-10-10 | 07:21:43.1 | 300.0 | 0.69 | |
| B | 2007-10-10 | 07:29:08.2 | 500.0 | 0.67 | |
| V | 2007-10-10 | 07:36:56.0 | 300.0 | 0.70 | |
| B | 2007-10-10 | 07:44:17.8 | 500.0 | 0.78 | |
| V | 2007-10-10 | 07:51:34.2 | 300.0 | 0.85 | |

Table A.1 (cont'd)

| Filter | UT Date (mid-exposure) | UT Time (mid-exposure) | Exposure time (seconds) | Seeing (arcseconds) | Comments |
|---|---|---|---|---|---|
| B | 2007-10-10 | 07:58:43.8 | 500.0 | 0.87 | |
| V | 2007-10-10 | 08:06:01.6 | 300.0 | 0.79 | |
| B | 2007-10-10 | 08:13:12.8 | 500.0 | 0.81 | |
| V | 2007-10-10 | 08:20:33.0 | 300.0 | 0.83 | |
| B | 2007-10-10 | 08:27:47.4 | 500.0 | 0.84 | |
| V | 2007-10-10 | 08:35:19.4 | 300.0 | 0.81 | |
| B | 2007-10-10 | 08:42:34.4 | 500.0 | 0.84 | |
| V | 2007-10-10 | 08:49:46.6 | 300.0 | 0.76 | |
| B | 2007-10-10 | 08:57:40.2 | 500.0 | 0.84 | |
| V | 2007-11-14 | 04:18:20.5 | 600.0 | 0.53 | Photometric night, |
| B | 2007-11-14 | 04:32:28.3 | 900.0 | 0.58 | standards observed |
| V | 2007-11-14 | 04:46:31.9 | 600.0 | 0.53 | |
| B | 2007-11-14 | 04:59:55.1 | 900.0 | 0.57 | |
| V | 2007-11-14 | 05:13:08.7 | 600.0 | 0.53 | |
| B | 2007-11-14 | 05:26:23.8 | 900.0 | 0.64 | |
| V | 2007-11-14 | 05:39:38.3 | 600.0 | 0.58 | |
| B | 2007-11-14 | 05:52:41.8 | 900.0 | 0.65 | |
| V | 2007-11-14 | 06:06:00.3 | 600.0 | 0.72 | |
| B | 2007-11-14 | 06:19:35.5 | 900.0 | 0.70 | |
| V | 2007-11-14 | 06:34:55.3 | 600.0 | 0.64 | |
| B | 2007-11-14 | 06:48:08.5 | 900.0 | 0.74 | |
| V | 2007-11-14 | 07:01:57.5 | 600.0 | 0.75 | |
| V | 2007-11-15 | 04:54:16.0 | 20.0 | 0.60 | Photometric night, |
| V | 2007-11-15 | 04:54:52.0 | 20.0 | 0.64 | standards observed. |
| V | 2007-11-15 | 04:55:28.0 | 20.0 | 0.67 | |
| B | 2007-11-15 | 04:58:14.0 | 40.0 | 0.70 | |
| B | 2007-11-15 | 04:59:10.0 | 40.0 | 0.77 | |
| B | 2007-11-15 | 05:00:06.0 | 40.0 | 0.87 | |
| V | 2007-11-15 | 05:06:18.1 | 600.0 | 0.80 | |
| B | 2007-11-15 | 05:19:12.1 | 900.0 | 0.75 | |
| V | 2007-11-15 | 05:32:05.0 | 600.0 | 0.82 | |
| B | 2007-11-15 | 05:45:12.0 | 900.0 | 0.82 | |

Table A.1 (cont'd)

| Filter | UT Date (mid-exposure) | UT Time (mid-exposure) | Exposure time (seconds) | Seeing (arcseconds) | Comments |
|---|---|---|---|---|---|
| V | 2007-11-15 | 05:58:22.1 | 600.0 | 0.86 | |
| B | 2007-11-15 | 06:11:35.0 | 900.0 | 0.76 | |
| V | 2007-11-15 | 06:24:42.1 | 600.0 | 0.63 | |
| B | 2007-11-15 | 06:37:51.1 | 900.0 | 0.73 | |
| V | 2007-11-15 | 06:51:04.0 | 600.0 | 0.53 | |
| V | 2007-12-11 | 02:45:41.5 | 600.0 | 0.83 | First half of night photometric. |
| B | 2007-12-11 | 02:58:55.9 | 900.0 | 0.97 | standards observed. |
| V | 2007-12-11 | 03:12:08.1 | 600.0 | 0.92 | |
| B | 2007-12-11 | 03:25:21.9 | 900.0 | 0.89 | |
| V | 2007-12-11 | 03:38:28.3 | 600.0 | 0.89 | |
| V | 2007-12-11 | 04:35:27.5 | 600.0 | 0.76 | |
| B | 2007-12-11 | 04:48:35.3 | 900.0 | 0.77 | Cirrus clouds reported around |
| V | 2007-12-11 | 05:01:50.7 | 600.0 | 0.73 | this time. |
| V | 2008-01-04 | 02:12:32.2 | 60.0 | 0.67 | Trial exposure |
| V | 2008-01-04 | 02:19:04.0 | 600.0 | 0.73 | Master V frame for AM 1 |
| B | 2008-01-04 | 02:32:13.0 | 900.0 | 0.75 | Master B frame for AM 1 |
| V | 2008-01-04 | 02:45:24.0 | 600.0 | 0.74 | |
| B | 2008-01-04 | 02:59:04.2 | 900.0 | 0.79 | |
| V | 2008-01-04 | 03:12:46.4 | 600.0 | 0.83 | |
| B | 2008-01-04 | 03:26:01.6 | 900.0 | 0.87 | |
| V | 2008-01-04 | 03:39:18.7 | 600.0 | 0.75 | |
| V | 2008-01-05 | 01:00:40.6 | 60.0 | 0.70 | |
| V | 2008-01-05 | 01:01:52.5 | 60.0 | 0.69 | |
| V | 2008-01-05 | 01:03:03.4 | 60.0 | 0.62 | |
| V | 2008-01-05 | 01:04:16.1 | 60.0 | 0.62 | |
| V | 2008-01-05 | 01:11:44.6 | 600.0 | 0.70 | |
| B | 2008-01-05 | 01:25:34.0 | 900.0 | 0.95 | |
| V | 2008-01-05 | 01:38:50.8 | 600.0 | 0.83 | |
| B | 2008-01-05 | 01:51:58.8 | 900.0 | 0.85 | |
| V | 2008-01-05 | 02:05:15.0 | 600.0 | 0.73 | |
| B | 2008-01-05 | 02:18:19.8 | 900.0 | 0.75 | |
| V | 2008-01-05 | 02:31:26.2 | 600.0 | 0.79 | |

Table A.1 (cont'd)

| Filter | UT Date (mid-exposure) | UT Time (mid-exposure) | Exposure time (seconds) | Seeing (arcseconds) | Comments |
|---|---|---|---|---|---|
| B | 2008-01-05 | 02:44:29.8 | 900.0 | 0.75 | |
| V | 2008-01-05 | 02:57:41.8 | 600.0 | 0.76 | |
| B | 2008-01-05 | 03:10:49.3 | 900.0 | 0.68 | |
| V | 2008-01-05 | 03:23:51.6 | 600.0 | 0.70 | |
| V | 2008-02-02 | 01:15:36.0 | 60.0 | 1.06 | Test exposure |
| V | 2008-02-02 | 01:23:43.4 | 600.0 | 1.09 | Transparency poor (cloudy) |
| B | 2008-02-02 | 01:36:54.2 | 900.0 | 1.05 | Transparency improved around 0143 UT |
| V | 2008-02-02 | 01:50:18.4 | 600.0 | 0.85 | Clearing |
| B | 2008-02-02 | 02:03:47.4 | 900.0 | 0.92 | Clear |
| V | 2008-02-02 | 02:17:01.8 | 600.0 | 1.01 | |
| V | 2008-12-23 | 01:41:10.1 | 600.0 | 0.74 | |
| B | 2008-12-23 | 01:58:14.5 | 900.0 | 0.77 | |
| V | 2008-12-23 | 02:11:22.1 | 600.0 | 0.68 | |
| B | 2008-12-23 | 02:24:21.7 | 900.0 | 0.82 | |
| V | 2008-12-23 | 02:37:26.1 | 600.0 | 0.65 | |
| B | 2008-12-23 | 02:50:23.3 | 900.0 | 0.68 | |
| V | 2008-12-23 | 03:03:18.3 | 600.0 | 0.77 | |
| B | 2008-12-23 | 03:16:25.9 | 900.0 | 0.57 | |
| V | 2008-12-23 | 03:29:23.3 | 600.0 | 0.64 | |
| V | 2009-01-31 | 01:13:01.0 | 600.0 | 0.64 | |
| B | 2009-01-31 | 01:26:02.3 | 900.0 | 0.65 | |
| V | 2009-01-31 | 01:38:59.4 | 600.0 | 0.65 | |
| B | 2009-01-31 | 02:06:37.4 | 900.0 | 0.98 | |
| V | 2009-01-31 | 02:19:44.9 | 600.0 | 1.06 | |
| B | 2009-01-31 | 02:32:44.2 | 900.0 | 0.97 | |
| V | 2009-01-31 | 02:45:42.4 | 600.0 | 0.95 | |

Table A.2. Pyxis Observations log

| Filter | UT Date (mid-exposure) | UT Time (mid-exposure) | Exposure time (seconds) | Seeing (arcseconds) | Comments |
|---|---|---|---|---|---|
| V | 2007-11-14 | 07:52:09.7 | 300.0 | 0.65 | Photometric night, |
| B | 2007-11-14 | 07:59:13.1 | 500.0 | 0.69 | standards observed. |
| V | 2007-11-14 | 08:06:31.7 | 300.0 | 0.64 | |
| B | 2007-11-14 | 08:13:14.5 | 500.0 | 0.68 | |
| V | 2007-11-14 | 08:20:32.9 | 300.0 | 0.61 | |
| V | 2007-11-14 | 08:23:25.3 | 10.0 | 0.65 | |
| V | 2007-11-14 | 08:23:47.1 | 10.0 | 0.62 | |
| V | 2007-11-14 | 08:24:09.3 | 10.0 | 0.67 | |
| B | 2007-11-14 | 08:25:07.7 | 20.0 | 0.64 | |
| B | 2007-11-14 | 08:25:39.5 | 20.0 | 0.63 | |
| B | 2007-11-14 | 08:26:11.1 | 20.0 | 0.66 | |
| V | 2007-11-15 | 07:30:36.0 | 300.0 | 0.50 | Photometric night, |
| B | 2007-11-15 | 07:38:01.1 | 500.0 | 0.57 | standards observed. |
| V | 2007-11-15 | 07:45:37.1 | 300.0 | 0.55 | UT dates and times had to be |
| B | 2007-11-15 | 07:53:06.1 | 500.0 | 0.64 | derived this night due to an |
| V | 2007-11-15 | 08:00:59.1 | 300.0 | 0.57 | acquisition software error |
| B | 2007-11-15 | 08:08:16.1 | 500.0 | 0.55 | |
| V | 2007-11-15 | 08:15:25.1 | 300.0 | 0.51 | ?? (time dosen't make sense) |
| V | 2007-11-15 | 08:13:33.0 | 10.0 | 0.52 | |
| V | 2007-11-15 | 08:13:59.0 | 10.0 | 0.53 | |
| V | 2007-11-15 | 08:14:25.0 | 10.0 | 0.53 | |
| B | 2007-11-15 | 08:15:14.5 | 15.0 | 0.56 | |
| B | 2007-11-15 | 08:15:45.5 | 15.0 | 0.56 | |
| B | 2007-11-15 | 08:16:16.5 | 15.0 | 0.56 | |
| B | 2008-01-04 | 04:28:35.4 | 30.0 | 1.00 | |
| B | 2008-01-04 | 04:29:17.2 | 30.0 | 0.80 | |
| B | 2008-01-04 | 04:29:58.6 | 30.0 | 0.86 | |
| V | 2008-01-04 | 04:31:34.9 | 15.0 | 0.78 | |
| V | 2008-01-04 | 04:32:01.3 | 15.0 | 0.72 | |
| V | 2008-01-04 | 04:32:29.1 | 15.0 | 0.78 | |
| V | 2008-01-04 | 04:36:48.3 | 300.0 | 0.81 | |
| B | 2008-01-04 | 04:44:27.2 | 500.0 | 0.84 | |

Table A.2 (cont'd)

| Filter | UT Date (mid-exposure) | UT Time (mid-exposure) | Exposure time (seconds) | Seeing (arcseconds) | Comments |
|---|---|---|---|---|---|
| V | 2008-01-04 | 04:52:04.3 | 300.0 | 0.70 | |
| B | 2008-01-04 | 05:02:04.2 | 500.0 | 0.75 | |
| V | 2008-01-04 | 05:10:06.0 | 300.0 | 0.73 | |
| B | 2008-01-04 | 05:17:22.6 | 500.0 | 0.78 | |
| V | 2008-01-04 | 05:25:45.1 | 300.0 | 0.74 | |
| B | 2008-01-04 | 05:33:11.0 | 500.0 | 0.76 | |
| V | 2008-01-04 | 05:41:05.4 | 300.0 | 0.77 | |
| B | 2008-01-04 | 05:50:41.0 | 500.0 | 0.87 | |
| V | 2008-01-04 | 05:57:56.2 | 300.0 | 0.81 | |
| B | 2008-01-04 | 06:09:31.8 | 500.0 | 0.76 | |
| V | 2008-01-04 | 06:16:51.8 | 300.0 | 0.67 | Master V frame for Pyxis |
| B | 2008-01-04 | 06:24:08.0 | 500.0 | 0.66 | Master B frame for Pyxis |
| V | 2008-01-04 | 06:31:40.4 | 300.0 | 0.69 | |
| B | 2008-01-04 | 06:39:01.8 | 500.0 | 0.70 | |
| V | 2008-01-04 | 06:46:21.2 | 300.0 | 0.74 | |
| V | 2008-01-05 | 03:41:46.6 | 30.0 | 0.81 | |
| V | 2008-01-05 | 03:46:27.6 | 300.0 | 0.78 | |
| B | 2008-01-05 | 03:53:47.4 | 500.0 | 0.84 | |
| V | 2008-01-05 | 04:00:57.1 | 300.0 | 0.75 | |
| B | 2008-01-05 | 04:08:19.4 | 500.0 | 0.77 | |
| V | 2008-01-05 | 04:17:26.7 | 300.0 | 0.65 | |
| B | 2008-01-05 | 04:25:49.0 | 500.0 | 0.80 | |
| V | 2008-01-05 | 04:36:37.8 | 300.0 | 0.66 | |
| B | 2008-01-05 | 04:43:58.6 | 500.0 | 0.65 | |
| V | 2008-01-05 | 04:51:25.0 | 300.0 | 0.61 | |
| B | 2008-01-05 | 04:58:40.5 | 500.0 | 0.68 | |
| V | 2008-01-05 | 05:06:35.8 | 300.0 | 0.70 | |
| B | 2008-01-05 | 05:13:46.6 | 500.0 | 0.80 | |
| V | 2008-01-05 | 05:20:53.0 | 300.0 | 0.76 | |
| V | 2008-02-02 | 02:31:49.9 | 15.0 | 0.95 | Clouds were an issue this entire night |
| V | 2008-02-02 | 02:32:19.7 | 15.0 | 0.95 | |
| V | 2008-02-02 | 02:32:48.3 | 15.0 | 0.95 | |

Table A.2 (cont'd)

| Filter | UT Date (mid-exposure) | UT Time (mid-exposure) | Exposure time (seconds) | Seeing (arcseconds) | Comments |
|---|---|---|---|---|---|
| B | 2008-02-02 | 02:33:46.8 | 30.0 | 1.14 | |
| B | 2008-02-02 | 02:34:31.6 | 30.0 | 1.14 | |
| B | 2008-02-02 | 02:35:14.8 | 30.0 | 1.14 | Focus soft, tweaking optics |
| V | 2008-02-02 | 02:50:46.2 | 300.0 | 0.71 | Focus improved |
| B | 2008-02-02 | 02:57:56.8 | 500.0 | 0.81 | |
| V | 2008-02-02 | 03:05:24.8 | 300.0 | 0.79 | |
| B | 2008-02-02 | 03:12:49.2 | 500.0 | 0.85 | |
| V | 2008-02-02 | 03:20:11.4 | 300.0 | 0.84 | |
| B | 2008-02-02 | 03:27:27.8 | 500.0 | 0.82 | |
| V | 2008-02-02 | 03:34:54.4 | 300.0 | 0.77 | |
| B | 2008-02-02 | 03:42:05.9 | 500.0 | 0.86 | |
| V | 2008-02-02 | 03:49:19.8 | 300.0 | 0.83 | |
| B | 2008-02-02 | 03:56:41.2 | 500.0 | 0.92 | |
| V | 2008-02-02 | 04:03:56.3 | 300.0 | 0.85 | |
| B | 2008-02-02 | 04:11:11.2 | 500.0 | 0.83 | |
| V | 2008-02-02 | 04:18:24.2 | 300.0 | 0.79 | |
| B | 2008-02-02 | 04:25:36.0 | 500.0 | 0.99 | Poor transparency |
| V | 2008-02-02 | 04:32:51.7 | 300.0 | 1.01 | Target obscured by clouds |
| V | 2008-02-02 | 06:04:50.9 | 300.0 | 0.85 | Clear enough to resume |
| B | 2008-02-02 | 06:13:26.4 | 500.0 | 0.86 | |
| V | 2008-02-02 | 06:20:46.4 | 300.0 | 1.06 | Clouds back |
| V | 2008-03-06 | 00:56:22.1 | 300.0 | 0.69 | Photometric night |
| B | 2008-03-06 | 01:03:43.3 | 500.0 | 0.78 | |
| V | 2008-03-06 | 01:10:56.1 | 300.0 | 0.65 | |
| B | 2008-03-06 | 01:18:14.0 | 500.0 | 0.67 | |
| V | 2008-03-06 | 01:25:40.5 | 300.0 | 0.67 | |
| B | 2008-03-06 | 01:33:10.1 | 500.0 | 0.71 | |
| V | 2008-03-06 | 01:40:41.5 | 300.0 | 0.67 | |
| B | 2008-03-06 | 01:47:55.7 | 500.0 | 0.69 | |
| V | 2008-03-06 | 01:55:14.9 | 300.0 | 0.68 | |
| B | 2008-03-06 | 02:03:07.0 | 500.0 | 0.70 | |
| V | 2008-03-06 | 02:10:18.5 | 300.0 | 0.65 | |

Table A.2 (cont'd)

| Filter | UT Date (mid-exposure) | UT Time (mid-exposure) | Exposure time (seconds) | Seeing (arcseconds) | Comments |
|---|---|---|---|---|---|
| B | 2008-03-06 | 02:17:40.8 | 500.0 | 0.66 | |
| V | 2008-03-06 | 02:24:49.9 | 300.0 | 0.69 | |
| V | 2008-03-06 | 02:44:26.0 | 300.0 | 0.73 | |
| B | 2008-03-06 | 02:51:41.9 | 500.0 | 0.68 | |
| V | 2008-03-06 | 02:58:50.7 | 300.0 | 0.67 | |
| B | 2008-03-06 | 03:06:11.7 | 500.0 | 0.79 | |
| V | 2008-03-06 | 03:13:46.0 | 300.0 | 0.86 | |
| B | 2008-03-06 | 03:21:04.9 | 500.0 | 0.82 | |
| V | 2008-03-06 | 03:28:20.0 | 300.0 | 0.85 | |
| B | 2008-03-06 | 03:36:09.6 | 500.0 | 0.86 | |
| V | 2008-03-06 | 03:43:32.1 | 300.0 | 0.75 | |
| V | 2008-04-14 | 00:07:07.0 | 300.0 | 0.99 | Photometric night |
| B | 2008-04-14 | 00:14:31.2 | 500.0 | 1.03 | standards observed. |
| V | 2008-04-14 | 00:22:02.0 | 300.0 | 0.98 | |
| B | 2008-04-14 | 00:29:17.0 | 500.0 | 1.00 | |
| V | 2008-04-14 | 00:36:31.4 | 300.0 | 0.93 | |
| B | 2008-04-14 | 00:43:55.6 | 500.0 | 0.94 | |
| V | 2008-04-14 | 00:51:26.0 | 300.0 | 0.90 | |
| V | 2008-05-08 | 23:26:56.3 | 300.0 | 0.71 | |
| B | 2008-05-08 | 23:34:17.0 | 500.0 | 0.80 | |
| V | 2008-05-08 | 23:41:37.3 | 300.0 | 0.78 | |
| B | 2008-05-08 | 23:48:36.3 | 500.0 | 0.76 | |
| V | 2008-05-08 | 23:55:41.4 | 300.0 | 0.68 | |
| B | 2008-05-08 | 00:02:54.4 | 500.0 | 0.75 | |
| V | 2008-05-09 | 00:10:00.3 | 300.0 | 0.72 | |
| B | 2008-05-09 | 00:17:21.4 | 500.0 | 0.80 | |
| V | 2008-05-09 | 00:24:37.6 | 300.0 | 0.71 | |
| B | 2008-05-09 | 00:31:51.2 | 500.0 | 0.85 | |
| V | 2008-05-09 | 00:39:56.4 | 300.0 | 1.02 | |
| B | 2008-05-09 | 00:47:03.5 | 500.0 | 0.99 | |
| V | 2008-05-09 | 00:54:11.8 | 300.0 | 0.89 | |
| V | 2008-12-23 | 03:42:33.7 | 300.0 | 0.89 | Airmass 1.56 and decreasing |

Table A.2 (cont'd)

| Filter | UT Date (mid-exposure) | UT Time (mid-exposure) | Exposure time (seconds) | Seeing (arcseconds) | Comments |
|---|---|---|---|---|---|
| B | 2008-12-23 | 03:50:53.3 | 500.0 | 0.99 | |
| V | 2008-12-23 | 03:58:07.3 | 300.0 | 0.77 | |
| B | 2008-12-23 | 04:05:20.5 | 500.0 | 0.84 | |
| V | 2008-12-23 | 04:12:28.9 | 300.0 | 0.82 | |
| B | 2008-12-23 | 04:19:38.9 | 500.0 | 0.90 | |
| V | 2008-12-23 | 04:27:45.5 | 300.0 | 0.84 | |
| B | 2008-12-23 | 04:34:53.7 | 500.0 | 0.93 | |
| V | 2008-12-23 | 04:42:06.7 | 300.0 | 0.75 | |
| B | 2008-12-23 | 04:49:22.7 | 500.0 | 0.87 | |
| V | 2008-12-23 | 04:56:55.3 | 300.0 | 0.81 | |
| B | 2008-12-23 | 05:04:08.2 | 500.0 | 0.91 | |
| V | 2008-12-23 | 05:11:27.1 | 300.0 | 0.85 | |
| B | 2008-12-23 | 05:18:33.9 | 500.0 | 0.89 | |
| V | 2008-12-23 | 05:25:44.1 | 300.0 | 0.77 | |
| V | 2008-12-23 | 05:29:07.2 | 15.0 | 0.69 | Short exposures for |
| V | 2008-12-23 | 05:29:29.0 | 15.0 | 0.69 | bright stars. |
| V | 2008-12-23 | 05:29:50.6 | 15.0 | 0.69 | |
| B | 2008-12-23 | 05:31:07.5 | 30.0 | 0.78 | |
| B | 2008-12-23 | 05:31:44.3 | 30.0 | 0.78 | |
| B | 2008-12-23 | 05:32:20.9 | 30.0 | 0.78 | |
| V | 2009-01-30 | 01:42:49.0 | 300.0 | 0.8 | |
| B | 2009-01-30 | 01:50:51.1 | 500.0 | 1.1 | |
| V | 2009-01-30 | 01:58:19.8 | 300.0 | 1.0 | |
| B | 2009-01-30 | 02:06:00.0 | 500.0 | 1.1 | |
| V | 2009-01-30 | 02:13:51.4 | 300.0 | 0.9 | |
| B | 2009-01-30 | 02:21:29.5 | 500.0 | 1.1 | |
| V | 2009-01-30 | 02:29:08.0 | 300.0 | 1.0 | |
| B | 2009-01-30 | 02:36:59.2 | 500.0 | 1.1 | |
| V | 2009-01-30 | 02:44:57.0 | 300.0 | 1.0 | |
| B | 2009-01-30 | 02:52:48.6 | 500.0 | 1.0 | |
| V | 2009-01-30 | 03:00:13.4 | 300.0 | 1.0 | |
| B | 2009-01-30 | 03:07:38.6 | 500.0 | 1.0 | |

Table A.2 (cont'd)

| Filter | UT Date (mid-exposure) | UT Time (mid-exposure) | Exposure time (seconds) | Seeing (arcseconds) | Comments |
|---|---|---|---|---|---|
| V | 2009-01-30 | 03:16:41.2 | 300.0 | 1.0 | |
| V | 2009-01-31 | 03:00:49.4 | 300.0 | 0.88 | |
| B | 2009-01-31 | 03:07:55.4 | 500.0 | 0.90 | |
| V | 2009-01-31 | 03:15:00.2 | 300.0 | 0.89 | |
| B | 2009-01-31 | 03:22:07.6 | 500.0 | 0.89 | |
| V | 2009-01-31 | 03:29:10.6 | 300.0 | 0.85 | |
| B | 2009-01-31 | 03:36:27.6 | 500.0 | 0.86 | |
| V | 2009-01-31 | 03:43:49.2 | 300.0 | 0.83 | |
| B | 2009-01-31 | 03:51:19.6 | 500.0 | 0.76 | |
| V | 2009-01-31 | 03:58:26.1 | 300.0 | 0.63 | |

# APPENDIX B

## Source Code

The following is the source code for the perl script `daofun`.

```
#!/usr/bin/perl
$| = 1;

use Getopt::Long;
use File::Copy;

#################################################################################################
#
# Okay, so running DAOPHOT on the hundreds of frames that I have is going to
# give me carpal tunnel.  I'm to the point now that I can automate the general
# procedure.  Other automation routines, namely 'daopsffind' and 'daopsfmark'
# will be used in conjunction with this script.  This will not be a fully
# automated procedure, but I'm going to at least automate as much as I can.
#
# General procedure:
#
#       run DAOPHOT, use FIND, PHOT and PICK to generate the PSF star
#               candidate list
#
#       Either pick out the PSF stars by hand or use 'daopsffind' to find
#               them based on a decent initial guess file.
#
#       Run this script.  It will pause between the first (file index 0)
#       and second (file index 1) iterations and prompt the user to
#       prune the PSF star list for defective PSF stars (eg. due to close
#       CR hits).
#
#       Script will complete the final DAOPHOT iteration, exit and call
#       ALLSTAR.
#
#
# Usage
#       daofun [input fits file] [output file basename] <options>
#
#       options
#
#               --path  Path to the data directory.  This will construct
#                       the environment variable DAODIR set to the path
#                       specified and call DAOPHOT and ALLSTAR using
#                       Stetson's environment variable friendly syntax
#                       (eg. attach DAODIR:somefile.fits).  If this is
#                       not specified, the input frame is assumed to be
#                       in the directory in which the script was called.
#                       If the environment variable DAODIR is already defined,
#                       it is overridden while the script executes.
#
#               --noclean  The script will creat batch files that are then
#                       fed to DAOPHOT using the redirect operator
#                       (eg. daophot < batch1.cmd).  This switch prevents
#                       these files from being deleted.  Useful for debugging
#                       and/or doccumentation.
#
#               --noop  Set up everything, but don't actually execute the
#                       DAOPHOT command.  Useful for debugging and
#                       troubleshooting.
#
#               --verbose | v   Verbose output (as usual)
```

```
#
#               --debug | d     Debugging output (again as usual)
#
# Outputs
#
#       This will preserve all output files.  In the notation below, the
#       annotation [iter] refers to the iteration (typically 0, 1, or 2).
#       Unless otherwise specified, iter=1 is the final iteration.
#       [basename] is the user supplied output basename.
#
#       Just to be explicit, the bracket characters ('[' and ']') below
#       do not literally appear in the filename.  They indicate user supplied
#       or variable name strings.
#
#               [basename].[iter].psf   # PSF file (final iter is 2).
#               [basename].[iter].nei   # Neighbors file (final iter is 2).
#               [basename].[iter].grp   # output of the GROUP command
#               [basename].[iter].nst   # output of the NSTAR command
#               [basename].sub.[iter].fits  # SUBSTAR output with PSF stars
#                                           # and their neighbors for
#                                           # the given iteration subtracted.
#               [basename].subN.fits    # Final image with just the PSF stars
#                                       # with neighbors subtracted away
#               [basename].ap           # Initial guess of the magnitudes and
#                                       # positions
#               [basename].als          # Final magnitudes from ALLSTAR
#               [basename].allsub.fits  # Subtracted ALLSTAR image.
#
#
# NOTES
#
#       This script makes heavy use of the perl 'system' command.
#       IT IS VERY BAD TO INTERRUPT A SYSTEM COMMAND!  Be very cautious when
#       considering CTRL-C (terminate) or CTRL-Z (suspend) keystrokes.
#       Particularly when it appears DAOPHOT or ALLSTAR appears to be running.
#
#
###############################################################################

# Global variables
$daophot = "/usr/local/bin/daophot";
$allstar = "/usr/local/bin/allstar";
@CleanupFiles;

ReadArgs();
PrintArgs() if $debug;

# Test for the existence of required input and configuration files
if (! -e "daophot.opt")
{
die "Required configuration file 'daophot.opt' not found in current directory.\n";
}

if (! -e "photo.opt")
{
die "Required configuration file 'photo.opt' not found in current directory.\n";
}

if (! -e "allstar.opt")
{
die "Required configuration file 'allstar.opt' not found in current directory.\n";
}

Iterate ("0");

print
```

```
"\n## First iteration complete.  A new PSF star list file has been created in the\n";
print
"## data directory with the extension '.1.lst'.  Take a moment to examine the\n";
print
"## subtracted image (extension '.sub.0.fits') and prune out bad PSF stars\n";
print
"## from the new list.  Look out for cosmic rays within the PSF radius, \n";
print
"## faint background stars not being subtracted away, etc.  When ready to\n";
print
"## continue, type 'y' at the prompt below.  Type 'n' to end the program\n";
print
"## cleanly.\n\n";

print "## Proceed to the second iteration? (y/n) ";

if (QueryUser())  {
  print "## Very well, proceeding to the next iteration\n" if $verbose;
}
else
{
  print "## Allrighty then, have a great day!\n" if $verbose;
  exit;
}

Iterate ("1");

print
"## The results of the second iteration can be inspected by viewing the \n";
print
"## file with the extension 'sub.1.fits'. Verify that all the PSF stars have\n";
print
"## been cleanly subtracted away.  When ready to continue to the final \n";
print
"## iteration, type 'y' at the prompt below.  Type 'n' to end the program\n";
print
"## cleanly.\n";

print "## Proceed to the final iteration? (y/n) ";

if (QueryUser())  {
  print "## Very well, proceeding to the final iteration\n" if $verbose;
}
else
{
  print "## Allrighty then, have a great day!\n" if $verbose;
  exit;
}

Iterate ("2");

print
"## DAOPHOT it complete.  The final PSF file has the extension '.2.psf'. \n";
print
"## The next step is to run ALLSTAR, wich you can choose to do now by \n";
print
"## selecting 'y' at the prompt below.  Select 'n' to cleanly exit the\n";
print
"## program.\n";

print "## Proceed with ALLSTAR? (y/n) ";

if (QueryUser())  {
  print "## Very well, proceeding to the final iteration\n" if $verbose;
}
else
```

```
{
  print "## Allrighty then, have a great day!\n" if $verbose;
  exit;
}

RunAllstar();

# Cleanup the batch files
if ($clean)
{
  print "## Deleting the following batch files:\n\t@CleanupFiles\n" if $verbose;
  unlink (@CleanupFiles);
}
else
{
  print "## noclean enabled.  The following batch files will remain in the current\n";
  print "## directory\n";
  print "\t@CleanupFiles";
}

###############################################################################################
#
#       Subprocess: ReadArgs
#
#       Inputs: None
#
#       Returns: Nothing
#
#       Description: Reads command line options.  Defaults are set if no
#               options are given.
#
###############################################################################################

sub ReadArgs  {

  # assign defaults
  $verbose=0;
  $debuvg=0;
  $noop=0;
  $clean=1;
  $force=0;
  $datapath .= "";

  # Get the options.  This should parse the ARGV array so that the only
  # thing left are the required arguments.

  &GetOptions ("path=s",
               "noop",
               "noclean",
               "force|f",
               "verbose|v",
               "debug|d");

  if ( $opt_path )  {
    $datapath = $opt_path;
  }

  if ( $opt_noop )  {
    $noop = $opt_noop;
  }

  if ( $opt_noclean )  {
    $clean = 0;
  }

  if ( $opt_verbose )  {
```

```
    $verbose = $opt_verbose;
  }

  if ( $opt_debug )  {
    $debug = $opt_debug;
  }

  if ( $opt_force )  {
    $force = $opt_force;
  }

  # Now trap the required arguments

  $infile = @ARGV[0];

  $basename = @ARGV[1];

  if (! $infile || ! $basename)
  {
    Usage();
    exit;
  }

  if (! $datapath)
  {
    $datapath = ".";
  }
}

##############################################################################################
#
#       Usage
#
#       Educate the user on how to use the program
#
##############################################################################################

sub Usage()  {

  print "\nUsage: daofun [input fits file] [output file basename] <options>";
  print "\n\n";

  print "       options\n";
  print "\n";
  print "              --path  Path to the data directory.  This will construct\n";
  print "                      the environment variable DAODIR set to the path\n";
  print "                      specified and call DAOPHOT and ALLSTAR using\n";
  print "                      Stetson's environment variable friendly syntax\n";
  print "                      (eg. attach DAODIR:somefile.fits).  If this is\n";
  print "                      not specified, the input frame is assumed to be\n";
  print "                      in the directory in which the script was called.\n";
  print "                      If the environment variable DAODIR is already defined,\n";
  print "                      it is overridden while the script executes.\n";
  print "\n";
  print "              --noclean  The script will creat batch files that are then\n";
  print "                      fed to DAOPHOT using the redirect operator\n";
  print "                      (eg. daophot < batch1.cmd).  This switch prevents\n";
  print "                      these files from being deleted.  Useful for debugging\n";
  print "                      and/or doccumentation.\n";
  print "\n";
  print "              --noop  Set up everything, but don't actually execute the\n";
  print "                      DAOPHOT command.  Useful for debugging and\n";
  print "                      troubleshooting.\n";
  print "\n";
  print "              --force, -f  Force delete files if they already exist.\n";
  print "                      If not enabled, program will halt and inform the user\n";
```

```
  print "                        which files need to be deleted.\n";
  print "\n";
  print "              --verbose, -v   Verbose output (as usual)\n";
  print "\n";
  print "              --debug, -d   Debug output (as usual)\n";
  print "\n";

}

##############################################################################
#
#       PrintArgs
#
#       Just a pretty way to print the input arguments.  Mainly used for
#       debugging
#
##############################################################################

sub PrintArgs  {

  print "\nInput arguments report\n\n";

  print "\tInput frame: $infile\n";
  print "\tOutput file basename: $basename\n";
  print "\tData directory path: $datapath\n\n";

  print "\tnoclean enabled\n" if ( ! $clean );
  print "\tnoop enabled\n" if $noop;
  print "\tverbose enabled\n" if $verbose;
  print "\tdebug enabled\n" if $debug;

  print "\nEnd input arguments report\n\n";
}

##############################################################################
#
#       QueryUser
#
#       A simple routine to prompt the user for a yes or no response.
#       Returns 1 for a yes answer, 0 for a no.  Continues to prompt the user
#       until a y or n is entered.
#
##############################################################################

sub QueryUser  {


  while ($yesno = <STDIN> )
  {

    chomp ($yesno);  #if I had a nickel for each minute I wasted debugging
                  # because I fogot to chomp the input....

    print "yesno = $yesno\n" if $debug;

    if ($yesno eq "y")
    {
      return 1;
    }
    elsif ($yesno eq "n")
    {
      return 0;
    }
    else
    {
      print "Please type 'y' or 'n' (no quotes) ";
```

```
    }

  }

}


##############################################################################################
#
#       Iterate
#
#       Set up the batch script for the each iteration through DAOPHOT.
#       Execute the script unless --noop is set
#
#       Arguments:
#               iteration index (0 or 1)
#
##############################################################################################

sub Iterate($)
{
  my $iteration = $_[0];
  my $next_iteration = $iteration + 1;
  my $prev_iteration = $iteration - 1;
  my $cmdfile = "daocommands.$iteration.bat";
  my $prefix = "";

  print "Iteration = $iteration\n" if ($debug);

  if ($datapath ne ".")
  {
    $prefix = "DDIR:";
  }

  # because the same filename is prompted for over and over....
  my $apfile = "$basename.ap";
  my $lstfile = "$basename.$iteration.lst";
  my $psffile = "$basename.$iteration.psf";
  my $neifile = "$basename.$iteration.nei";
  my $grpfile = "$basename.$iteration.grp";
  my $nstfile = "$basename.$iteration.nst";
  my $subfile = "$basename.sub.$iteration.fits";

  # Do this to fake DAOPHOT into thinking the file already exists.  This
  #  will force a new filename to be prompted for

  if ($iteration == 0)
  {
    symlink ( "$datapath/$basename.$iteration.nei", "$datapath/$basename.nei");

    # By historic convention (ie. habit), the first iteration .lst file
    # does not explicitly include the iteration index.  So we'll just
    # treat it as a special case.

    $lstfile = "$basename.lst";
  }

  if ($iteration == 2)
  {
    $lstfile = "$basename.$prev_iteration.lst";
  }


  # Test for required files that may be missing.
  if (! -e "$datapath/$apfile")
  {
```

```
  die "Required DAOPHOT intput file $apfile missing.\n";
}

if (! -e "$datapath/$lstfile")
{
  die "Required DAOPHOT input file $lstfile missing.\n";
}

# test for pre-existing filenames.  If output files already exist, it
# will change the way DAOPHOT prompts for input, and mess up the batch
# scripts.

my @ExistingFiles;
my $files_exist = 0;

if (-e "$datapath/$psffile")
{
  push (@ExistingFiles, $psffile);
  $files_exist++;
}

if (-e "$datapath/$neifile")
{
  push (@ExistingFiles, $neifile);
  $files_exist++;
}

if (-e "$datapath/$grpfile")
{
  push (@ExistingFiles, $grpfile);
  $files_exist++;
}

if (-e "$datapath/$nstfile")
{
  push (@ExistingFiles, $nstfile);
  $files_exist++;
}

if (-e "$datapath/$subfile")
{
  push (@ExistingFiles, $subfile);
  $files_exist++;
}


if ($files_exist > 0)
{
  if ($force)
  {
    print "## Deleting the following pre-existing files:\n" if ($verbose);

    foreach $existingfile (@ExistingFiles)
    {
      print "\t$datapath/$existingfile\n" if ($verbose);
      unlink ("$datapath/$existingfile");
    }
  }
  else
  {
    die "The following files in the directory \n$datapath\n must be
         deleted or moved out of the way\n@ExistingFiles\n";
  }
}
```

```
# Critical overlap is a DAOPHOT input.  I use 0.1, but this may change.
my $critical_overlap = 0.1;

open (CMDFILE, ">$cmdfile") or die "Unable to open batch file $cmdfile";

# The following comments are the command prompts.  The print statements
# are the DAOPHOT inputs

# Command
if ($iteration == 2)
{
  print CMDFILE "attach $prefix$basename.subN.fits\n";
}
else
{
  print CMDFILE "attach $prefix$infile\n";
}

# Command
print CMDFILE "psf\n";

if ($iteration == 0)
{
  # File with aperture results
  print CMDFILE "$prefix$apfile\n";
}
else
{
  # Use the previous iteration's nei file.
  print CMDFILE "$prefix$basename.$prev_iteration.nei\n";
}

# File with PSF stars
print CMDFILE "$prefix$lstfile\n";

# File for the PSF
print CMDFILE "$prefix$psffile\n";

# Prompt for a new filename for the .nei file
print CMDFILE "$prefix$neifile\n";

if ($iteration < 2)
{

  # Command
  print CMDFILE "group\n";

  # File with photometry
  print CMDFILE "$prefix$neifile\n";

  # File with the PSF
  print CMDFILE "$prefix$psffile\n";

  # Critical overlap
  print CMDFILE "$critical_overlap\n";

  # File for stellar groups
  print CMDFILE "$prefix$grpfile\n";

  # Command:
  print CMDFILE "nstar\n";

  # File with the PSF
  print CMDFILE "$prefix$psffile\n";

  # File with stellar groups
```

```
    print CMDFILE "$prefix$grpfile\n";

    # File for results
    print CMDFILE "$prefix$nstfile\n";

    # Command
    print CMDFILE "substar\n";

    # File with the PSF
    print CMDFILE "$prefix$psffile\n";

    # File with photometry
    print CMDFILE "$prefix$nstfile\n";

    # Do you have stars to leave in?  at this point, no.
    print CMDFILE "no\n";

    # Name for subtracted image
    print CMDFILE "$prefix$subfile\n";

    # One more time through substar to create the image with the PSF stars
    # in place but their neighbors subtracted away.
    if ($iteration == 1)
    {
      # Command
      print CMDFILE "substar\n";

      # File with the PSF
      print CMDFILE "$prefix$psffile\n";

      # File with photometry
      print CMDFILE "$prefix$nstfile\n";

      # Do you have stars to leave in?  Now we do.
      print CMDFILE "yes\n";

      # File with star list
      print CMDFILE "$prefix$lstfile\n";

      # Name for subtracted image
      print CMDFILE "$prefix$basename.subN.fits\n";
    }

}

print CMDFILE "exit\n";

close CMDFILE;

push (@CleanupFiles, $cmdfile);

my $command;

if ($datapath eq ".")
{
  $command = "$daophot < $cmdfile";
}
else
{
  $command = "env DDIR=$datapath $daophot < $cmdfile";
}

print "\n## Executing command:\n\t$command\n\n" if $verbose;

# call DAOPHOT
if (! $noop)
```

```
  {
    system ($command) == 0 or die "system $command failed: $?";
  }

  if ($iteration == 0)
  {
    copy ("$datapath/$lstfile", "$datapath/$basename.$next_iteration.lst")
      or die "!! copy .lst file failed.\n";

    print "## Creating a new .lst file for the next iteration:\n
          \t$datapath/$basename.$next_iteration.lst\n" if $verbose;
  }
}


##############################################################################################
#
#       RunAllstar
#
#       Set up and execute an ALLSTAR run using the results of DAOPHOT.
#
##############################################################################################

sub RunAllstar  {

  my $cmdfile = "alscommands.bat";
  my $prefix = "";

  if ($datapath ne ".")
  {
    $prefix = "DDIR:";
  }

  my $apfile = "$basename.ap";
  my $psffile = "$basename.2.psf";
  my $alsfile = "$basename.als";
  my $subfile = "$basename.allsub.fits";

  # test for pre-existing filenames.  If output files already exist, it
  # will change the way DAOPHOT prompts for input, and mess up the batch
  # scripts.

  my @ExistingFiles;
  my $files_exist = 0;

  if (-e "$datapath/$alsfile")
  {
    push (@ExistingFiles, $alsfile);
    $files_exist++;
  }

  if (-e "$datapath/$subfile")
  {
    push (@ExistingFiles, $subfile);
    $files_exist++;
  }


  if ($files_exist > 0)
  {
    if ($force)
    {
      print "## Deleting the following pre-existing files:\n" if ($verbose);

      foreach $existingfile (@ExistingFiles)
      {
```

```
        print "\t$datapath/$existingfile\n" if ($verbose);
        unlink ("$datapath/$existingfile");
      }
    }
    else
    {
      die "The following files in the directory \n$datapath\n must be
           deleted or moved out of the way\n@ExistingFiles\n";
    }
  }

  open (CMDFILE, ">$cmdfile") or die "Unable to open batch file $cmdfile";

  # Toss in a carriage return to accept the default options.
  print CMDFILE "\n";

  # Input image name:
  print CMDFILE "$prefix$infile\n";

  # File with the PSF:
  print CMDFILE "$prefix$psffile\n";

  # Input file
  print CMDFILE "$prefix$apfile\n";

  # File for the results
  print CMDFILE "$prefix$alsfile\n";

  # Name for the subtracted image
  print CMDFILE "$prefix$subfile\n";

  close CMDFILE;
  push (@CleanupFiles, $cmdfile);

  my $command;

  if ($datapath eq ".")
  {
    $command = "$allstar < $cmdfile";
  }
  else
  {
    $command = "env DDIR=$datapath $allstar < $cmdfile";
  }

  print "\n## Executing command:\n\t$command\n\n" if $verbose;

  # call ALLSTAR
  if (! $noop)
  {
    system ($command) == 0 or die "system $command failed: $?";
  }

  # That's all folks!

}
```

## BIBLIOGRAPHY


Aaronson, M., Schommer, R. A., & Olszewski, E. W. 1984, The Astrophysical Journal, 276, 221

Ackermann, M., Ajello, M., Allafort, A., et al. 2013, Science (New York, N.Y.), 339, 807

Armandroff, T. E., & Da Costa, G. S. 1991, The Astronomical Journal, 101, 1329

Arp, H. 1962, The Astrophysical Journal, 135, 311

Ashman, K. M., & Zeph, S. E. 1998, Globular Cluster Systems (Cambridge, U.K. ; New York: Cambridge University Press)

Becker, A. C., Silvestri, N. M., Owen, R. E., Ivezić, v., & Lupton, R. H. 2007, Publications of the Astronomical Society of the Pacific, 119, 1462

Belokurov, V., Zucker, D. B., Evans, N. W., et al. 2006, The Astrophysical Journal, 642, L137

Bergbusch, P. A., & Stetson, P. B. 2009, The Astronomical Journal, 76, 1455

Borissova, J., Catelan, M., Spassova, N., & Sweigart, A. V. 1996, The Astronomical Journal, 113, 31

Brewer, M.-m., & Carney, B. W. 2006, The Astronomical Journal, 131, 431

Burstein, D., & Heiles, C. 1982, The Astronomical Journal, 87, 1165

Cacciari, C., & Clementini, G. 2003, in Lecture Notes in Physics, ed. D. Alloin & W. Gieren, Vol. 635 (Springer), 105–122

Caliskan, S., Christlieb, N., & Grebel, K. E. 2012, Astronomy & Astrophysics, 537, 13

Carney, B. W. 1996, Publications of the Astronomical Society of the Pacific, 108, 900

Carney, B. W., & Harris, W. E. 2001, Star Clusters, ed. L. Labhardt & B. Binggeli (Berlin: Springer)

Carney, B. W., & Seitzer, P. 1993, The Astronomical Journal, 105, 2127

Carretta, E., Bragaglia, A., Gratton, R., D'Orazi, V., & Lucatello, S. 2009, Astronomy & Astrophysics, 506, 14

Carretta, E., Cohen, J. G., Gratton, R. G., & Behr, B. B. 2001, The Astronomical Journal, 122, 1469

Carretta, E., & Gratton, R. G. 1997, Astronomy and Astrophysics Supplement Series, 121, 95

Catelan, M. 1999, The Astrophysical Journal, 531, 862

—. 2009, Astrophysics and Space Science, 320, 261

Catelan, M., Bellazzini, M., Landsman, W. B., et al. 2001, The Astronomical Journal, 122, 3171

Cecil, G. N., & Crain, J. A. 2004, in Proceedings of the SPIE, ed. J. Hough & G. H. Sanders, Vol. 5493, 73–80

Chaboyer, B. 1999, in Post-Hipparcos Cosmic Candles, ed. A. Heck & F. Caputo (Boston: Kluwer Academic Publishers), 111

Clayton, D. D. 1968, Principles of Stellar Evolution and Nucleosynthesis (Chicago: The University of Chicago Press)

Cohen, J., Huang, W., & Kirby, E. 2011, The Astronomical Journal, 60

Cohen, J., & Kirby, E. 2012, The Astrophysical Journal, 760

Da Costa, G. S. 1995, Publications of the Astronomical Society of the Pacific, 107, 937

Davis, D. S., Richer, H. B., Anderson, J., et al. 2008, The Astronomical Journal, 135, 2155

Dotter, A. 2013, Memorie della Societa Astronomica Italiana, 84, 97

Dotter, A., Chaboyer, B., Jevremović, D., et al. 2008a, The Astrophysical Journal Supplement Series, 178, 89

Dotter, A., Sarajedini, A., & Anderson, J. 2011, The Astrophysical Journal, 738, 74

Dotter, A., Sarajedini, A., & Yang, S.-C. 2008b, The Astronomical Journal, 136, 1407

Dotter, A., Sarajedini, A., Anderson, J., et al. 2010a, The Astrophysical Journal, 708, 698

—. 2010b, The Astrophysical Journal, 708, 698

Eddington, A. S. 1926, The Internal Constitution of the Stars (Cambridge: Cambridge University Press)

Eggen, O. J., Lynden-Bell, D., & Sandage, A. R. 1962, The Astrophysical Journal, 136, 748

Ferraro, F. R., Carretta, E., Corsi, C. E., et al. 1997, Astronomy and Astrophysics, 320, 757

Forbes, D. a., & Bridges, T. 2010, Monthly Notices of the Royal Astronomical Society, 1214, 1203

Freeman, K., & Bland-Hawthorn, J. 2002, Annual Review of Astronomy and Astrophysics, 40, 487

Geisler, D., Wallerstein, G., Smith, V. V., & Casetti-Dinescu, D. I. 2007, Publications of the Astronomical Society of the Pacific, 119, 939

Green, E., Demarque, P., & King, C. 1987, The revised Yale isochrones and luminosity functions (New Haven: Yale University Observatory)

Green, E. M., & Norris, J. E. 1990, The Astrophysical Journal, 353, L17

Hardie, R. 1959, The Astrophysical Journal, 130, 663

Harris, W. E. 1996, The Astronomical Journal, 112, 1487

Harris, W. E., Fitzgerald, M. P., & Reed, B. C. 1981, Publications of the Astronomical Society of the Pacific, 93, 507

Harris, W. E., & Hesser, J. E. 1976, NGC 5694: A Globular Cluster Escaping from the Galaxy?

Harris, W. E., & Racine, R. 1979, Annual Review of Astronomy and Astrophysics, 17, 241

Hauschildt, P. H., Allard, F., & Baron, E. 1999a, The Astrophysical Journal, 512, 377

Hauschildt, P. H., Allard, F., Ferguson, J., Baron, E., & Alexander, D. R. 1999b, The Astrophysical Journal, 525, 871

Hayashi, C., & Hoshi, R. 1961, Publications of the Astronomical Society of Japan, 13, 442

Hilker, M. 2006, Astronomy and Astrophysics, 448, 171

Hiltner, W. A., ed. 1962, Astronomical Techniques, v. 2 edn. (University Press), 196–203

Holmberg, E., & Lauberts, A. 1975, Astronomy and Astrophysics Supplement Series, 22, 327

Irwin, J. B. 1952, Science (New York, N.Y.), 115, 223

Irwin, M. J., Demers, S., & Kunkel, W. E. 1995, The Astrophysical Journal, 453, L21

Joye, W., & Mandel, E. 2003, in ... Data Analysis Software and Systems XII, ed. H. E. Payne, R. I. Edrzejewski, & R. N. Hook, Vol. 295, 489–492

Keller, S. C., Mackey, D., & Da Costa, G. S. 2012, The Astrophysical Journal, 744, 57

Kim, Y.-c., Demarque, P., Yi, S. K., & Alexander, D. R. 2002, The Astrophysical Journal Supplement Series, 143, 499

King, I. R. 1966, The Astronomical Journal, 71, 276

Koch, A., & Côté, P. 2010, Astronomy & Astrophysics, 517, 15

Koch, A., Côté, P., & McWilliam, A. 2009, Astronomy & Astrophysics, 506, 729

Lai, D. K., Smith, G. H., Bolte, M., et al. 2011, The Astronomical Journal, 141, 62

Landolt, A. U. 1992, The Astronomical Journal, 104, 340

Lee, J.-w., & Carney, B. W. 1999, The Astronomical Journal, 118, 1373

Lee, J.-W., Lopez-Morales, M., & Carney, B. W. 2006, The Astrophysical Journal, 646, 119

Lee, Y.-W. 1990, The Astrophysical Journal, 363, 159

Lee, Y.-W., Demarque, P., & Zinn, R. 1994, The Astrophysical Journal, 423, 248

Mackey, A. D., & Gilmore, G. F. 2004, Monthly Notices of the Royal Astronomical Society, 355, 504

Madore, B. F., & Arp, H. C. 1979, The Astrophysical Journal, 227, L103

Marín-Franch, A., Aparicio, A., Piotto, G., et al. 2009, The Astrophysical Journal, 694, 1498

Massey, P. 1997, NOAO Laboratory, Tuscon, AZ

Mucciarelli, a., Bellazzini, M., Catelan, M., et al. 2013, Monthly Notices of the Royal Astronomical Society, 435, 3667

Mucciarelli, A., Bellazzini, M., Merle, T., et al. 2015, The Astrophysical Journal, 801, 68

Ochsenbein, F., Bauer, P., & Marcout, J. 2000, Astronomy and Astrophysics Supplement Series, 143, 23

Ortolani, S. 1984, Astronomy and Astrophysics, 137, 269

Palma, C., Kunkel, W., & Majewski, S. 2000, Publications of the Astronomical Society of the Pacific, 112, 1305

Palma, C., Majewski, S. R., & Johnston, K. V. 2002, The Astrophysical Journal, 564, 736

Pence, W. D., Chiappetti, L., Page, C. G., Shaw, R. a., & Stobie, E. 2010, Astronomy & Astrophysics, 524, A42

Piotto, G. 2009, in The Ages of Stars, Proceedings of the International Astronomical Union, IAU Symposium, ed. E. Mamajek, D. R. Soderblom, & R. Wyse No. 258, 233–244

Piotto, G., Bedin, L. R., Anderson, J., et al. 2007, The Astrophysical Journal, 661, L53

Racine, R., & Harris, W. E. 1989, The Astronomical Journal, 98, 1609

Reed, B. C., Hesser, J. E., & Shawl, S. J. 1988, Publications of the Astronomical Society of the Pacific, 100, 545

Reid, N. 1996, Monthly Notices of the Royal Astronomical Society, 278, 367

Reid, N., & Majewski, S. R. 1993, The Astrophysical Journal, 409, 635

Rey, S.-C., Yoon, S.-J., Lee, Y.-W., Chaboyer, B., & Sarajedini, A. 2001, The Astronomical Journal, 122, 3219

Rix, H. W., & Bovy, J. 2013, Astronomy and Astrophysics Review, 21

Robin, a. C., Reylé, C., Derrière, S., & Picaud, S. 2004, Astronomy & Astrophysics, 409, 523

Rutledge, G. A., Hesser, J. E., Stetson, P. B., et al. 1997, Publications of the Astronomical Society of the Pacific, 109, 883

Sandage, A. 1982, The Astrophysical Journal, 252, 553

Sandage, A., & Wildey, R. 1967, The Astrophysical Journal, 150, 469

Sandquist, E. L., Bolte, M., Stetson, P. B., & Hesser, J. E. 1996, The Astrophysical Journal, 470, 910

Sarajedini, A. 1994, The Astronomical Journal, 107, 618

Sarajedini, A., & Geisler, D. 1996, The Astronomical Journal, 112, 2013

Sarajedini, A., Lee, Y.-W., & Lee, D.-H. 1995, The Astrophysical Journal, 450, 712

Sarajedini, A., Bedin, L. R., Chaboyer, B., et al. 2007, The Astronomical Journal, 133, 1658

Schlegel, D. J., Finkbeiner, D. P., & Davis, M. 1998, The Astrophysical Journal, 500, 525

Searle, L., & Zinn, R. 1978, The Astrophysical Journal, 225, 357

Smith, G. S. 2005, American Journal of Physics, 73, 590

Sollima, a., Martinez-Delgado, D., Valls-Gabaud, D., & Penarrubia, J. 2011, The Astrophysical Journal, 726:47, 8

Spergel, D. N., Verde, L., Peiris, H. V., et al. 2003, The Astrophysical Journal Supplement Series, 148, 175

Stetson, P. B. 1987, Publications of the Astronomical Society of the Pacific, 99, 191

—. 1990, Publications of the Astronomical Society of the Pacific, 102, 932

—. 1994, Publications of the Astronomical Society of the Pacific, 106, 250

—. 2000, Users Manual for DAOPHOT II, Tech. rep., Victoria: Dominion Astrophysical Observatory

Stetson, P. B., & Harris, W. E. 1988, The Astronomical Journal, 96, 909

Stetson, P. B., Bolte, M., Harris, W. E., et al. 1999, The Astronomical Journal, 117, 247

Suntzeff, N., Olszewski, E., & Stetson, P. B. 1985, The Astronomical Journal, 90, 1481

Tody, D. 1993, Astronomical Data Analysis Software and Systems II, 52, 173

Turner, A. 1997, Cooking with ALLFRAME version 3.0, Tech. rep., Victoria: Dominion Astrophysical Observatory

van den Bergh, S. 1967, The Astronomical Journal, 72, 70

VandenBerg, D. a., Bergbusch, P. a., & Dowler, P. D. 2006, The Astrophysical Journal Supplement Series, 162, 375

Vandenberg, D. A., Bolte, M., & Stetson, P. B. 1990, The Astronomical Journal, 100, 445

VandenBerg, D. a., Brogaard, K., Leaman, R., & Casagrande, L. 2013, The Astrophysical Journal, 775, 134

VandenBerg, D. a., & Clem, J. L. 2003, The Astronomical Journal, 126, 778

Venn, K. a., Irwin, M., Shetrone, M. D., et al. 2004, The Astronomical Journal, 128, 1177

Walker, A. R. 1992, The Astrophysical Journal, 390, L81

Webbink, R. 1985, in Dynamics of star clusters; Proceedings of the Symposium, Princeton, NJ, May 29-June 1, 1984, ed. J. Goodman & P. Hut, Vol. 113 (Dordrecht, D. Reidel), 541–577

Weinberger, R. 1995, Publications of the Astronomical Society of the Pacific, 107, 58

Zinn, R. 1980, The Astrophysical Journal, 241, 602

—. 1985, The Astrophysical Journal, 293, 424

Zinn, R. 1993, in The Globular Cluster-Galaxy Connection, ed. G. H. Smith & J. P. Brodie, Vol. 48 (San Fransisco: Astronomical Society of the Pacific Conference Series), 38–47

Zinn, R., & West, M. J. 1984, The Astrophysical Journal Supplement Series, 55, 45